DEVELOPMENT AND APPLICATIONS OF A FULLY IMPLICITLY COUPLED WELLBORE-RESERVOIR SIMULATOR

A Dissertation

by

HEWEI TANG

Submitted to the Office of Graduate and Professional Studies of
Texas A&M University
in partial fulfillment of the requirements for the degree of

DOCTOR OF PHILOSOPHY

Chair of Committee,	John E. Killough
Co-Chair of Committee,	A. Rashid Hasan
Committee Members,	Maria A. Barrufet
	Eduardo Gildin
Head of Department,	Jeff Spath

May 2019

Major Subject: Petroleum Engineering

Copyright 2019 Hewei Tang

ABSTRACT

In this dissertation, we develop a compositional multiphase wellbore-reservoir simulator, GURU-MSW. The compositional reservoir simulator GURU serves as the starting point of this work. GURU-MSW fully implicit couples a multi-segment wellbore (MSW) model with the reservoir simulator GURU. Although taking the most developing effort, the fully implicit coupling mechanism is considered to be unconditionally stable and fast.

After developing the general framework of the simulator, the coupled MSW-reservoir simulator is tested in two application scenarios, both being the first attempt in the literature. The first application is to analyze the well interference phenomenon. Well interference, introduced by the inter-well fracture hits, is a major production issue in shale reservoir development. When fracture hits occur, GURU-MSW can capture the sudden production rate jump caused by the wellbore crossflow. We also apply GURU-MSW to model a case with three wells under well group control.

The second application of GURU-MSW is the simulation of liquid loading phenomenon. Liquid loading is an inevitable production issue in mature gas fields, which occurs when the producing gas rate is not high enough to carry all the liquids to wellbore surface. This is a phenomenon that can neither be comprehensively simulated by a single wellbore simulator nor a single reservoir simulator because of the dynamic interaction between wellbore and reservoir. GURU-MSW successfully characterizes the dynamic interaction between wellbore multiphase flow and reservoir multiphase flow. We

systematically analyze a cyclical production phenomenon, which was only reported as field observations previously.

Two new gas-liquid drift-flux models are proposed in this dissertation. The first model incorporates the flow regime transition criteria from annular flow to churn or slug flow for vertical, slanted and horizontal pipes. The model is specially designed for the application of liquid loading modeling in horizontal gas wells.

The second model is a unified model for all pipe inclinations. The new model is tested against 5805 experimental measured data points from 22 sources as well as 13440 data points from the OLGA-S library. The numerical stability of the model is tested with GURU-MSW. The drift-flux model commonly applied in MSW simulation only covers a pipe inclination range from 2° (nearly horizontal) to 90° (vertical upward). The proposed model has a potential in filling in the gap left by the existing drift-flux model.

DEDICATION

To

my husband

Zhuang

for his love, patience and support

ACKNOWLEDGEMENTS

I want to first express my sincere gratitude to my advisor Professor John E. Killough. I joined Dr. Killough's research group in 2014 as a Master student. He guided me into the community of reservoir simulation. I am always amazed by his broad knowledge, profound insight and novel ideas. Dr. Killough has been really supportive during my Ph.D. study. I am especially grateful that he offered me sufficient freedom to explore the research areas that I am interested in.

I want to express my deep gratitude to my co-advisor Professor A. Rashid Hasan. Dr. Hasan is a world-class expert in wellbore multi-phase flow modeling. He offered me a lot of inspiration and encouragement when I met the bottleneck of my Ph.D. work.

I also want to sincerely thank my committee members, Professor Maria A. Barrufet and Professor Eduardo Gildin. Dr. Barrufet generously shared the simulator developed by her student, Dr. Ernesto Valbuena Olivares. This simulator inspired the development of GURU and GURU-MSW. Dr. Gildin also kindly shared with me his knowledge on coupled wellbore-reservoir simulation. The suggested references from him helped deepen my understanding in this research area.

During my Ph.D. study, I gained a lot of help from Professor Peter Valko and Dr. Nozomu Yoshida. I had several long talks with Dr. Valko discussing the liquid loading phenomenon. He offered me a lot of encouragement in pursuing this research direction. Dr. Yoshida kindly shared with me his expertise in developing a coupled wellbore reservoir simulator when I first started. I sincerely acknowledge their time and kindness.

Special thanks go to Dr. William Bailey, my mentor during my internship with Schlumberger-Doll Research center. The work with him made the Section 5 of this dissertation possible. His recognition of my Ph.D. work gave me a lot of strength and confidence.

I appreciate my time spent with the friends of Dr. Killough's research group and Dr. Hasan's research group. They offered me many suggestions and help during my Ph.D. study.

Finally, I am deeply indebted to my parents and my husband. Without their support and love, none of this work would be possible.

CONTRIBUTORS AND FUNDING SOURCES

Contributors

This work was supervised by a dissertation committee consisting of Professor John E. Killough [advisor], Professor A. Rashid Hasan [co-advisor], and Professor Eduardo Gildin of the Department of Petroleum Engineering, as well as Professor Maria A. Barrufet of the Department of Chemical Engineering.

The reservoir simulation part in GURU-MSW was developed by Dr. Bicheng Yan. The Embedded Discrete Fracture Model (EDFM) applied in Chapter 3 was developed by Dr. Zhi Chai. Both of them are members of Dr. Killough's research group in the Department of Petroleum Engineering at Texas A&M University. The experimental data applied in Chapter 5 were original from Tulsa University Fluid Flow Project (TUFFP) and provided by Dr. William Bailey.

All other work conducted for the dissertation was completed by the student independently.

Funding Sources

Graduate study was supported financially by the Crisman Institute for Petroleum Research at Texas A&M University. Schlumberger-Doll Research center funded the work of Chapter 5 in this dissertation.

NOMENCLATURE

Acronyms

DFM	Drift-Flux Model
DTS	Distributed Temperature Sensors
ECLIPSE	Industry Reference Reservoir Simulator own by Schlumberger
EDFM	Embedded Discrete Fracture Model
EDFN	Enhanced Discrete Fracture Network
FPSO	Floating Production Storage and Offloading
GURU	General Unstructured Reservoir Utility
ILU	Incomplete Factorization Preconditioner
IPR	Inflow Performance Relation
LGR	Local Grid Refinement
MSW	Multi-Segment Well
NEXUS	Reservoir Simulator developed by Landmark, Halliburton
NPW	No Pressure Wave Model
NNC	Non-Neighbor Connections
OLGA	Dynamic Multiphase Flow Simulator
PDE	Partial Differential Equation
SRV	Stimulated Reservoir Volume
TFM	Two-Fluid Model
THP	Tubing Head Pressure
TUFFP	Tulsa University Fluid Flow Project

VLE	Vapor Liquid Equilibrium
3D	Three Dimensional

Notation

A	flow cross section area, ft^2
C_0	profile parameter
D	pipe inner diameter, ft
f_f	frictional factor
f_g	gas inlet fraction
f_v	molar vapor fraction
Fr	Froude number
g	gravity constant
h	absolute height of wellbore segment, ft
h_f	height of fracture segment, ft
J	Jacobian matrix
k	permeability, mD
K_c	equilibrium ratio
K_u	critical Kutateladze number
l_f	length of fracture segment, ft
L	segment length, ft
La	inverse of dimensionless hydraulic pipe diameter
n	net mole flow rate, mol/day

N	moles of component/water per unit volume, mol/ft^3
N_B	bond number
$N_{Eö}$	Eötvös number
N_μ	viscosity number
P	pressure, psia
P_c	critical pressure, psia
$Q^*_{v,p}$	volume flux of phase *p* at standard condition, scf/day or STB/day
$\tilde{Q}_p$	molar rate of phase *p*, lbmol/day
r_o	equilibrium radius of reservoir grid
r_w	wellbore radius
R	residual
Re	Reynolds number
S_p	saturation of phase *p*
S	well skin factor
T	temperature, °F
T_c	critical temperature, °F
T_s	Transmissibility between two connected reservoir cells
T_w	well geometry index
v_d	drift-flux velocity
v_p	velocity of phase *p*, ft/s or m/s
v_{sp}	superficial velocity of phase *p*, ft/s or m/s
V	volume, ft^3

V_c	characteristic velocity, ft/s or m/s
V_{sgf}	gas flooding velocity, ft/s or m/s
w_c	acentric factor of component c
w_f	fracture width, ft
x	liquid mole fraction
X_p	tunable parameter set for the drift-flux model
y	vapor mole fraction
z	overall mole fraction
Z	compressibility factor
α	volume fraction, holdup
β	violation factor
ε	relative pipe roughness
ξ	input fluid properties
κ	binary interaction coefficient
γ	profile parameter reduction term
λ_p	mobility of phase p
θ	wellbore/pipe inclination
φ	fugacity coefficient
Ψ_p	potential of each phase p, psia
μ	viscosity, cP
ρ	density, lb/ft^3
$\tilde{\rho}$	molar density, lbmol/ft^3

σ	interfacial tension, dynes/cm
χ	two phase flow quality

Subscripts and Superscripts

c	hydrocarbon component
f	fracture
g	gas
h	horizontal
l	liquid
m	mixture
o	oil
opt	optimized
OLG	OLGA-S
perf	perforation
res	reservoir grid
s	source/sink
seg	wellbore segment
TUF	TUFFP
v	vapor or vertical
w	water

TABLE OF CONTENTS

Page

LIST OF FIGURES

Page

LIST OF TABLES

Page

1. INTRODUCTION

1.1 Background

Reservoir and wellbore are two crucial components in modern petroleum exploration. Understanding the dynamic interaction between reservoir and wellbore is important for improving the asset productivity. Integrated reservoir, wellbore and surface facility simulation has always been a need in offshore exploration. For offshore development, multilateral wells are commonly applied and multiple reservoirs may connect to a single Floating Production Storage and Offloading unit (FPSO). Recently, as long lateral horizontal wells become a common practice in onshore unconventional reservoir exploration, there are also increasing desires to couple the dynamic flow behaviors between reservoir and wellbore.

Unlike flow in porous media, where flow velocities are calculated through Darcy's law, flow velocities in wellbore need to be solved through momentum balance at different complexity. The solutions are even more complicated when it comes to multiphase wellbore flow. There are several stand-alone wellbore simulators at different sophisticated levels specially dealing with the multiphase flow in wellbore. In these simulators, reservoir is commonly represented through an inflow performance relation (IPR) curve. Contrary to a standalone wellbore simulator, the wellbore model coupled to a reservoir simulator has more numerical restrictions. The multiphase flow inside the wellbore can only be accounted through homogeneous or drift-flux models rather than more complex mechanistic models.

Although there are several existing simulators that perform coupled wellbore reservoir simulations, there are still a lot of research challenges that need to be solved. The dissertation is aimed to develop a general and flexible research platform for integrated simulation of reservoir and wellbore. The platform can be served for new model realizations and as an analyzing tool for industrial applications. The General Unstructured Reservoir Utility (GURU) developed by Yan (2017) in his Ph.D. work is the starting point of the work in this dissertation.

1.1.1 General Unstructured Reservoir Utility (GURU)

GURU is a compositional simulator for general reservoir simulation purpose. The reservoir simulator is based on finite volume spatial discretization. To handle unstructured reservoir cells, a connection list is served as input to document the relation between reservoir grid blocks (Cao, 2002). For example, GURU can simulate unstructured fracture network generated by Enhanced Discrete Fracture Network (EDFN) approach (Yan et al., 2018). These fracture grids have irregular shape and complex geometry based on different fracture orientations. The time discretization in GURU is fully implicit, which guarantees stable numerical solutions with large time steps. In addition, GURU incorporates several other features for fluid flow modeling in shale reservoirs. For example, GURU considers multi-component adsorption, Knudsen diffusion and gas slippage for the transport of shale gas. Moreover, to characterize a more realistic picture of shale reservoir, GURU incorporates a triple-porosity model considering inter-porosity and intra-porosity transport among fractures, inorganic matrix and organic matrix.

Figure 1.1 summarizes the six modules inside GURU. The rock fluid module is to calculate rock-fluid interaction properties such as relative permeability, capillary pressure and compaction. The fluid module includes the vapor liquid equilibrium (VLE) calculation for hydrocarbon properties. It also includes water property calculation and gas adsorption/desorption calculation in shale reservoir. Well control module computes the relevant Jacobian terms and residuals based on different well control modes. Mobility module computes mobility and flux-related terms. Flow equation module constructs the Jacobian matrix and residuals for Newton-Raphson methods. The linear solver module solves linear system for primary variables.

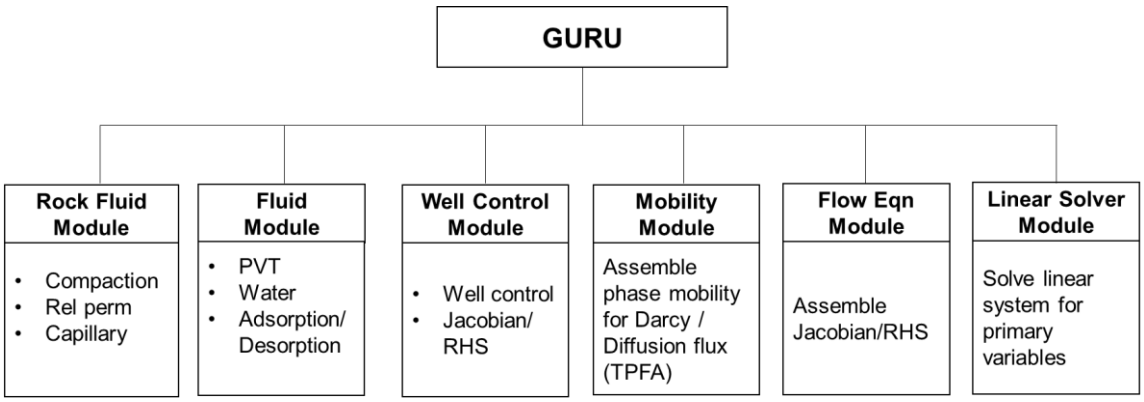

Figure 1.1–Major modules in GURU (reprinted from Yan, 2017).

Although GURU can handle different well control strategies, it is not capable in modeling advanced wellbore structures and the fluid flow inside wellbore. These capabilities are commonly achieved through a multi-segment wellbore (MSW) model.

Therefore, the focus of this dissertation is to couple the reservoir model (GURU) with an advanced wellbore model considering multiphase wellbore flows.

1.1.2 Coupled Wellbore-Reservoir Simulation

Conventionally, wellbore and reservoir are simulated separately because of the time scale difference (da Silva and Jansen, 2015). A dynamic wellbore simulator either assumes a constant reservoir inflow rate or applies a simple inflow performance relationship (IPR). A dynamic reservoir simulator either applies historical bottom-hole pressure (BHP) or a BHP value estimated from a tubing performance curve. The time scale of a multi-phase wellbore simulator is typically from seconds to hours, and the time scale of a reservoir simulator is typically from hours to decades. However, there exist several situations where the time scale of wellbore and reservoir overlap with each other, and the dynamic interaction between the two systems cannot be ignored. Figure 1.2 shows the time and spatial scales of natural production phenomena shown by Nennie et al. (2007), the situations include but are not limited to wellbore storage, liquid loading and clean-up process. Bahonar et al. (2011) developed a transient non-isothermal wellbore-reservoir model for gas-well testing, which is a single phase model. Yoshida (2016) developed a coupled two-phase wellbore-reservoir model for interpretation of data from distributed temperature sensors (DTS). Tang et al. (2018) developed a fully implicitly coupled wellbore-reservoir model, which implemented a novel drift-flux model specially designed for the liquid loading process.

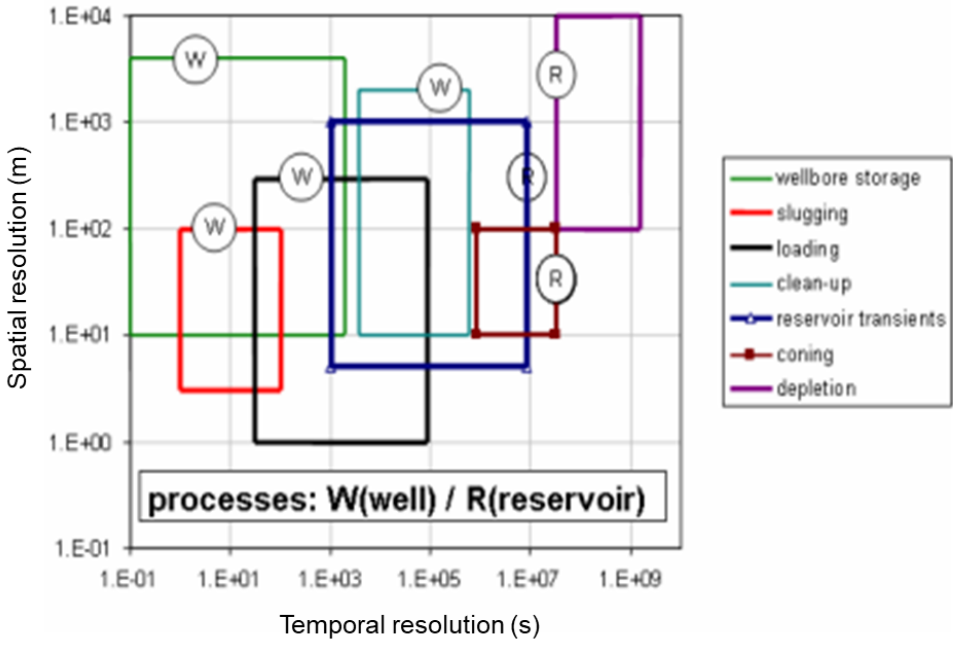

Figure 1.2–Time and spatial scales for different production scenarios (reprinted from Nennie et al., 2007).

The coupling of the wellbore model and the reservoir model can be at different levels. The industry commonly applies loosely-coupling approaches either at time step or newton iteration levels. If the final time step convergence criteria are based on the reservoir equations, then the approach coupled at the time step level is categorized as explicit, and the approach coupled at the newton iteration level is categorized as partially implicit (Coats et al., 2004). The advantages of loosely-coupling approaches include the convenience and flexibility. However, the numerical convergence of this coupling mechanism is not always guaranteed. Several research efforts have been made to improve the stability of the loosely-coupled approaches (Guyaguler et al., 2011; Redick, 2017; Yanbin Zhang et al., 2017). The most rigorous coupling approach is to merge the wellbore

equations and reservoir equations into a single set and solve them simultaneously, which is also known as the fully implicit approach (da Silva and Jansen, 2015). Although the fully implicit approach requires a lot of developing effort, it improves the stability and speed significantly (Cao et al., 2015). The fully implicitly coupled wellbore-reservoir simulator was first introduced by Stone et al. (1989). This tightly-coupled simulation approach has been widely adopted in a lot of black-oil and compositional systems (Coats et al., 2004; Livescu et al., 2010; Valbuena Olivares, 2015).

The tightly-coupled wellbore-reservoir model is also known as the multi-segment wellbore (MSW) model in several commercial reservoir simulators (ECLIPSE, NEXUS and etc.). Contrary to a standalone advanced wellbore simulator, the wellbore model coupled to a reservoir simulator is simpler in form. The wellbore multiphase flow is accounted for through the drift-flux model rather than the segregated flow model or the mechanistic model to ensure convergence and avoid numerical instability.

1.1.3 Two-phase Flow Modeling in Wellbores

The mechanical simulation of transient two-phase flow in pipelines includes two kinds of models: one is the Two-Fluid Model (TFM) and the other is the Drift-Flux Model (DFM). The TFM is governed by mass and momentum conservations of each phase. The representative commercial code for TFM is OLGA, which was developed in Norway (Bendiksen et al., 1991). The general two-fluid model can be expressed as follows:

$$\frac{\partial(\alpha_g \rho_g)}{\partial t} + \frac{\partial(\alpha_g v_g \rho_g)}{\partial x} = 0 \tag{1.1}$$

$$\frac{\partial(\alpha_l \rho_l)}{\partial t} + \frac{\partial(\alpha_l v_l \rho_l)}{\partial x} = 0 \tag{1.2}$$

$$\frac{\partial(\alpha_g v_g \rho_g)}{\partial t} + \frac{\partial(\alpha_g v_g^2 \rho_g)}{\partial x} + \alpha_g \frac{\partial p}{\partial x} = \tau_g - \tau_i + \rho_g \alpha_g g \sin(\theta) \tag{1.3}$$

$$\frac{\partial(\alpha_l v_l \rho_l)}{\partial t} + \frac{\partial(\alpha_l v_l^2 \rho_l)}{\partial x} + \alpha_l \frac{\partial p}{\partial x} = \tau_l - \tau_i + \rho_l \alpha_l g \sin(\theta) \tag{1.4}$$

The drift-flux model is governed by mass conservation equations of each phase and a single momentum conservation equation for phase mixture. The representative commercial code is TACITE, which was developed in France (Pauchon et al., 1993). The mass balances of DFM are the same as TFM (Equations (1.1) and (1.2)). The mixture momentum balance can be derived by summing up the momentum balances in TFM (Equations (1.3) and (1.4)), as shown in Equation (1.5).

$$\frac{\partial(\alpha_g v_g \rho_g + \alpha_l v_l \rho_l)}{\partial t} + \frac{\partial(\alpha_g v_g^2 \rho_g + \alpha_l v_l^2 \rho_l + p)}{\partial x} = \tau_l + \tau_g + (\rho_l \alpha_l + \rho_g \alpha_g) g \sin(\theta) \tag{1.5}$$

To close the equation system, Zuber and Findlay slip relation (Zuber and Findlay, 1965) is commonly applied in the TFM.

$$v_g = C_o v_m + v_d \tag{1.6}$$

There are two parameters that correlate the mixture velocity (v_m) with gas in situ velocity (v_g) in the model, one is the distribution parameter (C_o) and the other is drift velocity (v_d). The distribution parameter accounts for the non-uniform distribution of gas phase over the pipe cross section. The drift velocity describes the relative velocity of the gas phase

comparing to the two phase mixture velocity. The C_o and v_d are generally a function of mixture velocity, gas void fraction and fluid properties.

Both TFM and DFM are generally hyperbolic systems. However, the TFM can easily lose the hyperbolicity and well-posedness when the Kelvin-Helmholtz condition is met (Shirdel, 2013). The condition indicates the transition between stratified to non-stratified flow regimes. Regulation is required to avoid the related numerical instability. The DFM model is not unconditionally hyperbolic and well-posedness as some researchers claimed. Santim and Rosa (2016) analyzed the characteristic roots of the quasi-linear form of the drift-flux model. They found that the hyperbolicity of the system is guaranteed when $C_o\alpha_g < 1$. Their analysis was based on constant C_o and v_d. For more complex slip relations, analytical expression of the characteristic roots are not available. Faille and Heintzé (1999) presented a compositional drift-flux model that was implemented in TACITE. The model honored mass conservation equations for n hydrocarbon components and a mixture conservation equation as shown in Equation (1.5). They applied a complex hydrodynamic closure law based on different flow regimes (Pauchon and Dhulesia, 1994), which is a function based on the center of mass velocity, gas mass fracture, pressure and fluid component.

Aarsnes (2016) dived the two-phase flow pressure behavior into three time scales: the first time scale is about 10 seconds, which is dominated by distributed pressure dynamics; the second time scale is about 1-10 minutes, which is governed by slow compression pressure introduced by using flow rates as boundary conditions; and the third time scale is from 10min to hours, which is dominated by void wave advection. For most

production problems, it is sufficient to apply a dynamic model only with void wave advection. Therefore, the pressure wave is negligible because it does not have strong effect on the initiation and transport of void waves (Masella et al., 1998). The simplification leads to the no-pressure-wave (NPW) model, which solves the momentum equations as a local force balance, given in Equation (1.7).

$$\frac{\partial p}{\partial x} = \tau_l + \tau_g + (\rho_l \alpha_l + \rho_g \alpha_g) g \sin(\theta) \tag{1.7}$$

Nemoto et al. (2009) analyzed a three-phase (water, gas, oil) no-pressure-wave model with mass transport between oil and gas phases being considered. With α_g, α_o, p and v_m being the state variables, the characteristic roots of the system are as follows:

$$\lambda_1 = \frac{\partial v_g}{\partial \alpha_g};\ \lambda_2 = \frac{v_o}{\alpha_o};\ \lambda_3 = \infty;\ \lambda_4 = \infty; \tag{1.8}$$

Therefore, the model is classified as mixed hyperbolic/parabolic. The observation is consistent with that reported by Masella et al. (1998). The other reported no-pressure-wave models include Choi et al. (2013) and Aarsnes et al. (2016). The model of Choi et al. (2013) implemented a power law correlation for pressure drop calculation. Aarsnes et al. (2016) further reduced the model to a single hyperbolic PDE of void fraction and two closure relations of gas phase velocity and the static pressure.

The comparison of all the three models (TFM, DFM and NPW) has been conducted by Masella et al. (1998) and Santim et al. (2017). Masella et al. (1998) implemented a semi-implicit numerical scheme similar to that introduced by Faille and Heintzé (1999) for the DFM and an implicit numerical scheme for NPW. They concluded

that the DFM is faster than the NPW for a given accuracy. Santim et al. (2017) compared different models for analyzing the gas-liquid slug flow in a horizontal pipe. They applied an explicit scheme as introduced by Santim and Rosa (2016) for the DFM and a semi-implicit numerical scheme for the NPW. In the semi-implicit approach, the velocities and pressure were evaluated implicitly and the void fraction was evaluated explicitly. Santim et al. (2017) concluded that both DFM and NPW showed good agreement with the experimental data, while the DFM exhibited better predictions of pressure wave velocity.

1.2 Research Objectives

In GURU, wellbore is incorporated through standard wellbore model, where wells are considered as sink and source terms in reservoir grids. Therefore, the first objective of this dissertation is to develop a general multi-segment well (MSW) model for GURU platform. The new platform is named as GURU-MSW. We intend to make GURU-MSW a flexible framework for well group and surface network modeling.

As stated earlier, wellbore multiphase flow modeling is a big challenge in both standalone wellbore simulation and coupled wellbore-reservoir simulation. Therefore, another major effort of this dissertation is to improve the gas-liquid drift-flux modeling for applications in a coupled wellbore-reservoir simulator like GURU-MSW.

1.3 Dissertation Outline

The dissertation is organized as follows:

In Chapter 2, physical formulations in GURU-MSW are reviewed from two aspects: flow in porous media and flow in wellbore. Detailed numerical implementation such as discretization techniques, boundary conditions and initialization procedure are explained. As a fully implicitly coupled wellbore-reservoir simulator, a sample Jacobian matrix and the global linear system of GURU-MSW are also presented.

In Chapter 3, GURU-MSW is applied in the well interference study of shale reservoir. The simulator is benchmarked with Eclipse 300 in a case with three-phase reservoir fluid containing five hydrocarbon components. This verifies the reliability of GURU-MSW as a compositional simulator. The designed cases also reveal the capability of GURU-MSW in simulating wellbore crossflow and multiple well performance under different production constraints.

In Chapter 4, the drift-flux model proposed by Shi et al (2005) is improved to include the flow regime transition from annular to churn or slug flow. The modified drift-flux model is implemented in GURU-MSW. For the first time, we apply a fully coupled wellbore-reservoir simulator in gas well liquid loading modeling. This study demonstrates the capability of GURU-MSW as a comprehensive tool in characterizing the dynamic interaction between wellbore multiphase flow and reservoir multiphase flow.

In Chapter 5, a new unified drift-flux model for pipe inclinations from upward vertical to downward vertical is proposed. This new drift-flux model is validated with data from various sources. More importantly, the new model is proved to be numerically stable in GURU-MSW, and therefore applicable in fully coupled wellbore-reservoir simulation.

In Chapter 6, we summarize the contributions of this work and give suggestions to future research efforts.

2. FORMULATION OF GURU-MSW*

In traditional reservoir simulation, standard wells are represented by the sink and source terms in the grid blocks. The details of the fluid flow inside the wellbore are ignored. However, as wellbore structures become more and more complicated, this simplification can no longer fulfill the need of modeling wellbore trajectories, inflow control devices and so on. A common solution is to discretize the wellbore into segments along the flow direction and solve the wellbore flow as flow in pipe. This is also known as multi-segment well (MSW) model in reservoir simulation. We name the newly developed fully-implicitly coupled wellbore reservoir simulator as GURU-MSW. In this chapter, the mathematical formula and numerical implementation of GURU-MSW is introduced.

---

*Part of this section is reprinted with permission from "Analyzing the Well Interference Phenomenon in Eagle Ford Shale – Austin Chalk Production System with a Comprehensive Compositional Reservoir Model" by H. Tang, B. Yan, Z. Chai, et al. SPE Reservoir Evaluation and Engineering, Copyright [2018] by Society of Petroleum Engineer; from "What Happens After the Onset of Liquid Loading? --- An Insight from Coupled Well-Reservoir Simulation" by H. Tang, Z. Chai, Y. He et al. SPE Proceedings, Copyright [2018] by Society of Petroleum Engineers; and from "Development and Application of a Fully Implicitly Coupled Wellbore-Reservoir Simulator to Characterize the Flow Transients in Liquid-Loaded Horizontal Gas Wells" by H. Tang, A.R. Hasan, and J. Killough. SPE Journal, Copyright [2018] by Society of Petroleum Engineers.

2.1 Fluid Flow in Porous Media

2.1.1 Primary Equations

We consider three-phase (oil, gas and water) Darcy flow in the subsurface isothermal porous media. For each hydrocarbon component c in oil and gas phases, a mass conservation equation is given in Equation (2.1). Similarly, Equation (2.2) expresses the mass conservation equation in water phase. We assume that water is inertial and does not present in the oil and gas phases.

$$\nabla\left[kA\left(\frac{k_{ro}}{\mu_o}x_c\tilde{\rho}_o\nabla\psi_o+\frac{k_{rg}}{\mu_g}y_c\tilde{\rho}_g\nabla\psi_g\right)\right]=V_b\frac{\partial}{\partial t}\left(\phi N_c\right)-\sum_{perf}n_{c,s} \tag{2.1}$$

$$\nabla\left[kA\frac{k_{rw}}{\mu_w}\tilde{\rho}_w\nabla\psi_w\right]=V_b\frac{\partial}{\partial t}\left(\phi N_w\right)-\sum_{perf}n_{w,s} \tag{2.2}$$

$$N_c=S_o\tilde{\rho}_o x_c+S_g\tilde{\rho}_g y_c \tag{2.3}$$

$$N_w=S_w\tilde{\rho}_w \tag{2.4}$$

V_b is the bulk rock volume. A is the cross section area. x_c and y_c are the mole fractions of component c in oil and gas phases. k is the absolute permeability. $k_{r\alpha}$ (α = *o, g, w*) is the phase relative permeability. Ψ_α (α = *o, g, w*) is the phase potential considering pressure and gravitational forces acting on the phase. S_α (α = *o, g, w*) is the phase saturation. $\tilde{\rho}_\alpha$ is the molar density of phase α. $n_{c,s}$ and $n_{w,s}$ are the net molar rates of component c and water from each perforation. Another primary equation is a volume constraint ensuring that total

fluid volume of each phase ($V_{\alpha,i}$) equals to the pore volume (PV_i) of each reservoir grid i. The associated primary variable is the oil phase pressure (P_o).

$$PV_i = \sum_{\alpha=o,g,w} V_{\alpha,i} \tag{2.5}$$

2.1.2 Vapor-Liquid Equilibrium

Fluid properties of oil and gas phases are calculated through vapor-liquid flash calculations based on the equation of state. We consider the component fugacity equilibrium as shown in Equation (2.6) to solve for the equilibrium ratio (K_c). The molar vapor fraction (f_v) is obtained through Rachford-Rice Equation (Rachford Jr and Rice, 1952) as given by Equation (2.7).

$$K_c = \frac{\varphi_{c,l}\, p_l}{\varphi_{c,\mathrm{v}}\, p_v} \tag{2.6}$$

$$\sum_{c=1}^{n_c} \frac{(K_c - 1) z_c}{1 + f_v (K_c - 1)} = 0 \tag{2.7}$$

z_c is the overall mole fraction of component c. $\varphi_{c,l/v}$ is the liquid and vapor fugacity coefficient of component c. $p_{l/c}$ is the liquid and vapor phase pressure. The fugacity coefficient for each phase α ($\alpha = l, v$) is calculated based on Peng-Robinson equation of state (Peng and Robinson, 1976).

$$\begin{aligned} \ln(\varphi_{c,\alpha}) = {} & \frac{b_c}{b}(\mathrm{Z}_\alpha - 1) - \ln(\mathrm{Z}_\alpha - B_\alpha) \\ & + \frac{A_\alpha}{2\sqrt{2} B_\alpha} \left[\frac{b_c}{b} - \frac{1}{a} \left(2\sqrt{a_j} \sum_{c=1}^{n_c} x_c \sqrt{a_c} (1 - \kappa_{cj}) \right) \right] \ln\left(\frac{\mathrm{Z}_\alpha + (1+\sqrt{2}) B_\alpha}{\mathrm{Z}_\alpha - (1-\sqrt{2}) B_\alpha} \right) \end{aligned} \tag{2.8}$$

Appendix A lists the definition of each parameter.

In compositional simulation, VLE calculations are conducted millions of times. Therefore, it is important to develop an efficient VLE calculation algorithm. The initial guesses of K_c and f_v are crucial to the convergence speed of VLE calculation. Wilson's correlation (Wilson, 1969) is commonly applied to estimate the value of K_c. However the correlation might give trivial solutions when pressure is high. Yan et al. (2017) introduced a compositional space method to provide initial guesses for K_c and f_v. We further combine the Successive Substitution Iteration method (SSI) and the Newton-Raphson (NR) method to solve Equations (10) and (11). The solutions from the SSI iterations are served as initial guesses for NR iterations to improve the convergence speed.

In traditional compositional reservoir models, liquid phase pressure is assumed to be equal to the vapor phase pressure, and Equation (14) can be reduced to $K_c = \varphi_{c,l}/\varphi_{c,v}$. It is a valid assumption for conventional reservoirs, which have large pore volumes. However, for shale reservoirs, whose pore sizes are in nanoscale (Kou et al., 2017), it is no longer a reasonable assumption. The nanopores in shale reservoir result in high capillary pressure and significant changes in fluid properties such as bubble-point pressure, fluid densities and viscosities (Nojabaei et al., 2013). Some researchers have reported that the high capillary pressure affects the well performance and the estimated ultimate recovery (EUR) of the reservoir (Siripatrachai et al., 2017). We will further discuss the impact of nanopore confinement on well interference phenomenon in Chapter 3.

2.1.3 Embedded Discrete Fracture Model

The Embedded Discrete Fracture Model (EDFM) is developed for Cartesian reservoir grids to achieve a higher computational efficiency for fracture modeling (Moinfar, 2013). The fractures in the model are treated as additional quadrilateral plates, which are naturally discretized by the boundary of matrix grids (Jiang and Younis, 2017). The model honors fluid flow through non-neighbor connections (NNC) between fracture segments and matrix grids, between fracture segments in a single fracture and between intersecting fractures. Transmissibility (T_{NNC}) of all three type of NNCs is generally expressed as (Chai et al., 2018):

$$T_{NNC} = \frac{k_{NNC} A_{NNC}}{d_{NNC}}, \tag{2.9}$$

where k_{NNC} , A_{NNC}, and d_{NNC} are the harmonic average of permeability, contact area and distance between the two cells in the connection. The well geometry index for wellbore-fracture connection is calculated based on Peaceman Equation (Xu et al., 2017):

$$T_w = \frac{2\pi k_f w_f}{\ln(\frac{0.14\sqrt{l^2 + h^2}}{r_w})}, \tag{2.10}$$

where k_f and w_f are permeability and width of the fracture, l and h are length and height of the fracture segment, and r_w is the wellbore radius. We apply EDFM to explicitly model fractures in the well interference study (Chapter 3). The separate grid system of EDFM enables the convenient handling of dynamic changes in fracture networks resulted from the completion of infill wells.

2.2 Fluid Flow in Wellbore

Fluid flow in wellbore can be treated with different complexities as introduced in section 1.1.3. For coupling with a reservoir simulator, whose time scale is from hours to decades, we implement a compositional NPW model with a pressure drop equation. It is also a common implementation among those reported MSW models.

2.2.1 Primary Equations

The primary equations for wellbore flow include mass conservations for each hydrocarbon component (c) and water (w) as shown in Equations (2.11) and (2.12), a pressure drop equation as shown in Equation (2.13) and a multiphase holdup constraint equation as shown in Equation (2.14). The relevant primary variables are moles of hydrocarbon component per unit volume (N_c), water holdup (y_w), mixture velocity (u_m) and average pressure of each wellbore segment (P_{seg}).

$$\nabla\left[A(x_c\tilde{\rho}_o v_{so} + y_c\tilde{\rho}_g v_{sg})\right] = V_{seg}\frac{\partial}{\partial t}(N_c) + n_{c,s} \tag{2.11}$$

$$\nabla\left[A\tilde{\rho}_w v_{sw}\right] = V_{seg}\frac{\partial}{\partial t}(N_w) + n_{w,s} \tag{2.12}$$

α_o , α_g, and α_w are oil , gas and water volumetric holdups. u_{so}, u_{sg}, and u_{sw} are superficial velocities of each phase. V_{seg} is segment volume. $\tilde{\rho}_o$, $\tilde{\rho}_g$ and $\tilde{\rho}_w$ are molar densities of each phase. The pressure drop equation is given by Equation (2.13).

$$\frac{\partial P_{seg}}{\partial z} + \frac{\partial \rho_m v_m^2}{\partial z} + \frac{f_f \rho_m v_m |v_m|}{2d_{in}} + \rho_m g\cos\theta = 0 \tag{2.13}$$

ρ_m is the mixture density given by $\rho_m = \alpha_o \rho_o + \alpha_g \rho_g + \alpha_w \rho_w$. v_m is the average mixture velocity which is the sum of gas and liquid superficial velocities. f_f is the friction factor and d_{in} is the pipe inside diameter. The second term in Equation (2.13), which represents the pressure loss due to acceleration is usually small compared to frictional (the third term) and gravitational (the fourth term) pressure losses. The constraint equation for holdup of each phase is as follows:

$$\alpha_w + \alpha_o + \alpha_g = 1. \tag{2.14}$$

The correlation between individual phase velocity and mixture velocity will be discussed in next section.

2.2.2 Homogeneous and Drift-Flux Models

GURU-MSW implements homogeneous and drift-flux models for multi-phase flow characterization in wellbore. The homogeneous model assumes all the phases move in the same speed. The in-situ flow velocity for each phase is correlated as:

$$v_p = v_m \ (p = o, g, w) \tag{2.15}$$

The superficial phase velocity of each phase is then expressed as:

$$v_{sp} = \alpha_p v_m \ (p = o, g, w) \tag{2.16}$$

The homogeneous model is unconditionally stable within a Newton-Raphson solver. However, the model ignores the slip among phases, and thus fails to accurately predict the in-situ phase volume fractions.

On the contrary, drift-flux models are considered to be fairly accurate for gas volume fraction prediction in gas-liquid two phase flow (Bhagwat and Ghajar, 2014; Woldesemayat and Ghajar, 2007). The drift-flux model has been introduced in section 1.1.3. We rewrite the general model expression for three-phase application as follows:

$$v_g = C_0^{gl} v_m + v_d^{gl} \tag{2.17}$$

$$v_{sl} = v_m - v_g \alpha_g \tag{2.18}$$

$$v_o = C_0^{ow} v_{sl} + v_d^{ow} \tag{2.19}$$

$$v_{so} = v_o \frac{\alpha_o}{\alpha_o + \alpha_w} \tag{2.20}$$

$$v_{sw} = v_{sl} - v_{so} \tag{2.21}$$

C_0 and u_d are can both be a constant or an empirical correlation determined by experimental data. Although, there are a lot of different drift-flux models in the literature, few of them can be compatible with a Newton-Raphson non-linear solver and a fully-implicitly coupled wellbore-reservoir simulator. The following crucial points are summarized based on our experiences (Hewei Tang et al., 2017) : (1) the model needs to be continuous and differentiable within the whole range of primary variables; and (2) the model needs to be based on mixture velocity (v_m) rather than gas superficial velocity (v_{sg}). The first points comes from the restriction of applying the Newton-Raphson method. The third point comes from the intrinsic logic behind the fully implicit method, which is to solve the primary variables (i.e. mixture velocity and liquid holdup) first, and then update

secondary variables (i.e. individual phase velocities) with auxiliary equations such as the drift-flux model. These three restrictions make most flow-pattern based drift-flux models inapplicable.

2.2.3 Auxiliary Equations

The reservoir model and wellbore model are coupled through the sink and source terms $n_{c,s}$ and $n_{w,s}$ in Equations. (2.11) and (2.12). We assume that the reservoir pressure at the wellbore-reservoir interface equals to the wellbore segment pressure at the interface. The net molar rates $n_{c,s}$ and $n_{w,s}$ are calculated as shown in Equations (2.22) and (2.23).

$$n_{c,s} = T_w[\lambda_o x_c(P_{o,res} - P_{seg}) + \lambda_g y_c(P_{g,res} - P_{seg})] \tag{2.22}$$

$$n_{w,s} = T_w \lambda_w (P_{w,res} - P_{seg}) \tag{2.23}$$

T_w is the well geometry index. We evaluated T_w through Peaceman equation, which assumes that well penetrates through the center of the reservoir grid block, perpendicular to two of its faces (Peaceman, 1978). For a horizontal well in x direction, T_w is given as:

$$T_w = 2\pi \frac{\Delta x \sqrt{k_y k_z}}{\ln(\frac{r_o}{r_w}) + S} \tag{2.24}$$

With,

$$r_o = 0.28 \frac{\left(\Delta y^2 \sqrt{k_z / k_y} + \Delta z^2 \sqrt{k_y / k_z}\right)^{1/2}}{\sqrt[4]{k_y / k_z} + \sqrt[4]{k_z / k_y}} \tag{2.25}$$

Δx, Δy, and Δz are dimensions of grids, k_x, k_y, and k_z are permeability in each direction, r_w is wellbore radius, and S is skin factor.

In Equations. (2.22) and (2.23), λ_p (p = o, g, w) is the phase mobility, which is evaluated based on the flow direction. For production scenario ($P_{o,res} > P_{seg}$), the phase mobility is evaluated at perforated cells.

$$\lambda_p = k_{rp} \frac{\tilde{\rho}_p}{\mu_p} \tag{2.26}$$

For injection scenario ($P_{o,res} < P_{seg}$), the phase mobility is evaluated through the total mobility at perforated cells and the fluid properties at perforated well segments (Holmes, 1983).

$$\lambda_p = \left(\frac{k_{ro}}{\mu_o} + \frac{k_{rg}}{\mu_g} + \frac{k_{rw}}{\mu_w} \right) \tilde{\rho}_p \alpha_p \tag{2.27}$$

The frictional factor in Equation (2.13) is calculated as (Economides et al., 2012):

$$f_m = \left\{ 4 \log \left\{ \frac{\varepsilon}{3.7065} - \frac{5.0452}{N_{\mathrm{Re}}} \log \left[\frac{\varepsilon^{1.1098}}{2.8257} + \left(\frac{7.149}{N_{\mathrm{Re}}} \right)^{0.8981} \right] \right\} \right\}^{-2}, \tag{2.28}$$

where ε is the relative pipe roughness. N_{Re} is the Reynolds number calculated as:

$$N_{Re} = \frac{v_m \rho_m d_{in}}{\mu_l} \tag{2.29}$$

In Equation (2.14), gas and oil holdups (y_g and y_o) can be correlated as follows:

$$\alpha_g = \frac{f_v \times \sum N_c}{\tilde{\rho}_g} \tag{2.30}$$

$$\alpha_o = \frac{(1-f_v)\times\sum N_c}{\tilde{\rho}_o} \tag{2.31}$$

2.3 Numerical Implementation

2.3.1 Residual Equations

The compositional reservoir model is spatially discretized base on control-volume finite-difference method proposed by Cao (2002) with a two-point flux approximation. This method allows the convenient handling of unstructured reservoir grids. For time discretization, a fully implicit scheme is applied. The mass balance residual equations of the hydrocarbon component (c) and the water component (w) in cell *i* are shown in Equations. (2.32) and (2.33). The volume balance residual equation of cell *i* is shown in Eq. (2.34).

$$R_{c,i} = \frac{V_b\phi^{n+1}}{\Delta t}(N_{c,i}^{n+1} - N_{c,i}^{n}) - \sum_s T_s\left(\frac{k_{ro}}{\mu_o}x_c\tilde{\rho}_o\nabla\psi_o + \frac{k_{rg}}{\mu_g}y_c\tilde{\rho}_g\nabla\psi_g\right)^{n+1} - n_{c,s,i}^{n+1} = 0 \tag{2.32}$$

$$R_{w,i} = \frac{V_b\phi^{n+1}}{\Delta t}(N_{w,i}^{n+1} - N_{w,i}^{n}) - \sum_s T_s\left(\frac{k_{rw}}{\mu_w}x_c\tilde{\rho}_w\nabla\psi_w\right)^{n+1} - n_{w,s,i}^{n+1} = 0 \tag{2.33}$$

$$R_{v,i} = S_{o,i} + S_{g,i} + S_{w,i} - 1 = 0 \tag{2.34}$$

The wellbore model is also discretized based on finite volume methods along the axial direction of the wellbore. A staggered grid arrangement as shown in Figure 2.1 is adopted. Scalar variables such as pressure and phase holdup are solved at the center of each well segment, while velocities are solved at the face of each well segment to avoid spurious pressure oscillations (Prosperetti and Tryggvason, 2009; Yoshida, 2016).

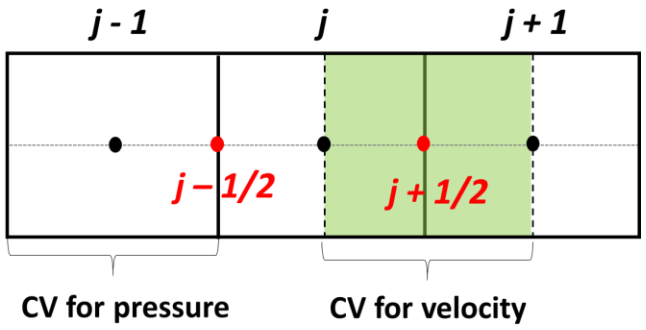

Figure 2.1 Schematic for the staggered grid arrangement and corresponding control volumes (CV).

The residual equations of mass conservation, pressure drop, and volume balance are given by Equations (2.35) to. (2.38).

$$R_{c,j} = \frac{V_{seg}}{\Delta t}(N_{c,j}^{n+1} - N_{c,j}^{n}) + \left[(Ax_c\tilde{\rho}_o v_{so})_{j-1/2} + (Ay_c\tilde{\rho}_g v_{sg})_{j-1/2}\right]^{n+1} - \left[(Ax_c\tilde{\rho}_o v_{so})_{j+1/2} + (Ay_c\tilde{\rho}_g v_{sg})_{j+1/2}\right]^{n+1} - n_{c,s,j} \tag{2.35}$$

$$R_{w,j} = \frac{V_{seg}}{\Delta t}(N_{w,j}^{n+1} - N_{w,j}^{n}) + [(A\tilde{\rho}_w v_{sw})_{j-1/2}]^{n+1} - [(A\tilde{\rho}_w v_{sw})_{j+1/2}]^{n+1} - n_{w,s,j} \tag{2.36}$$

$$R_{p,j+1/2} = (P_{j+1} - P_j) + \rho_{m,j+1/2} g(h_{j+1} - h_j) + \left(\frac{f_{tr}\rho_m v_m |v_m| L}{2D}\right)_{j+1/2} \tag{2.37}$$

$$R_{v,j} = \alpha_{w,j} + \alpha_{o,j} + \alpha_{g,j} - 1 \tag{2.38}$$

The pressure loss due to acceleration is ignored because it is usually small compared to frictional and gravitational pressure losses, especially for uniform pipe diameter. $\rho_{m,j+1/2}$ in the potential term is evaluated based on the volume averaged method. For other flux

related terms, a donor-cell approach is applied to evaluate the secondary variables (i.e., α, x, y, ρ) at well segment faces (Prosperetti and Tryggvason, 2009). The approach is presented in Eq. (2.39) with α_w as an example. The production direction is defined as a positive velocity direction.

$$\alpha_{w,j+1/2} = \frac{1}{2}(1+\mathrm{sgn}(v_{w,j+1/2}))\alpha_{w,j+1} + \frac{1}{2}(1-\mathrm{sgn}(v_{w,j+1/2}))\alpha_{w,j} \tag{2.39}$$

2.3.2 Boundary Conditions

The no-flow boundary condition is applied in the reservoir model. For the wellbore model, we also apply a no-flow boundary at the bottom of the wellbore. At the wellhead, the boundary condition is applied by replacing R_p with constraint residuals defined by different control strategies. We honor both pressure constraints and rate constraints of different phases in GURU-MSW. For the pressure constraint, we consider the gravitational and frictional pressure loss between the segment pressure and the target well head pressure (P^*) as shown in Equation (2.40).

$$R_{p,1} = P_{1,seg} - P^* - \left(\frac{\rho_m g L \sin(\theta)}{2}\right)_1 - \left(\frac{f_f \rho_m v_m |v_m| L}{4 d_{in}}\right)_1 \tag{2.40}$$

In standard well model, the rate constraint equations are calculated by equaling the sum of flow rate from all perforations to the specific rate. Equation (2.41) gives an example of constant oil rate control ($Q^*_{v,o}$).

$$R_{well} = \frac{(\sum_{perf} \tilde{Q}_o + \sum_{perf} \tilde{Q}_g)(1 - f_v^{sc})}{\tilde{\rho}_o^{sc}} - Q^*_{v,o} \tag{2.41}$$

Based on the analysis of Jiang (2008), writing rate constraint equation in the above format may impose difficulties to ILU preconditioner and ignore transient wellbore effects such as wellbore storage. Therefore, we adopt another format of constraint equations that are based on the superficial phase velocities of the first wellbore segment. Equations (2.42) to (2.45) show the residual equations for constant oil surface volume rate control, constant gas surface volume rate control, constant water surface volume rate control and constant liquid surface volume rate control.

$$R_{p,1} = \frac{A_{1,seg}(\tilde{\rho}_o v_{so} + \tilde{\rho}_g v_{sg})_1 (1 - f_v^{sc})}{\tilde{\rho}_o^{sc}} - Q_{v,o}^* \tag{2.42}$$

$$R_{p,1} = \frac{A_{1,seg}(\tilde{\rho}_o v_{so} + \tilde{\rho}_g v_{sg})_1 f_v^{sc}}{\tilde{\rho}_g^{sc}} - Q_{v,g}^* \tag{2.43}$$

$$R_{p,1} = \frac{A_{1,seg}(\tilde{\rho}_w v_{sw})_1}{\tilde{\rho}_w^{sc}} - Q_{v,w}^* \tag{2.44}$$

$$R_{p,1} = \frac{A_{1,seg}(\tilde{\rho}_o v_{so} + \tilde{\rho}_g v_{sg})_1 (1 - f_v^{sc})}{\tilde{\rho}_o^{sc}} + \frac{A_{1,seg}(\tilde{\rho}_w v_{sw})_1}{\tilde{\rho}_w^{sc}} - Q_{v,l}^* \tag{2.45}$$

When multiple constraints exist, the active boundary condition is decided by selecting the constraint with the largest violation factor (Watts et al., 2012). The violation factors for producing rate constraint and pressure constraint are defined in Equations (2.46) and (2.47) respectively.

$$\beta_Q = \frac{Q_{seg1}}{Q^*} \tag{2.46}$$

$$\beta_p = \frac{P^*}{P_{seg1}} \tag{2.47}$$

2.3.3 Initialization of MSW

Small time step and good initial values are important to properly begin the simulation. Contrary to the standard wellbore model, which only has one variable, the multi-segment well model has n_h+2 (considering there are n_h compositions) primary variables in each wellbore segment. All these primary variables need to be assigned proper initial values to guarantee the convergence of Newton-Raphson solver. We implement the following steps to determine these initial values:

(1) We assume the initial composition of each wellbore segment is the same as that in the reservoir.

(2) Estimate wellbore pressure. If the well is under constant pressure control, the wellbore pressure is set as the constant wellbore pressure. If the well is under a constant rate control (given oil rate control as an example), the wellbore pressure is estimated as follows:

$$P_{well} = \frac{\sum_{perf} (T_w \lambda_o P_o + T_w \lambda_g P_g) \frac{(1 - f_v^{sc})}{\tilde{\rho}_o^{sc}} - Q_{v,o}^*}{\frac{(1 - f_v^{sc})}{\tilde{\rho}_o^{sc}} \sum_{perf} (T_w \lambda_o + T_w \lambda_g)} \tag{2.48}$$

The mixture fluid density inside the wellbore is then estimated by summing up the flow influx from each wellbore perforations. The pressure of each wellbore segment is finally determined by adding gravitational effect to the reference wellbore pressure.

(3) Estimate holdups. The holdups in each wellbore segment are estimated by summing up the flow influx ratios from all the upstream perforations.

(4) Estimate mixture velocity. The mixture velocity of each wellbore segment is estimated by summing up the flow influx from all the upstream perforations.

The individual phase velocity is assumed to be equal to the mixture velocity. In other words, homogeneous model is applied for the initialization of MSW to ensure the convergence.

2.3.4 Global Linear System and Jacobian Matrix

Table 2.1 summarizes the primary residual equations and variables in the coupled wellbore-reservoir simulation. For n_h hydrocarbon components being considered, there are $(n_h + 2) \times nCells$ primary equations for the reservoir system and $(n_h + 2) \times nSegs + nSegConnes$ primary equations for the wellbore system.

System	Residual Equations	Variables	Number	Total
Reservoir	Hydrocarbon component mass balance ($R_{c,i}$)	$N_{c,i}$	$n_h \times nCells$	$(n_h + 2) \times nCells$
	Water mass balance ($R_{w,i}$)	$N_{w,i}$	$1 \times nCells$	
	Volume balance ($R_{v,i}$)	$P_{o,i}$	$1 \times nCells$	
Wellbore	Hydrocarbon component mass balance ($R_{c,j}$)	$N_{c,j}$	$n_h \times nSegs$	$(n_h + 2) \times nSegs + nSegConnes$
	Water mass balance ($R_{w,j}$)	$\alpha_{w,j}$	$1 \times nSegs$	
	Volume balance ($R_{v,j}$)	P_{seg}	$1 \times nSegs$	
	Pressure drop ($R_{p,j}$)	v_m	$1 \times nSegConnes$	

Table 2.1–Summary of primary equations and variables in GURU-MSW

The Newton-Raphson method is applied to solve all the primary variables. For a single equation, the method can be expressed as:

$$x_{n+1} = x_n - \frac{f(x_n)}{f'(x_n)}. \tag{2.49}$$

For a set of nonlinear equations, the method can be expressed as a global linear system including a Jacobian matrix, a vector of primary variables changes, and a vector of residual equations, as shown in Eq. (2.50):

$$\begin{bmatrix} \frac{\partial \vec{R}_{res}}{\partial \vec{x}_{res}} & \frac{\partial \vec{R}_{res}}{\partial \vec{x}_{well}} \\ \frac{\partial \vec{R}_{well}}{\partial \vec{x}_{res}} & \frac{\partial \vec{R}_{well}}{\partial \vec{x}_{well}} \end{bmatrix} \begin{bmatrix} \delta \vec{x}_{res} \\ \delta \vec{x}_{well} \end{bmatrix} = \begin{bmatrix} \vec{R}_{res} \\ \vec{R}_{well} \end{bmatrix} \tag{2.50}$$

The vectors of independent variables are constructed from primary reservoir variables ($\vec{x}_{res} = [N_c, N_w, P_o]_{\forall i}$) and primary wellbore variables ($\vec{x}_{well} = [N_c, \alpha_w, P_{seg}, v_m]_{\forall j}$). The vectors of residuals are constructed from the residuals of reservoir governing equations ($\vec{R}_{res} = [R_c, R_w, R_v]_{\forall i}$) and residuals of wellbore governing equations ($\vec{R}_{well} = [R_c, R_w, R_v, R_p]_{\forall j}$). The Jacobian matrix is made of four components: the derivation of reservoir residual equations with respect to reservoir variables ($J_{RR} = \partial \vec{R}_{res} / \partial \vec{x}_{res}$), the derivation of reservoir residual equations with respect to wellbore variables ($J_{RW} = \partial \vec{R}_{res} / \partial \vec{x}_{well}$), the derivation of wellbore residual equations with respect to reservoir variables ($J_{WR} = \partial \vec{R}_{well} / \partial \vec{x}_{res}$), and the derivation of wellbore residual equations with respect to wellbore variables ($J_{WW} = \partial \vec{R}_{well} / \partial \vec{x}_{well}$). Because of the staggered grid discretization scheme, the wellbore residual equations related with mass balance and

volume balance are ordered first based on the segment list, following by the pressure drop equation based on the segment connection list. Therefore, the J_{ww} portion can be further split as follows:

$$J_{ww} = \begin{bmatrix} \frac{\partial \vec{R}_{well,s}}{\vec{x}_{well,s}} & \frac{\partial \vec{R}_{well,s}}{\vec{x}_{well,c}} \\ \frac{\partial \vec{R}_{well,c}}{\vec{x}_{well,s}} & \frac{\partial \vec{R}_{well,c}}{\vec{x}_{well,c}} \end{bmatrix} \tag{2.51}$$

$\vec{R}_{well,s}$ is the vector of residuals related with well segments, $\vec{R}_{well,c}$ is the vector residuals related with well connections, $\vec{x}_{well,s}$ is the vector of variables related with well segments, and $\vec{x}_{well,c}$ is the vector of variables related with well connections. This arrangement allows the flexible extension of current MSW model to surface network model.

Similar to the idea of applying a connection list for unstructured reservoir grid handling, we also generate a connection list for wellbore segments in GURU-MSW. Segments from different wells are constructed into a single wellbore segment array, and the connection list documents the connectivity among different wellbore segments. Based on this data structure, GURU-MSW can handle complex well geometries like branches and loops, multiple wellbores. In GURU-MSW, each well can either be defined as a standard well or a multi-segment well, and multiple wells can also be grouped to a junction point where production constraints for the entire well group being applied.

Figure 2.2 shows a sample Jacobian matrix with 5 × 1 reservoir cells and 8 wellbore segments. There are 2 hydrocarbon components in total. The 8th wellbore segment perforates the 5th reservoir cell. The dash lines separate the entries of Jacobian

matrix into different reservoir cells and wellbore segments. There are four primary variables/residuals for each reservoir cell and wellbore segment. The red line separate the Jacobian matrix into four portions: J_{RR}, J_{RW}, J_{WR} and J_{WW}. The dimension of Jacobian matrix is 60 × 60 with the dimension of J_{RR} being 20 × 20 and the dimension of J_{WW} being 40 × 40. The green lines further separate the J_{WW} into segment based residuals and connection based residuals.

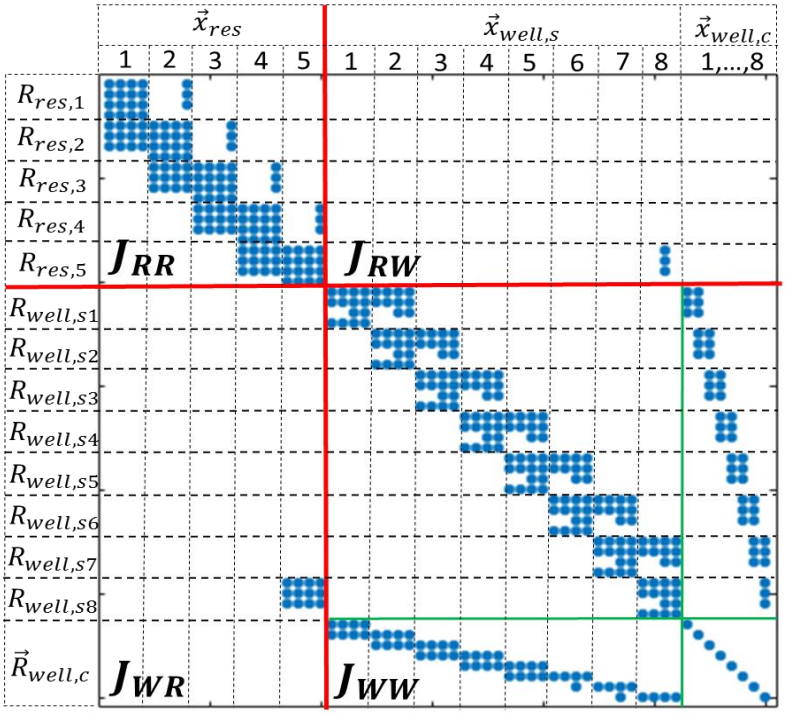

Figure 2.2–A sample Jacobian matrix of GURU-MSW.

A Gaussian Elimination method is applied to solve the global linear system shown in Eq. (2.50) (Cao et al., 2015).

$$(J_{RR} - J_{RW} \cdot J_{WW}^{-1} \cdot J_{WR}) \cdot \vec{x}_{res} = \vec{R}_{res} - J_{RW} \cdot J_{WW}^{-1} \cdot \vec{R}_{well} \tag{2.52}$$

$$J_{WW} \cdot \vec{x}_{well} = \vec{R}_{well} - J_{WR} \cdot \vec{x}_{res} \tag{2.53}$$

The linear solvers available in GURU-MSW are direct solver, conjugate gradient solver, GMRES solver, and BiCGSTAB solver. ILU preconditioners are applied for the last three solvers.

2.4 Simulation Workflow

As introduced in Section 1.1.1, GURU-MSW is developed based on the in-house compositional reservoir simulator GURU. The newly added wellbore modules include input module, initialization module, fluid module, governing equation module, and output module as shown in Figure 2.3. Several important subroutines, such as vapor liquid equilibrium (VLE) calculation and phase velocity calculation are all included in the fluid module. The wellbore equation module includes the subroutines of assembling wellbore governing equations and calculating the other three portions of the Jacobian matrix. Ultimately, the original linear solver module is modified to handle the global linear system constructed by wellbore and reservoir equations.

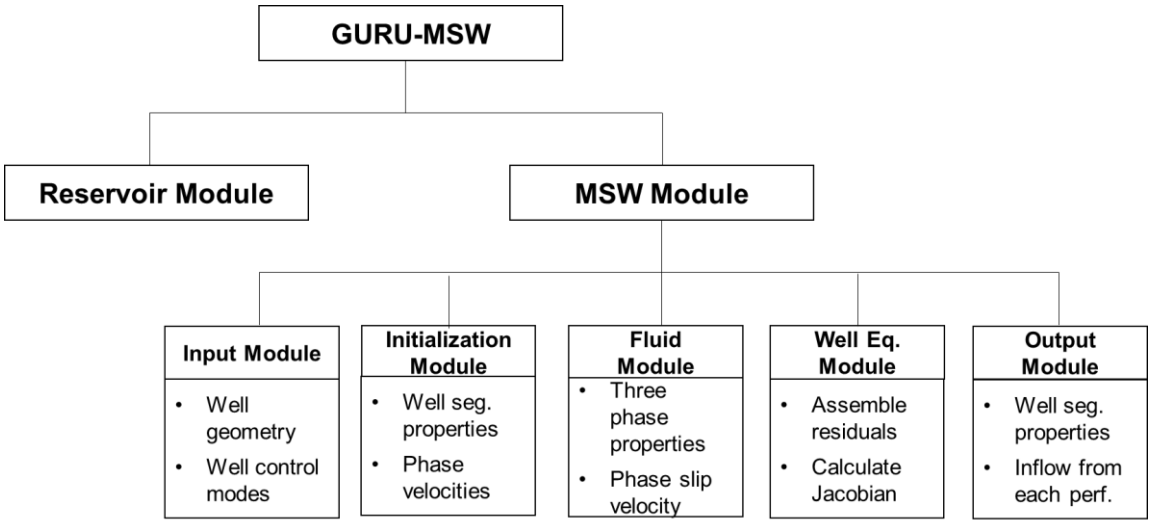

Figure 2.3–Newly added modules in GURU-MSW.

Figure 2.4 shows the simulation flowchart of GURU-MSW. After reading the reservoir and wellbore input files, the program performs miscellaneous calculation to examine the bad inputs and to give notifications. Next, the initialization of both reservoir cells and wellbore segments variables are conducted based on the input. The initialization data are then passed to the time-step level. For each time step, the program enters newton iteration with the initial guess of primary variables. The global linear system is constructed based on the assembled residual equations and Jacobian matrix and sent to the linear solver module. The updated primary variables are sent to the quality check module. If there are any unphysical values, the program breaks out of the newton loop and cuts the time step. If the new primary variables pass the quality check, they re-enter the newton loop until convergence criteria are met. The converged results of the time step are output into the data files. The program enters next time step with the converged results of previous time step as initial guess. The simulation is end when the target time is reached.

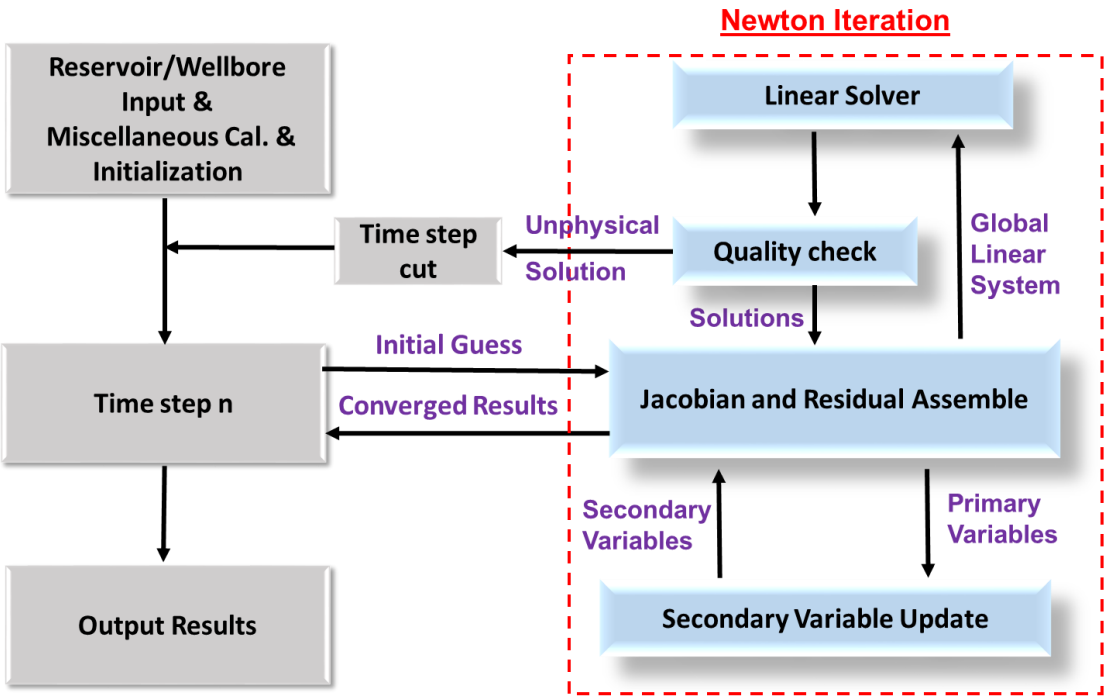

Figure 2.4–Simulation flowchart of GURU-MSW

3. WELL INTERFERENCE STUDY IN SHALE RESERVOIR*

Well interference is a common phenomenon in unconventional reservoir development. The completion and production of infill wells can lead to either positive or negative well interference impacts on the existing producers. Many researchers have investigated the well interference phenomenon; however, few of them attempted to apply rigorous simulation methods to analyze both positive and negative well interference effects, especially in two different formations. In this chapter, we apply the newly developed wellbore-reservoir simulator GURU-MSW to study the well interference phenomena in Eagle Ford Shale – Austin Chalk production system. For this application, we consider the fluid flow inside the wellbore to be homogeneous.

---

*Part of this section is reprinted with permission from "Analyzing the Well Interference Phenomenon in Eagle Ford Shale – Austin Chalk Production System with a Comprehensive Compositional Reservoir Model" by H. Tang, B. Yan, Z. Chai, et al. SPE Reservoir Evaluation and Engineering, Copyright [2018] by Society of Petroleum Engineer.

3.1 Introduction

3.1.1 Well Interference Phenomenon

Massive and complex hydraulic fractures created by drilling multiple well pads and multi-stage hydraulic fracturing lead to the successful development of unconventional reservoirs(Xue et al., 2016; Zhang and Zhu, 2017; Zhang et al., 2018ab). However, as well spacing decreases, the extensive fractures from adjacent wells also increase the chance of "fracture hits" and result in well interference.

Previous studies have varying definitions for fracture hits. We subdivide these definitions into two categories based on the places where fracture hits happen. The first category of fracture hit happens in the near wellbore region of parent wells. It can result in the removal of considerable amount of proppants in hydraulic fractures or wellbore failures (Fjar et al., 2008). Therefore, this kind of fracture hits often leads to mild or severe negative impacts on the production of existing parent wells (Marongiu-Porcu et al., 2016). The second category of fracture hits happens in the stimulated reservoir volume (SRV) of parent wells. The feature of this kind of fracture hit is the creation of hydraulic connections as the fractures of infill wells propagate and hit the fractures of parent wells. This kind of fracture hit leads to either a positive or negative impact to the production of existing parent wells, while the negative impact is much more common based on field observations (Ajani and Kelkar, 2012; Kurtoglu and Salman, 2015). The scope of this study focuses on simulating the production impacts of the second category of fracture hits.

Yu et al. (2017) simulated the production of multiple wells under well interference by use of a compositional reservoir model. Their model was able to characterize the

complex geometry of hydraulic and natural fractures. However, they only presented the cumulative production of several interference wells in a single reservoir and did not investigate the impact of well interference on existing producers. We consider this investigation as important, especially for parent wells and infill wells completed in different formations, such as Eagle Ford Shale and Austin Chalk, since the wells very likely belong to different operators.

3.1.2 Eagle Ford Shale and Austin Chalk Formations

The Eagle Ford Shale formation locates in Western Gulf Basin, South Texas. It overlies the Buda limestone and underlies the Austin Chalk. The Eagle Ford Shale is a self-sourced reservoir with seals. Hentz and Ruppel (2010) divided the Eagle Ford Shale formation into the Lower Eagle Ford and the Upper Eagle Ford. The Lower Eagle Ford, which is present throughout the whole area of the play, has higher gamma ray and resistivity responses, reflecting its richness in organic matter. On the other hand, the Upper Eagle Ford is restricted to the west region of the play, and it has more carbonate. The elevation of the Eagle Ford Shale formation decreases from 3,500ft subsea to 14,000ft subsea southwestward. As the basin gets deeper and more thermally mature, the Eagle Ford fluids exhibit an evolution from oil, gas condensate and to dry gas (Energy Information Agency, 2010). The reservoir properties also vary a lot across the play, with porosity ranging between 2% and 10% and permeability ranging between 0.1nd and 1000nd (Siripatrachai et al., 2017; Walls and Sinclair, 2011). Commercial production in

the Eagle Ford Shale was first obtained in 2008 with a combination of horizontal drilling and hydraulic fracturing (Tunstall, 2015).

The Austin Chalk formation extends from southern Louisiana to south-central Texas. The Austin Chalk is a tight oil reservoir with the Eagle Ford Shale being its source rock. Hydrocarbons sourced from the Eagle Ford Shale charge the Austin Chalk reservoirs through vertical migration pathways formed by fracture networks (Pearson, 2010). The matrix porosity of the Austin Chalk reservoir is between 3% and 10% and the matrix permeability is between 0.03 and 1.27mD (Hovorka, 1998). The Austin Chalk has been a target of numerous horizontal wells since the late 1980's (Martin et al., 2011).

Martin et al. (2011) studied the production system formed by the Austin Chalk and the Eagle Ford Shale from the perspectives of geological features and production activities. They proved the possibility that the two formations form a single hydrocarbon system. Okeahialam et al. (2017) investigated the well production performance of the Eagle Ford Shale play in Gonzales and Lavaca counties. In this region, the Upper Eagle Ford has pinched out, and the Austin Chalk is directly above the Lower Eagle Ford. They observed that the oil production rate of a parent well in the Austin Chalk formation increased significantly after an infill well in the Eagle Ford Shale started to produce, as shown in Figure 3.1. This field case reveals that although the positive well interference effect is not common, it does happen in the Eagle Ford Shale-Austin Chalk production system.

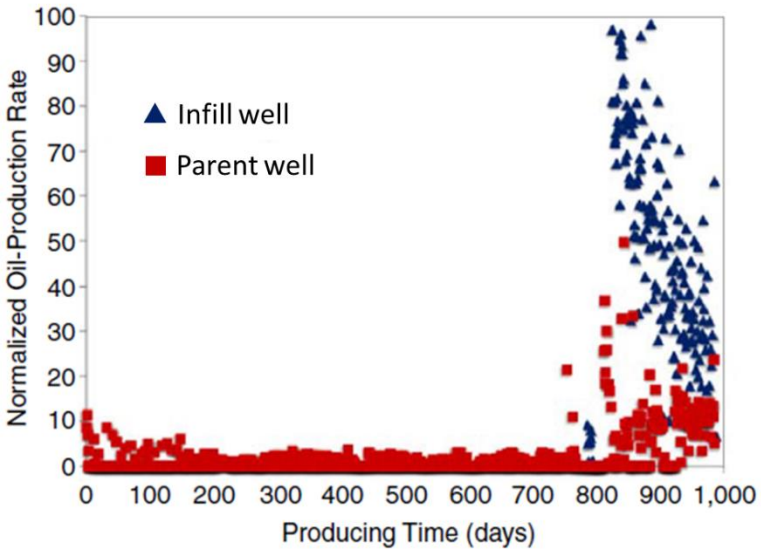

Figure 3.1–Normalized production rates of a parent well in the Austin Chalk formation and an infill well in the Eagle Ford Shale formation (reprinted from Okeahialam et al. 2017).

3.2 Model Verification

A 3D synthetic reservoir model is set up to represent the Eagle Ford Shale - Austin Chalk production system (Figure 3.2). The reservoir has a dimension of 3000ft × 1000ft × 300ft and three equal-size layers (100ft) in the vertical direction. The top layer (layer 1) represents the Austin Chalk formation and the bottom two layers (layers 2 and 3) represent the Eagle Ford Shale formation. A horizontal well (represented by black line) with four planar hydraulic fractures (represented by red lines) is completed in the Austin Chalk formation. The half-length of the fractures is 250ft. We assume these fractures penetrate through layer 1 with a height of 100ft. Table 3.1 lists all reservoir properties and well control parameters of the model. We assume the vertical permeability equals to the horizontal permeability in the two formations. A separate study indicates that the vertical

permeability does not influence the competitive drainage between parent and infill wells in the production system. We honor two production constraints simultaneously, one is a maximum production rate control of 2000 STB/day and the other is a minimum bottom-hole pressure (BHP) control of 2000 psia. Because most hydrocarbon in Austin Chalk is sourced from Eagle Ford Shale, we assume they share the same fluid compositions. We apply the five pseudo-components for Eagle Ford Shale (CO_2, N_2-C_1, C_2-C_5, C_6-C_{10}, C_{11}) reported by Yu et al. (2017), whose molar fractions and properties are listed in Table 3.2. The binary interaction parameters among components are the same as those in the original publication. The relative permeability curves for matrix and fractures in Austin Chalk are shown in Fig. 3.3 (Valbuena Olivares, 2015). The Stone II (1973) method is applied to calculate the three phase relative permeability. The capillary pressures between oil and water phases and between gas and oil phases in the Eagle Ford shale layers are shown in Fig. 3.4. For this verification case, we only consider the impacts of capillary pressure on flow behavior.

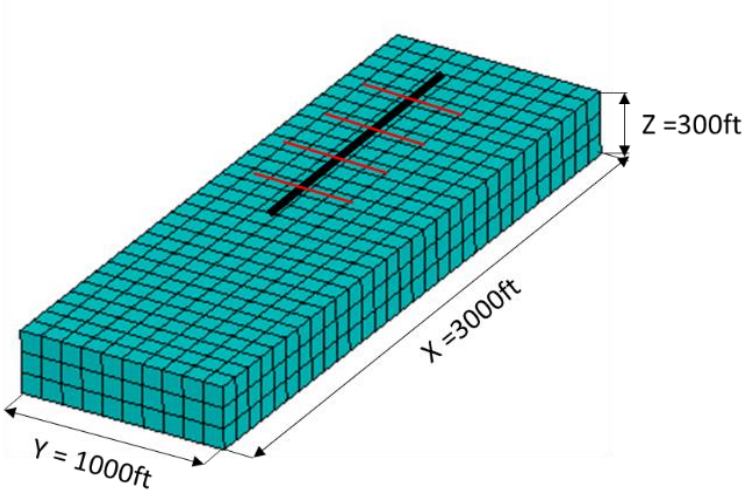

Figure 3.2–3D reservoir layout of the synthetic case for verification.

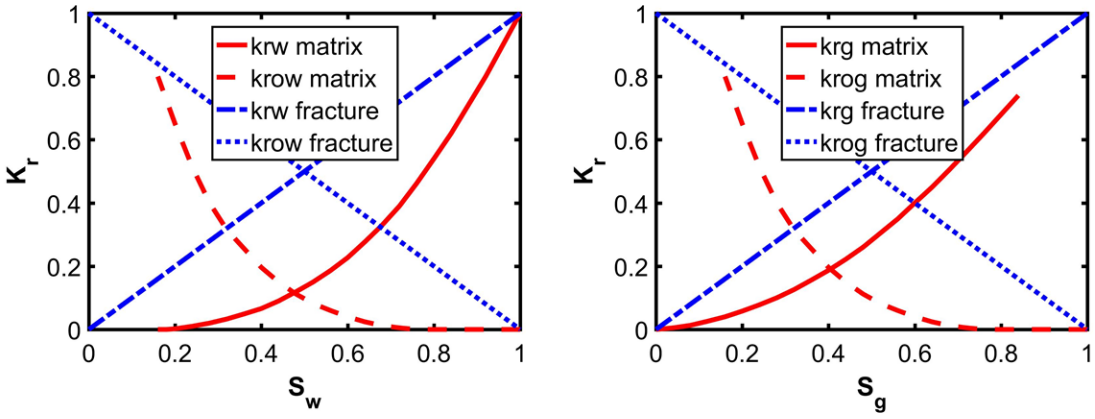

Figure 3.3–Relative permeability curves for rock matrix and fractures in the Austin Chalk (modified after Valbuena Olivares, 2015).

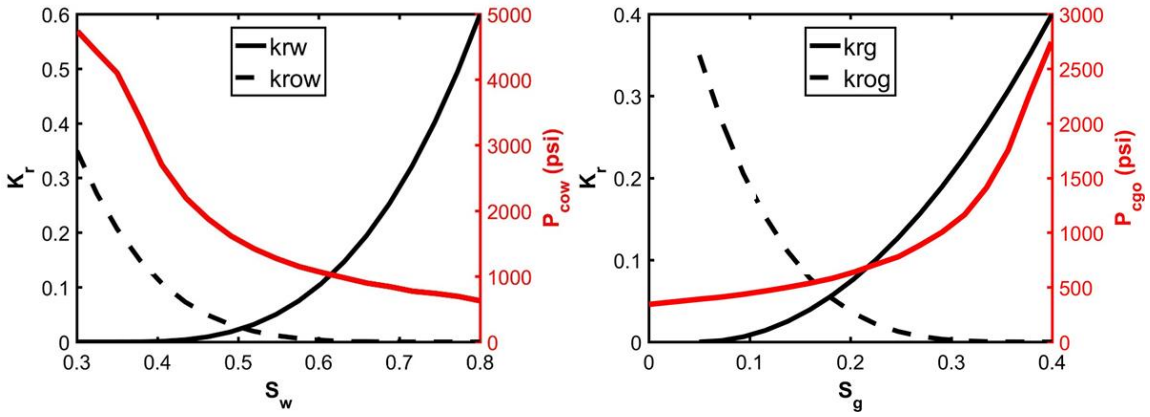

Figure 3.4–Relative permeability curves and capillary pressure curves for rock matrix in the Eagle Ford Shale (modified after Agboada et al., 2013).

Parameter	**Value**	**Units**
Initial reservoir pressure (layer 1)	8000	psi
Reservoir pressure gradient	0.45	psi/ft
Initial water saturation	0.3	-
Reservoir temperature	270	F
Rock matrix porosity	0.1	-
Rock matrix permeability (layer 1)	0.18	mD
Rock matrix permeability (layers 2 and 3)	450	nD
Rock compressibility	4×10^{-6}	psi^{-1}
Fracture width	0.1	ft
Fracture porosity	0.3	-
Fracture permeability	1000	mD
Fracture half-length	250	ft
Wellbore diameter	0.5	ft
Maximum oil producing rate	2000	STB/day
Minimum bottom hole pressure (BHP)	2000	psia

Table 3.1–Parameters for the synthetic case.

Component	Molar fraction	Molar weight	Acentric factor	Critical pressure (psia)	Critical temperature (°F)	Critical volume (ft^3/mol)
CO_2	0.2506	44.01	0.2250	1069.86	87.89	1.506
N_2-C_1	0.2200	16.21	0.0084	664.84	-118.26	1.584
C_2-C_5	0.2000	52.02	0.1723	472.77	155.46	3.672
C_6-C_{10}	0.1300	103.01	0.2839	360.20	419.77	6.315
C_{11+}	0.1994	304.39	0.6716	222.20	1097.33	14.206

Table 3.2–Component properties for Eagle Ford Shale fluid (modified after Yu et al. 2017).

We validate the compositional reservoir model applying EDFM against ECLIPSE 300 applying the local grid refinement (LGR) method for fracture modeling. To resemble the actual production process, the well is produced under a maximum oil producing rate constraint of 2000 STB/day and a minimum bottom-hole pressure of 2000 psi. Simulation results of bottom-hole pressure, oil producing rate and gas producing rate are compared in Figure. 3.5(a) through (c). All the results are in excellent agreement, which demonstrates the reliability of compositional simulation in GURU-MSW and the EDFM fracture modeling technique.

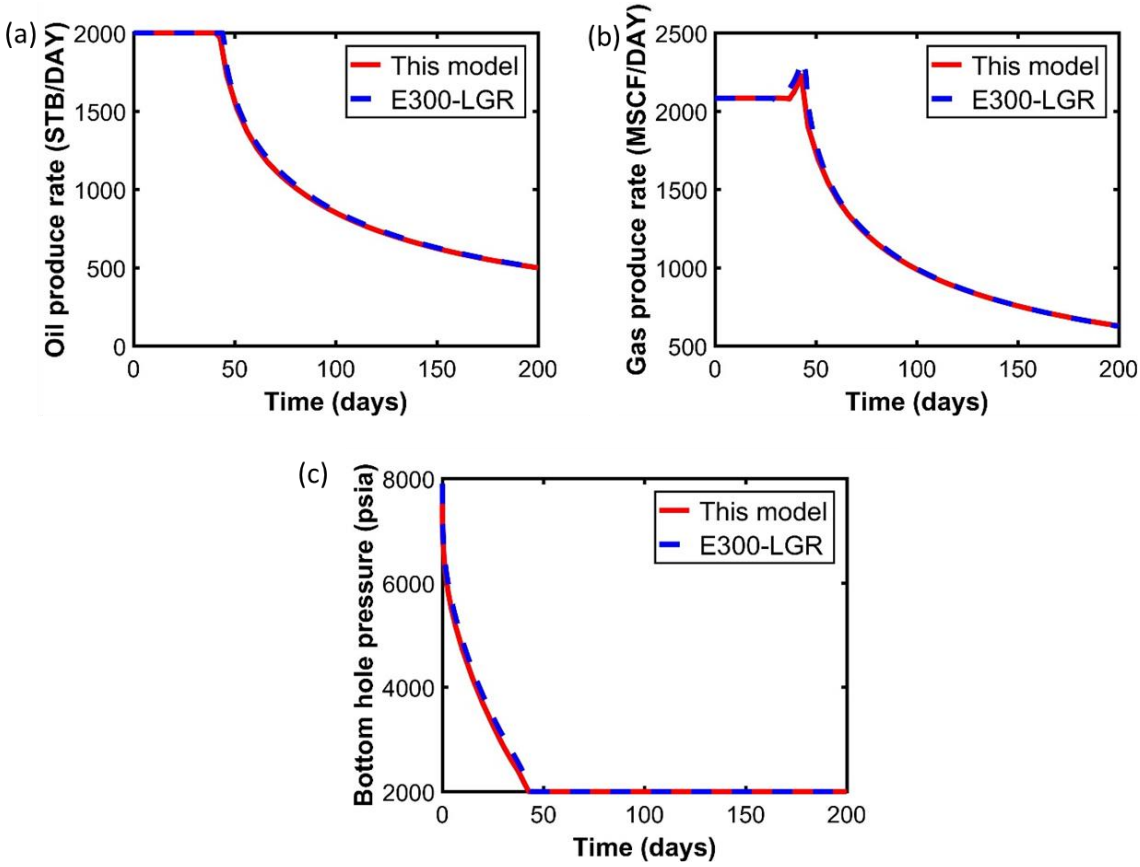

Figure 3.5–Results comparison of (a) oil production rate, (b) gas production rate, and (c) bottom hole pressure between GURU-MSW and ECLIPSE 300.

3.3 Case Studies

3.3.1 Effect of Different Well Interference Scenarios

To evaluate the impact of infill wells in the Eagle Ford Shale formation on the production of parent wells in the Austin Chalk formation, we design three different well interference cases shown in Figure 3.6. For all three cases, the parent well in the Austin Chalk layer is the same as that in the base case, and the infill well in the Eagle Ford Shale layer is completed in the third layer of the synthetic model. The two wells in the Austin

Chalk formation and the Eagle Ford Shale formation are placed staggered vertically. All existing fractures of the parent well are marked as red lines, and the new fractures of the infill well are marked as green lines. The infill well has nine stages of fractures. In case 1, nine planar fractures of the infill well penetrate through layers 2 and 3 with a height of 200ft. Four of these fractures directly hit the four planar fractures of parent well at row 5 and row 6 in the y direction of the synthetic model. In case 2, the first five planar fractures of the infill well penetrate through layers 2 and 3 with a height of 200ft, and the last four planar fractures penetrate through layers 1 to 3 with a height of 300ft. All new fractures have no hits with pre-existing fractures. The case is designed to simulate the well interference effect through rock matrix (Awada et al., 2016). In case 3, the first five planar fractures are the same as those in Case 2. The last four stages of fractures are designed to have two planar fractures in each stage; one parallels with the pre-existing fractures and the other hits the pre-existing fractures with an angle. All new fractures penetrate through layers 1 to 3 with a height of 300ft. The upward growth of fractures in the Eagle Ford Shale formation toward the Austin Chalk formation is considered to be reasonable because the rock is more brittle in the Austin Chalk (Okeahialam et al., 2017).

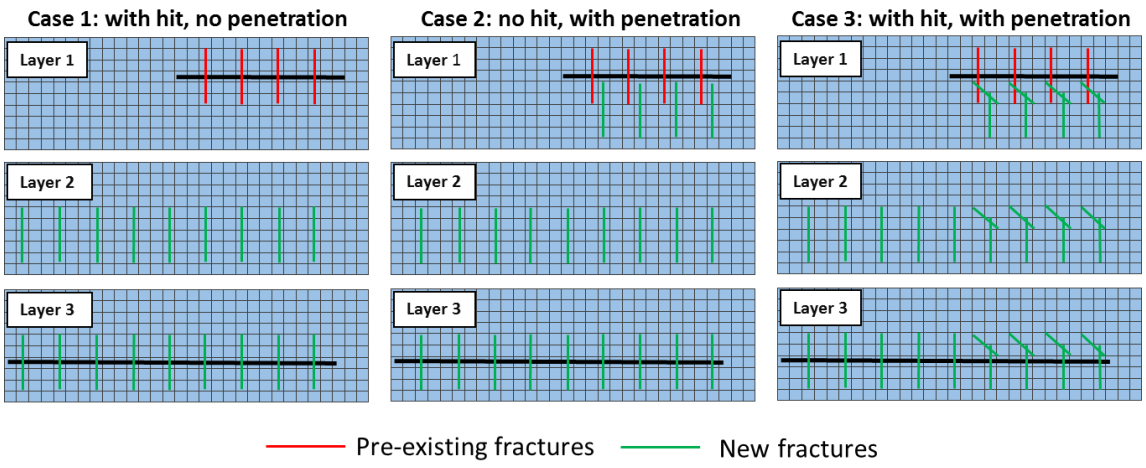

Figure 3.6–Three different well interference cases.

A 200-day production cycle is simulated for all three well interference cases. The infill well starts to produce when the parent well has already produced for 100 days. The wells are under the same well control strategies as in the base case. Figure 3.7(a) through (c) presents the oil-producing rates of parent and infill wells for the three cases. For case 1, the oil-producing rate of the parent well first increases sharply, and then it decreases below its original decline curve. It is a typical negative well interference performance resulted from the production competition with infill wells. The sharp rate increase is mainly because of the wellbore crossflow introduced by the fracture hits. For case 2, the producing rate of the parent well directly evolves underneath its original decline curve. The sharp rate increase cannot be observed in this case because there are no direct hits among fractures. For case 3, the producing rate of the parent well first increases above its original decline curve and then evolves underneath it. It is a combing result of the infill well's contribution to the SRV of the parent well and the infill well's competition with the

parent well. Figure 3.7(d) presents cumulative oil production of the parent well in all three cases and the case without infill wells. Case 1 and Case 2 have almost the same cumulative production, which is 8.2% lower than that of the case without infill wells at the end of 200 days. Case 3 has a little higher cumulative production compared to the other two cases, but it is still 5.7% lower than that of the case without infill wells at the end of the production. We can clearly tell from the comparison that all this three infill well scenarios bring negative well interference effects to the parent well in the Austin Chalk layer.

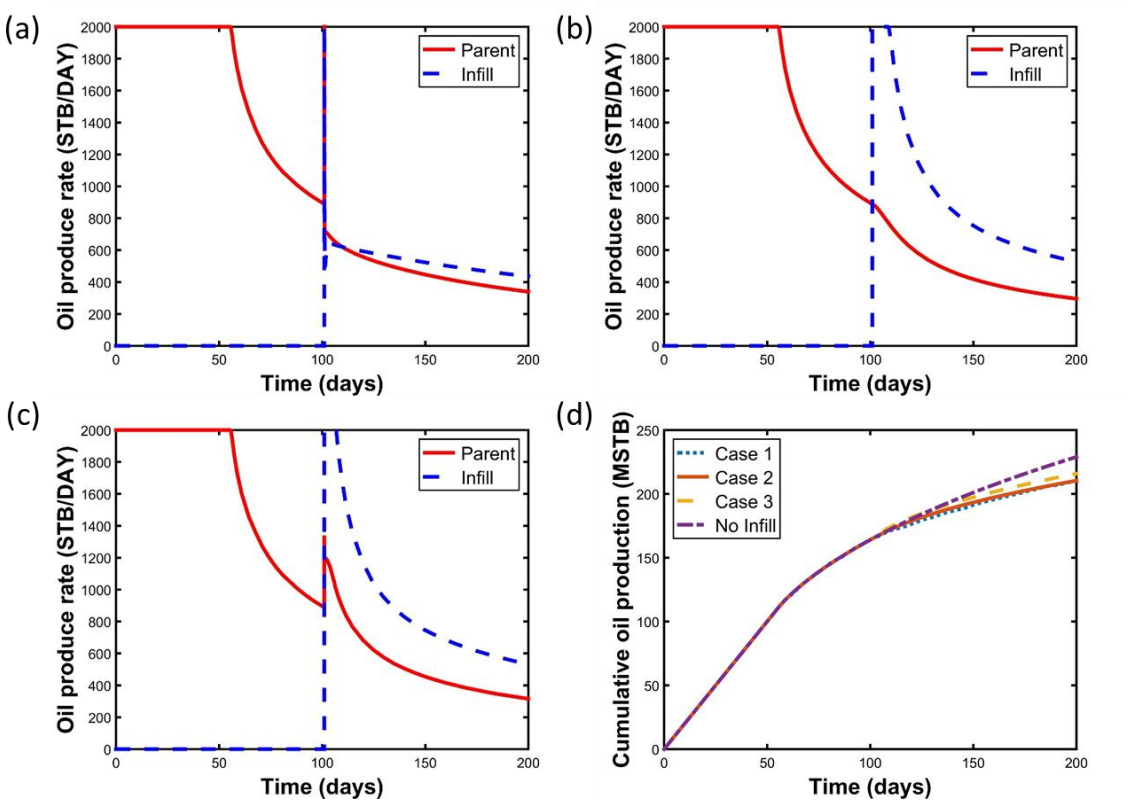

Figure 3.7–(a)-(c) Oil producing rate of parent and infill wells for cases 1 to 3. (d) Cumulative oil production of the parent well for cases1 to 3 and the case without infill wells.

Figure 3.8 shows the pressure maps at the 155th day of production for the case without infill wells and the three well interference cases. The pressure maps of layer one (the Austin Chalk layer) and layer three (the Eagle Ford Shale layer) are presented for each case. The presence of the infill well in the Eagle Ford Shale layer, and the well interference effects accelerate the pressure depletion in the Austin Chalk layer. The fracture hits in the Austin Chalk layer also accelerate the pressure depletion in the Eagle Ford Shale layer as shown in Figure 3.8(d).

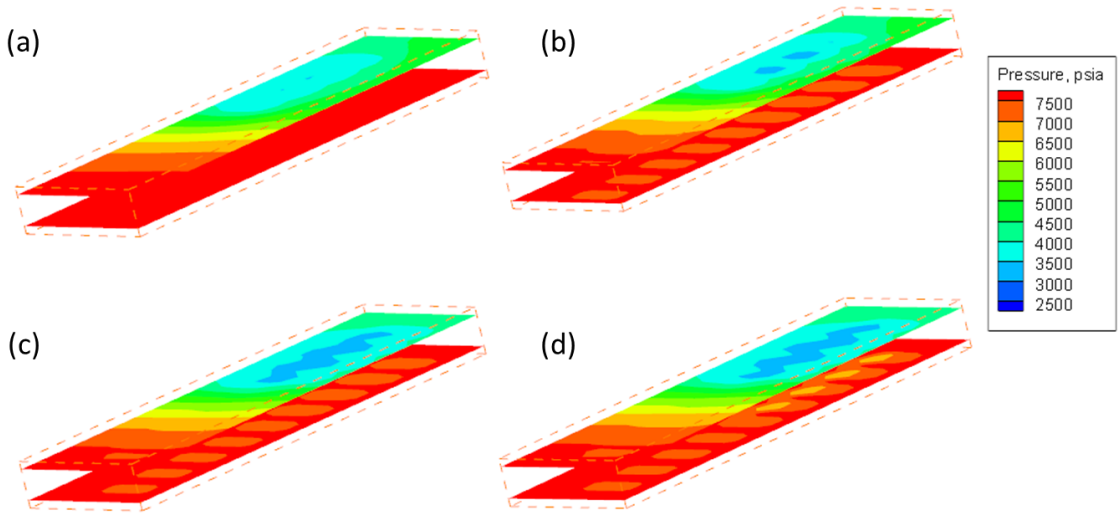

Figure 3.8–Pressure maps of the case without infill wells and cases 1 to 3 at the 155th day of the production.

3.3.2 Effect of Reservoir Permeability

We apply case 1 to evaluate the impacts of the Eagle Ford Shale permeability on the well interference between the parent and the infill wells. A 500-day production cycle is simulated, and the infill well is brought into production at the 200th day. Figure 3.9 shows the simulation results when the Eagle Ford Shale permeability equals to 450nd, 0.0045mD and 0.045mD. For the case of 450nd permeability, the well interference effect is similar as that shown in Figure 3.7(a). The production of the infill well reduces the cumulative production of the parent well for 11.2% at the end of 500-day production. For the case of 0.0045mD, the producing rate of the parent well first increases above its original decline curve after the infill well starts to produce, and then decline faster than it originally does. From the cumulative oil production comparison, we can confirm that it is a negative well interference scenario since the cumulative production of the parent well decreases 12.9% at the end of 500-day production. For the case of 0.045mD, the producing rate of the parent well increases to the maximum oil producing rate of 2000 STB/day after the infill well starts to produce. The parent well remains to produce at this rate for about 50 days, and then declines at a rate faster than its original decline rate because of the competition with the infill well. The cumulative oil production of the parent well at the 500th day is almost the same as that in the case without infill wells. Although we can expect a negative well interference effect after a longer production period, the positive well interference effect lasts for about 300 days in this case, which is comparable with the field observations shown in Figure 3.1.

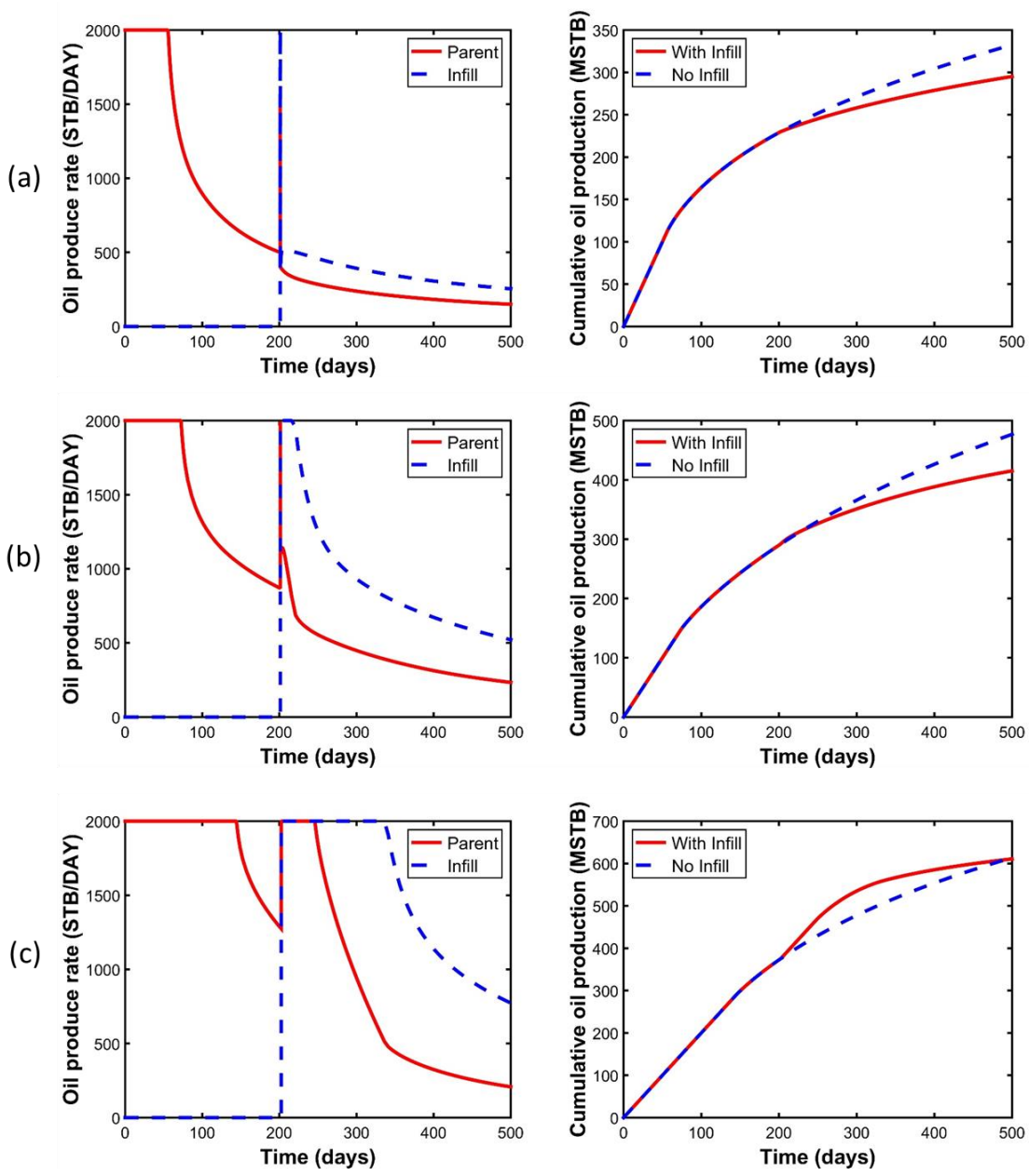

Figure 3.9–(a)-(c) Oil producing rate of the parent and the infill wells and cumulative oil production of the parent well for Eagle Ford Shale permeability equals to 450nd, 0.0045mD and 0.045mD.

Notice that the oil-producing rate of the parent well follows two decline rates after the infill well starts to produce in the cases of 0.0045mD and 0.045mD permeability. It is mainly because of the different performance of the infill well under different well controls. When the infill well starts to produce, it is first under the constraint oil producing rate control, with BHP declining quickly, which in turn accelerates the decline rate of the parent well. When the BHP of the infill well declines to 2000psi, the well control switches to the constant BHP control, and the producing rate of the infill well starts to decline. It also results in a slower decline rate of the oil-producing rate of the parent well.

Figure 3.10 shows the pressure maps at the 250th day of production for the cases with Eagle Ford Shale permeability equaling to 0.0045mD and 0.045mD. The high permeability of Eagle Ford Shale leads to a faster depletion rate and a higher recovery for the Austin Chalk formation. Therefore, if the infill well is completed in a high permeable region of the Eagle Ford Shale formation, the production of infill well can lead to positive well interference effect for the parent well in the Austin Chalk formation.

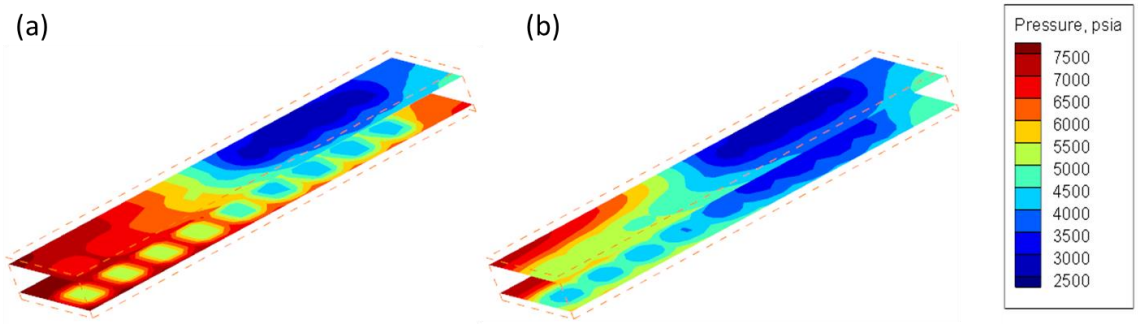

Figure 3.10–(a)-(b) Pressure maps at the 250th day of production for Eagle Ford Shale permeability equals to 0.0045mD and 0.045mD.

3.3.3 Effect of Nanopore Confinement

In this section, we evaluate the nanopore confinement effect of Eagle Ford Shale on the production performance of both the parent and the infill wells, and the well interference effects between them. We assume that the fractures and the Austin Chalk matrix have negligible capillary pressure, while the Eagle Ford Shale matrix has high capillary pressure as shown in Fig.5. We evaluate the nanopore confinement effect by considering capillary pressure in the phase behavior of reservoir fluid in Eagle Ford Shale. The evaluation is based on case 3, where the new fractures of infill well penetrate to the upper Austin Chalk formations and hit the existing fractures of the parent well. Figure 3.11(a) shows the cumulative oil production of the parent and the infill wells with and without capillary pressure effects being considered in VLE calculation. The two scenarios give exactly the same cumulative oil production curves. It is because the extremely low permeability of the Eagle Ford Shale layer, in this case the 450nd, and thus most of the rock matrix grids with no hydraulic fractures embedded do not contribute to the production. We then increase the permeability to 0.045mD, which considers the existence of nature fractures. Figure 3.11(b) presents the cumulative oil production of the parent and the infill wells for this case. The results indicate that the cumulative oil production of the infill well increases 4.4% at the end of 500-day production when considering capillary pressure effect in VLE calculation. The observation is comparable to those reported by other researchers who studied the nanopore confinement effect on reservoir performance (Siripatrachai et al., 2017; Yuan Zhang et al., 2017). At the same time, the cumulative oil production of the parent well decreases 3.6%. Figure 3.12(a) and (b) show the oil-

producing rates of the parent and the infill wells with and without capillary pressure in VLE calculation. We can observe an increase of the oil-producing rate in the infill well and a drop of the oil-producing rate in the parent well in the late production period. The results indicate that the consideration of nanopore confinement effect makes the infill well a stronger competitor in the production system. It is mainly because that the additional capillary pressure in VLE calculation leads to a lower bubble point pressure of fluid mixture. In other words, the fluid properties in Eagle Ford Shale are no longer the same as those in Austin Chalk because of the capillary pressure in phase behavior. This situation favors the oil production of infill well in the Eagle Ford formation, and also leads to more negative well interference effects to the parent well in the Austin Chalk formation.

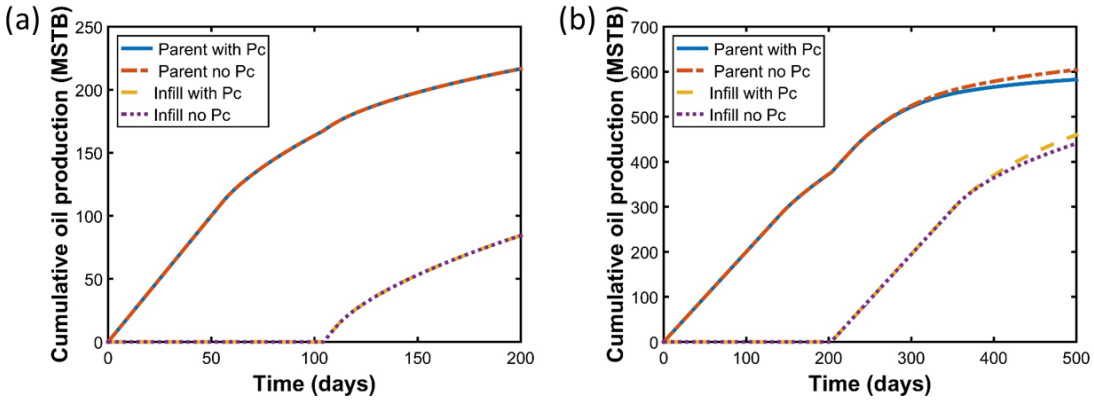

Figure 3.11–(a)-(b) Cumulative oil production of the infill and the parent wells with and without capillary pressure effects being considered in VLE calculation for Eagle Ford layers permeability equals to 450nd and 0.045mD.

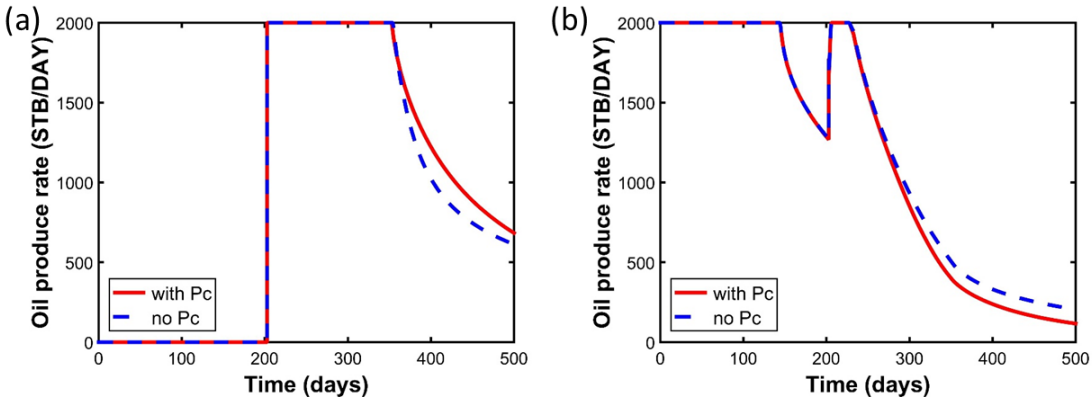

Figure 3.12–(a)-(b) Oil producing rate of the infill and the parent wells with and without capillary pressure effects being considered for permeability equals to 0.045mD.

3.3.4 Effect of Natural Fractures

Austin Chalk is characterized by its natural fracture system. We analyze the effect of natural fractures by randomly generating 20 natural fractures in the Austin Chalk layer as shown in Figure 3.13. The properties of these fractures are shown in Table 3.3.

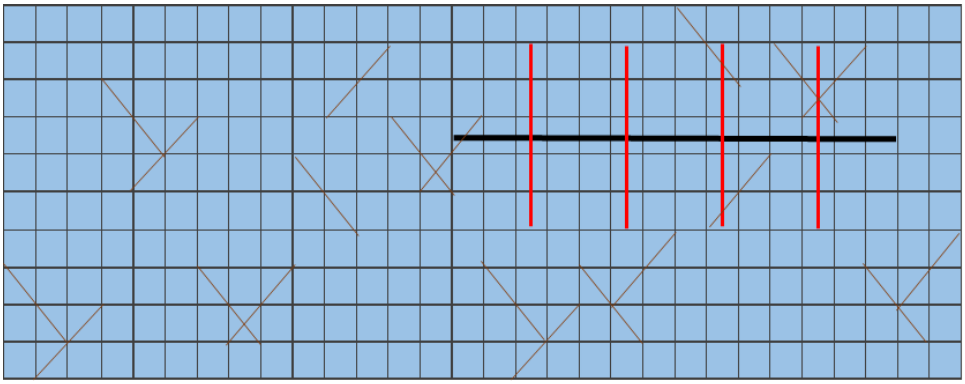

Figure 3.13–Layout of the Austin Chalk layer with natural fractures embedded.

Fracture width (ft)	Fracture length (ft)	Fracture permeability (mD)	Fracture porosity
0.02	282.84	3000	1

Table 3.3–Properties of natural fractures in the Austin Chalk layer.

We apply the production scenarios in case 1 and case 2 for analysis. The cumulative production curves of the parent well with and without natural fractures for these two cases are shown in Figure 3.14(a). At the 200th day of production, the existence of natural fractures increases the cumulative production of parent well by 3% and 4% for case 1 and case 2 respectively. Figure 3.14(b) presents the cumulative production curves of the infill well. At the 200th day of production, the cumulative production of case 1 increases by 1%, and that of case 2 increases by 9%. This is mainly because that the fractures of infill well penetrate to the Austin layer in case 2. Figure 3.15(a) and (b) depict the pressure maps at the 150th day of production for case 1 and case 2 with natural fractures. Comparing the figures with Figure 3.8(b) and (c), we can find the pressure depletion becomes faster when natural fractures exist. However, the oil producing rate profiles are similar to that presented in Figure 3.7(a) and (b), which indicates that the production of the infill well still brings negative well interference effects to the parent well in these two cases.

3.3.5 Effect of Hydraulic Fracturing Process

The above simulation results are all based on the assumption that the infill drilling and completion process do not significantly change the reservoir properties. In the actual hydraulic fracturing process, large volume of fracturing fluid is injected into the formation to create fractures and then a fracturing fluid flow back period will be followed before the well starts to produce hydrocarbons. This process may change the reservoir pressure and water saturation especially at the fractured zones. To account for the effect of hydraulic fracturing, we set the water saturation and the pressure of the new-fracture-embedded reservoir cells to be 0.5 and 10000psi before the infill well starts to produce. The exact value changes need to be tracked by a coupled geomechanics-reservoir model, which is beyond the scope of this paper. Figure 3.14(a) through (c) present the parent well oil producing rate of the three cases with and without the hydraulic fracturing effect being considered. Figure 3.14(d) shows the parent well cumulative oil production of the three cases under the hydraulic fracturing effect and the case without infill wells. For case 1, where new fractures stay in the Eagle Ford formation, the oil-producing rate of the parent well does not change. For case 2, where new fractures penetrate to the Austin Chalk formation, the oil-producing rate of the parent well increases compared to the original case. This increasing trend lasts for about 75 days, and then the oil-producing rate goes back to its original track. The infill well in this case still brings a negative effect to the parent well at the end of 200-day production with a 4.9% decline in cumulative oil production. For case 3, the additional pressure brought by the infill well has a significant effect in increasing the production of the parent well since the new fractures not only

penetrate to the Austin Chalk but also hits the existing fractures. Similar to case 2, the parent well oil-producing rate drops back to its original declining track 75 days after the infill well starts to produce. In this case, the cumulative oil production of parent well is the same as that of the no infill case at the end of 200-day production. Therefore, the positive well interference effect lasts for about 100 day in this case, and we can expect a negative well interference effect afterwards.

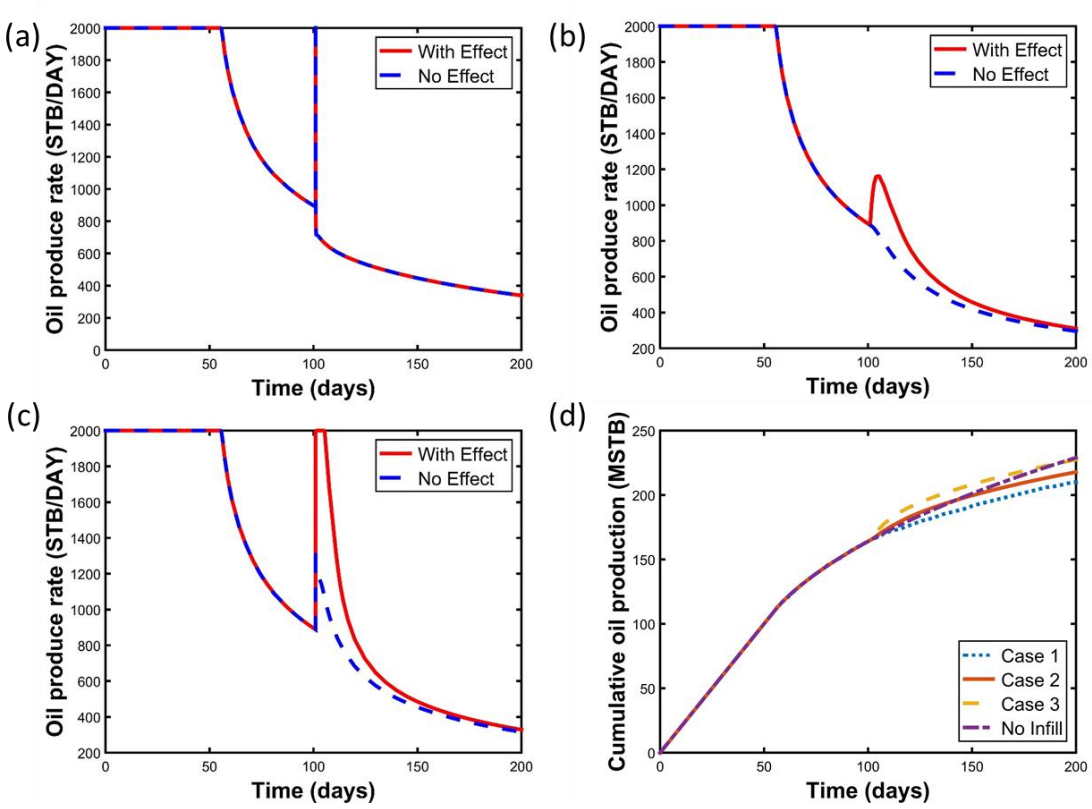

Figure 3.14–(a)-(c) Oil producing rate of the parent and infill wells for cases 1 to 3 with and without hydraulic fracturing effect. (d) Cumulative oil production of the parent well for cases 1 to 3 with hydraulic fracturing effect and the case without infill wells.

Figure 3.15 shows the pressure maps at the 101th day of production for case 2 and case 3. In both cases, the new fractures of infill wells penetrate to the Austin Chalk layer. The hydraulic fracturing process can increase the pressure of nearby formation, providing an additional pressure support for the existing producer. This additional pressure support can lead to a period of positive well interference effect for the parent well in Austin Chalk.

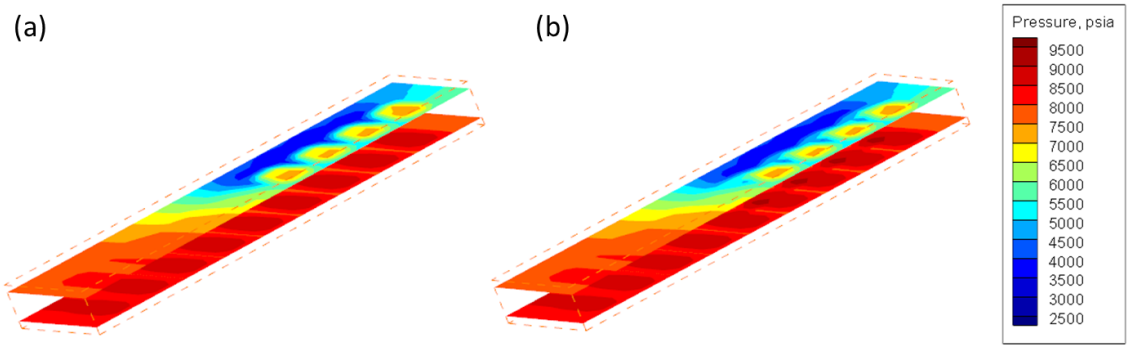

Figure 3.15–(a)-(b) Pressure maps at the 101st day of production for case 2 and case 3 with the additional pressure support from the hydraulic fracturing process.

3.4 Infill Well Pad and Well Group Control

A new homogeneous 3D reservoir case is set up in Figure 3.16. The reservoir dimension is 1000ft×800ft×400ft, discretizing into 20×16×4 grid blocks. A parent well (Parent) is completed in the top layer of the reservoir with three transverse fractures. Two infill child wells (Well1 and Well2) are completed in the bottom layer of the reservoir, each having four transverse fractures. There exists one transverse fracture fully penetrating

the whole reservoir thickness, connecting the Parent Well and Well 2. All other transvers fractures only penetrate a single reservoir layer. Reservoir and fracture properties are shown in Table 3.4. All three wells are treated as multi-segment wells with the topmost segment located at the tubing head. We assume that all three wells are grouped into a same surface manifold or stock tank with a minimum tubing head pressure (THP) constraint of 100 psi applied. In this case, the parent well produces with two transverse fractures in the top layer and one transverse fracture in the whole reservoir thickness from the beginning. Two infill child wells are brought into production at the same time with Well 2 sharing a same transverse fracture with the Parent Well.

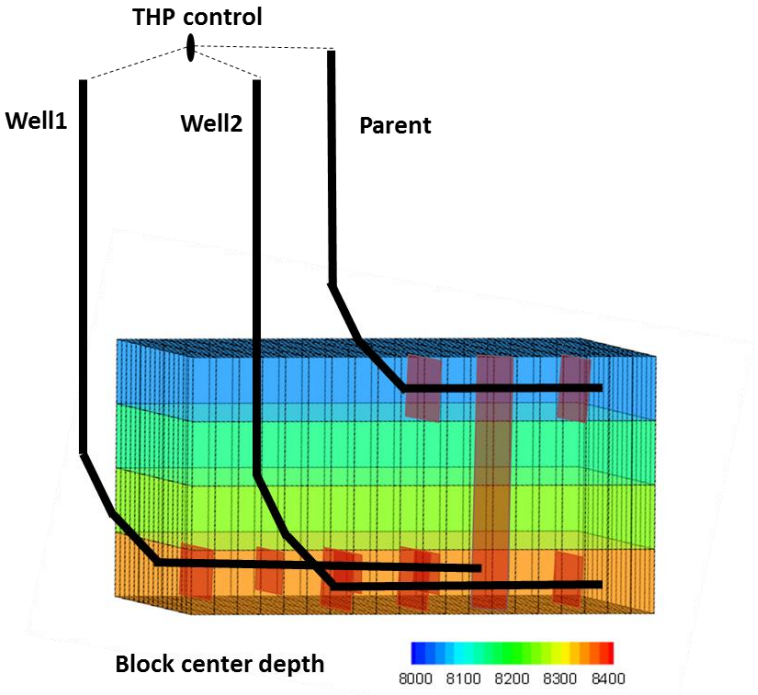

Figure 3.16–Reservoir and wellbore layout for the case with well group control

Parameter	Value	Units
Initial reservoir pressure	8000	psi
Initial water saturation	0.3	-
Reservoir temperature	200	F
Rock matrix porosity	0.06	-
Rock matrix permeability	450	nD
Rock compressibility	4×10^{-6}	psi^{-1}
Fracture width	0.02	ft
Transverse fracture porosity	0.3	-
Transverse fracture permeability	5000	mD
Connecting fracture porosity	0.1	-
Connecting fracture permeability	1000	mD
Gas fluid composition	10.0 CO_2 90.0 CH_4	mol%

Table 3.4–Simulation parameters of the case with well group control

Figure 3.17(a) indicates a peak of the parent well's producing rate at the time infill child wells being brought into production. Shortly after that, the parent well's producing rate decreases to a value below that before the child wells start to produce. Figure 3.17(b) shows that the cumulative production of the parent well decreases for about 22% at the end of the simulation. The production peak for the parent well is the result of wellbore cross flow of Well 2. The extremely low permeability of shale reservoir makes the pressure of fractured area of the parent well significantly lower than the pressure of un-fractured area. When Well 2 is brought into production, its third perforation which shares the same transverse fracture with the parent well experiences severe crossflow.

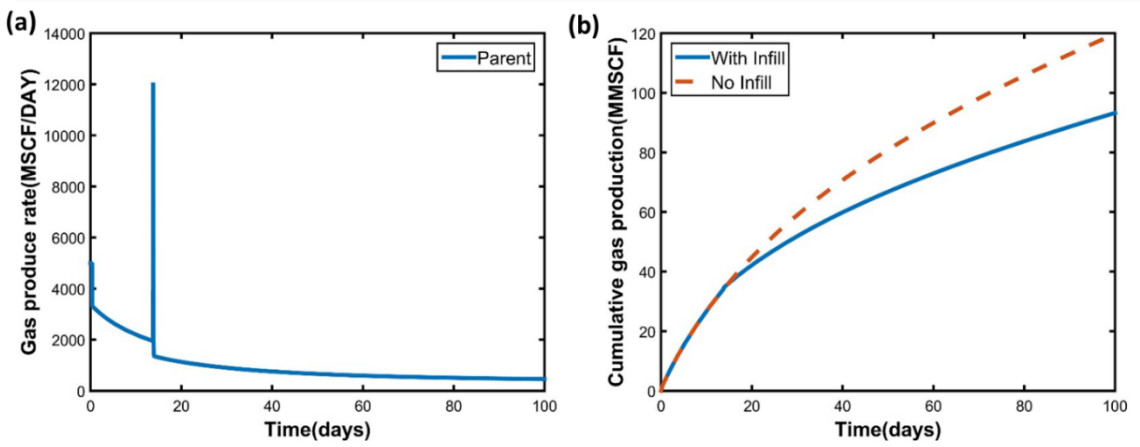

Figure 3.17–(a) Gas production rate and (b) cumulative gas production for the parent well with and without the infill well pad.

Figure 3.18(a) presents the gas inflow rate of this perforation for a short period of time after Well 2 starts to produce. We can observe that the crossflow period only lasts for a short period of time as wellbore pressure quickly drops below the pressure of fractured area. The average productivity index of two infill wells presented in Figure 3.19(b) indicates that the productivity of Well2 is at first lower than Well1 because of the wellbore cross flow. When the crossflow ceases, the productivity of Well2 ends up being slightly larger than Well1 due to a larger SRV. In this case, infill Well2 acts as a “contributor” to the parent well because of the unbalanced pressure at the beginning of production, but it ends up being a “competitor” because of the SRV overlap with the parent well.

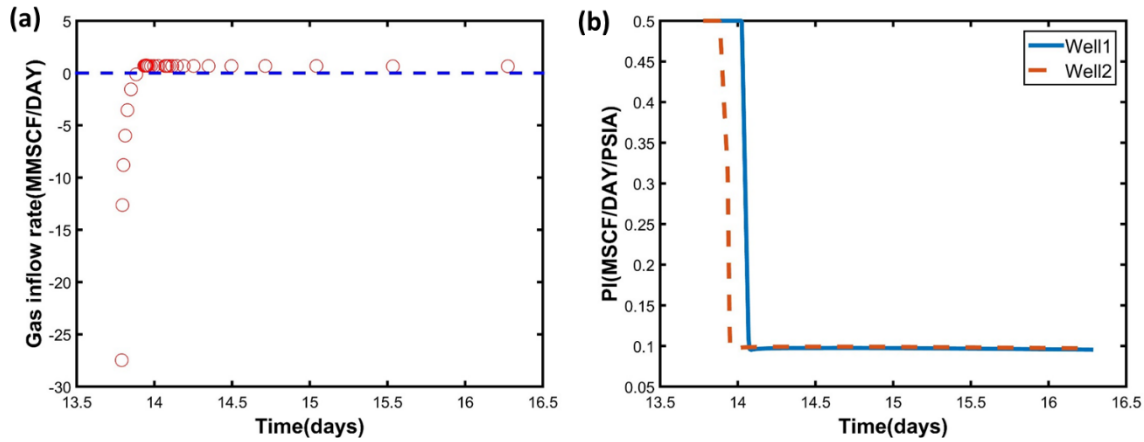

Figure 3.18–(a) Gas inflow rate of the third perforation of Well 2 shortly after it starts to produce and (b) average productivity index of Well1 and 2 for the same evaluating period.

Furthermore, we introduce a connecting fracture between infill Well 1 and Well 2 based on the above 3D case. Figure 3.19 compares the reservoir pressure map with and without a connecting fracture between two infill wells. We can observe that parent well depletes quicker at the second perforation when there is a connecting fracture between infill wells. The fracture hit between parent well and infill Well 2 also occurs at this second perforation.

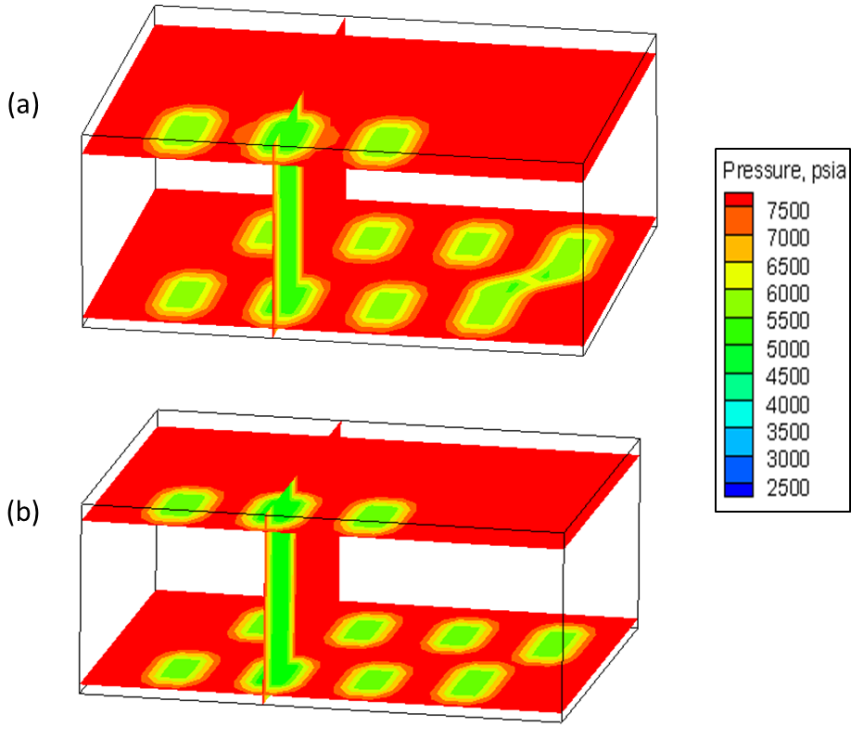

Figure 3.19–Reservoir pressure map at the 60th day of simulation (a) with and (b) without connecting fracture between infill wells.

Figure 3.20 presents the cumulative production of the parent well and infill well pair (Well1+Well2) for the 3D case with and without connecting fracture between the infill wells. We can observe that the infill well pair becomes a stronger competitor when there is a hydraulic connection between them. The cumulative production rate of the parent well decreases for about 2% compared to the no connection case. The cumulative production rate of infill well pair increases for about 5% compared to the no connection case. This also indicates that a considerable percentage of the infill well pair cumulative production rate increase comes from the increasing SRV introduced by the connecting fracture between Well1 and Well2.

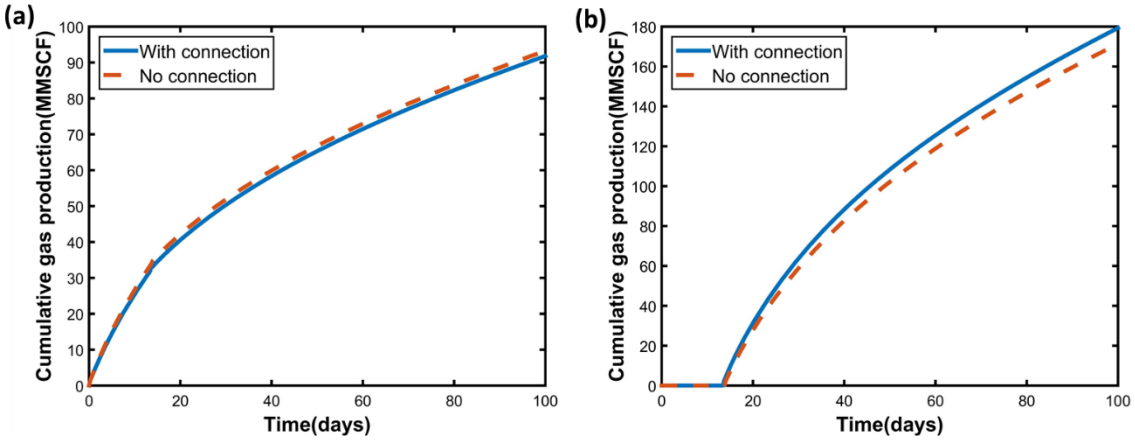

Figure 3.20–Cumulative gas production of (a) the parent well and (b) the infill well pair (Well1 and Well2) with time for the 3D case with and without connection between Well1 and Well2.

3.5 Discussion

Among all the cases being studied, only two of them show positive well interference effect. In one case, the Eagle Ford Shale permeability is four times smaller than that of the Austin Chalk. In the other case, the new hydraulic fractures penetrate to the Austin Chalk formation and hit the existing fractures with an additional pressure support resulting from the hydraulic fracturing process. The positive well interference period lasts for about 300 days for the first case and about 100 days for the second case. In the field observations presented by Figure 3.1, the positive well interference period lasts for about 200 days, but a longer time can be expected based on the rate profile. To history match these field data, a combined effect of high permeable Eagle Ford Shale region and hydraulic fracturing process can be considered.

The simulation results indicate that the negative well interference effect is much more common for a parent well completed in the Austin Chalk formation and an infill well completed in the Eagle Ford Shale formation. This conclusion makes physical sense and coincides with field observations. However, it is not a trivial conclusion from the perspective of reservoir simulation. Based on our previous simulation results for 2D and 3D homogeneous reservoirs, positive well interference results are much more commonly obtained (Tang et al., 2017). If parent wells and infill wells are modeled in a reservoir with universal permeability, a positive well interference result is inevitable because new fractures introduced by the infill well contribute to the SRV of the parent well. To history match the field data with negative well interference effects, a reservoir engineer can consider setting the formation permeability around the parent wells to a significant higher value (more than 5 times) than the surrounding formations. It is a reasonable setting when we consider the complex fracture network around the wells.

3.6 Conclusions

In this chapter, we investigated the well interference phenomenon in two different formations with GURU-MSW. We considered the nanopore confinement effect in phase behavior and applied an embedded discrete fracture model (EDFM) to simulate the new fractures introduced by infill wells. The multi-segment wellbore model can characterize the wellbore crossflow introduced by fracture hits. The model was validated against ECLIPSE 300 with an excellent agreement.

We specifically focused on studying the effect of an infill well in the Eagle Ford Shale formation on the production performance of a parent well in the Austin Chalk formation. Different reservoir properties and hydraulic fracturing impacts were evaluated through the reservoir model. The following conclusions are obtained from the simulation results:

(1) The multi-segment well model allows the program to characterize the wellbore crossflow introduced by fracture hits. The simulation results also prove that the sharp producing rate increase of parent wells can be an indicator of direct fracture hits between parent and infill wells.

(2) Infill wells in Eagle Ford Shale most likely result in negative impacts on existing producers in Austin Chalk. From the perspective of reservoir simulation, the main parameter that contributes to the phenomenon is the reservoir permeability difference between the two formations.

(3) A smaller permeability difference between the two formations and the additional pressure support due to hydraulic fracturing can lead to positive well interference effects for the parent well after the infill well starts to produce. This positive well interference period can last for several hundred days.

(4) The nanopore confinement effect can lead to more negative well interference impacts on the parent well in Austin Chalk if the permeability of the Eagle Ford Shale region is sufficiently large.

4. LIQUID LOADING STUDY OF HORIZONTAL GAS WELL*

Liquid loading is a challenging production issue in most mature gas fields. The dynamic interaction between wellbore and reservoir when liquid loading happens cannot be comprehensively simulated by a single wellbore simulator or a single reservoir simulator. Therefore, applying a fully coupled wellbore-reservoir simulator like GURU-MSW to analyze liquid loading phenomena is almost idealized. In this chapter, we will introduce a new drift-flux model for liquid loading characterization. By combing this new drift-flux model within GURU-MSW, we are able to model some interesting phenomena that have never been systematically studied in the literature.

---

*Part of this section is reprinted with permission from "Development and Application of a Fully Implicitly Coupled Wellbore-Reservoir Simulator to Characterize the Flow Transients in Liquid-Loaded Horizontal Gas Wells" by H. Tang, A.R. Hasan, and J. Killough. SPE Journal, Copyright [2018] by Society of Petroleum Engineers, and "What Happens After the Onset of Liquid Loading? --- An Insight from Coupled Well-Reservoir Simulation" by H. Tang, Z. Chai, Y. He et al. SPE Proceedings, Copyright [2018] by Society of Petroleum Engineers.

4.1 Introduction

The liquid loading phenomenon occurs when the gas rate is not high enough to carry all the liquids (water or condensate) to the surface. The unproduced liquids can accumulate in the wellbore, resulting in sharp drops in gas producing rates, sharp changes in wellbore pressure and liquid slug production (Lea and Nickens, 2004).

There are a few research efforts in predicting the onset of liquid loading in horizontal wellbores. El Fadili and Shah (2017) clarified that the conventional model for critical gas rate prediction in vertical wells cannot be applied to horizontal wells. They proposed a new model for horizontal and deviated wells and tested the model with data from 62 wells. Shi et al. (2016) presented an analytical model based on the size and shape of liquid droplet to predict critical gas rates for liquid loading in vertical, slanted and horizontal wellbores. Wang et al. (2018) pointed out that the liquid droplet model cannot explained the liquid-loading mechanism revealed by the experimental work well (Alamu, 2012; Magrini et al., 2012). They proposed an analytical model based on the force balance of the bottom film and an empirical model that was tested by data from 60 horizontal wells from north China. Ansari et al. (2018) collected data from the Marcellus Shale reservoir to build a neural network model for real-time liquid loading prediction.

However, predicting the critical gas rate is only the first step in understanding the liquid loading phenomenon. The difficulties in fully modeling the phenomenon come from the dynamic interaction between the multiphase flow in wellbore and reservoir. Especially for unconventional reservoirs that apply stimulation techniques, a comprehensive

modeling approach should account for both heterogeneity in reservoir and hydrodynamics in wellbore.

Jackson et al. (2011) investigated liquid loading in an open-hole tight gas horizontal well with a commercial transient multiphase flow simulator coupled with an inflow-performance-relationship (IPR) curve to describe the reservoir. They assumed the pressure near the wellbore followed a linear relationship between the manually assigned pressure limits. Tan et al. (2017) introduced a design method for de-liquification with coiled tubing in shale gas reservoirs based on nodal analysis. Their method combines the IPR curve of multi-stage hydraulic fractures in shale reservoir and the tubing performance curve calculated from the Beggs & Brill model (Beggs and Brill, 1973). Both models mentioned above chose to simplify the reservoir system using IPR curves, which ignores transient behaviors such as wellbore fluid reinjection into the reservoir. Therefore, Limpasurat et al. (2015) proposed to apply a reservoir simulation method with special treatment of sink/source terms to characterize the liquid phase reinjection into the reservoir. Their wellbore model adopted the empirical treatment proposed by Dousi et al. (2006) which assumed no liquid production after gas rates drop below the critical gas rates. However, this assumption contradicts the field observations of Marino et al. (2017) which stated that coproduction of liquid and gas after the onset of liquid loading is feasible.

It appears that no-one in the literature has attempted to simulate the liquid loading phenomenon through a fully implicitly coupled wellbore-reservoir simulator (either a commercial one or a self-developed one). Therefore, we intend to apply GURU-MSW to characterize the flow transients in liquid-loaded gas wells.

4.2 Drift-Flux Model for Liquid Loading Characterization

We would like to repeat here the basic gas-liquid drift-flux model proposed by Zuber and Findlay (1965):

$$v_g = C_0 v_m + v_d \tag{4.1}$$

There are two parameters that correlate the mixture velocity (vm) with gas in situ velocity (vg) in the model, one is the distribution parameter (Co) and the other is drift velocity (vd). The distribution parameter accounts for the non-uniform distribution of gas phase over the pipe cross section. The drift velocity describes the relative velocity of the gas phase comparing to the two-phase mixture velocity Wallis (1969).

Although there are a lot of high-performance drift-flux models in the literature, few of them can be applied in a fully implicitly coupled wellbore-reservoir system as stated in Section 2.2.2. The drift-flux model originally developed by Holmes in 1977 (covered in more details by Shi et al. 2005) fulfills the aforementioned requirements and has been applied in several fully coupled wellbore-reservoir simulators (Livescu et al., 2010; Pan and Oldenburg, 2014; Schlumberger, 2017a). Equations (4.2) to (4.6) present the drift-flux model introduced by Shi et al. (2005).

$$C_o = \frac{A}{1+\left(A-1\right)\gamma^2} \tag{4.2}$$

$$\gamma = \frac{\max\left(\alpha_g, F_v \frac{\alpha_g V_m}{V_{sgf}}\right) - B}{1-B} \tag{4.3}$$

$$v_d = \frac{\left(1-\alpha_g C_o\right) C_o K\left(\alpha_g\right) V_c}{\alpha_g C_o \sqrt{\frac{\rho_g}{\rho_l}} + 1 - \alpha_g C_o} \tag{4.4}$$

$$K\left(\alpha_g\right) = \begin{cases} 1.53/C_o & \text{for } \alpha_g \le a_1 \\ 1.53/C_0 + \dfrac{Ku - 1.53/C_0}{2}\left[1-\cos(\pi \dfrac{\alpha_g - a_1}{a_2 - a_1})\right] & \text{for } a_1 < \alpha_g < a_2 \\ Ku & \text{for } \alpha_g \ge a_2 \end{cases} \tag{4.5}$$

In Equation (4.3), gas flooding velocity (V_{sgf}) is defined as:

$$V_{sgf} = K_u \left(\frac{\rho_l}{\rho_g}\right)^{0.5} V_c \ . \tag{4.6}$$

In Equation (4.5) and (4.6), *Ku* is the Kutazeladze number. We applied a formulation reported by Pan (2011) as shown in Eq. (19). The ramping parameters, a_1 and a_2, are set to 0.06 and 0.21.

$$Ku = \left[\frac{C_{ku}}{\sqrt{N_B}}\left(\sqrt{1+\frac{N_B}{C_{ku}^2 C_w}} - 1\right)\right]^{0.5} \tag{4.7}$$

In Equation (4.7), N_B is the Bond number, which is calculated as the square of the dimensionless pipe diameter. To match the measurement given by Richter (1981), C_w is set to 0.008 and C_{ku} is set to 142. The characteristic velocity (V_c) is defined as:

$$V_c = \left(\frac{\sigma_{gl} g\left(\rho_l - \rho_g\right)}{\rho_l^2}\right)^{0.25} \tag{4.8}$$

The model is independent of flow patterns and only requires the pre-knowledge of mixture velocity (v_m), gas void fraction (α_g), and other fluid properties that can be calculated from primary variables. The original model parameters were determined through experiments of gas void fractions from 0 to 0.6 and pipe inclinations from 0° to 88°, which indicates that the model may not have good performance in annular or mist flow regime (Pan et al., 2011; Pan and Oldenburg, 2014). In order to characterize the liquid loading phenomenon, we incorporate into the model several criteria to predict the transition from annular or stratified flow regimes to churn or slug flow regimes. The parameters for the modified model are determined with the same optimization algorithm as introduced by Shi et al. (2005). We apply a larger range of experimental data with gas void fractions from 0 to 1 and modify the model for horizontal pipe.

For vertical and nearly vertical pipe (inclinations from 0° to 45°), the transition from churn to annular flow is based on two criteria (Hasan et al., 2010): the first is that v_{sg} exceeds a critical velocity value (v_{gc}), and the second is that gas void fraction should be larger than 0.7. We apply a critical velocity criterion introduced by Taitel et al. (1980) as shown in Equation (4.9). The criterion was determined from the balance between the gravity and drag forces acting on a liquid droplet.

$$v_{gc} = 3.1\left[\frac{g\sigma\left(\rho_l - \rho_g\right)}{\rho_g^2}\right]^{1/4} \tag{4.9}$$

An empirical value m is incorporated into the expression of v_d as follows to make the drift velocity sensitive to the flow regime transition.

$$v_{dm} = v_d \times m \times f(\theta) \tag{4.10}$$

$$m = \begin{cases} m_1 & \text{for } v_m \geq v_{gc} \\ m_2 & \text{for } v_m < v_{gc} - b \\ m_1 + (m_2 - m_1)/2 \times \left(1 + \cos(\pi(V_m - V_{gc} + b)/b)\right) & \text{for } v_{gc} - b \leq v_m < v_{gc} \end{cases} \tag{4.11}$$

In Equation (4.10), v_{dm} represents the modified v_d. Notice that v_m instead of v_{sg} is applied in the equations. Equation (4.11) is made continuous and differentiable to fulfill the strict requirements mentioned above. This assumes that in a high gas void fraction region where annular flow occurs, v_m is approximately equal to $v_{sg.}$ The impact of pipe inclination is accounted through $f(\theta)$, which follows the same expression as in the original model as shown in Equation (4.12):

$$f(\theta) = \left(\cos(\theta)\right)^{n_1} \times \left(1 + \sin(\theta)\right)^{n_2} \tag{4.12}$$

Low liquid holdup data reported by Guner et al. (2015) and high liquid holdup data reported by Shi et al. (2005) are combined to determine the optimized parameters for nearly vertical pipe. The final parameters that achieves the predicting results shown in Figure 4.1 are [A, B, m_1, m_2, b, n_1, n_2] = [1.27, 0.5, 1.29, 0.99, 0.1, 0.9, 1.2]. Most of the data in Figure 4.1 fall within the ±20% error range. The squared 2-norm of the difference between measured and predicted values of liquid holdup is 0.179.

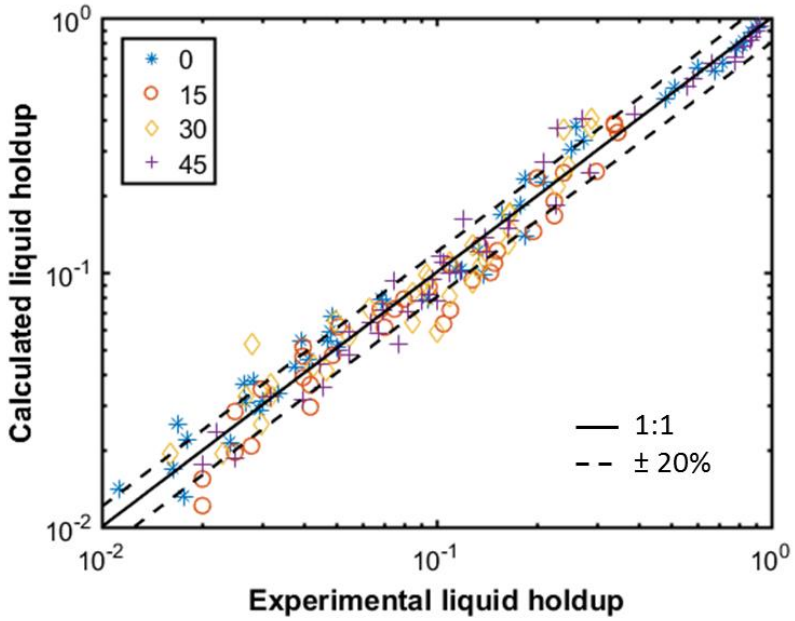

Figure 4.1–Comparison of calculated liquid holdup and experimental liquid holdup for nearly vertical pipes (experimental data adapted after Shi et al. 2005; Guner et al. 2015).

For nearly horizontal pipe (inclinations from 45° to 88°), the same modifications as shown in Equations (4.9) to (4.11) are applied. The only difference is that a new correction function for pipe inclination f(θ) is applied. The new function shown in Equation (4.13) is adapted from the angle-corrected Turner criterion proposed by Belfroid et al. (2008).

$$f(\theta) = n_1 \times \left(\sin\left(1.7\theta\right)\right)^{n_2} \tag{4.13}$$

Low liquid holdup data reported by Alsaadi et al. (2015) and high liquid holdup data reported by Shi et al. (2005) are applied for parameter optimization. Experimental data for 45° inclination pipe from Figure 4.1 is also included in order to cover the whole inclination

range of nearly horizontal pipe. Figure 4.2 shows the comparison result of predicted and measured values of liquid holdup, and the calculated squared 2-norm difference between them is 0.157. The final optimized parameters are [A, B, m_1, m_2, b, n_1, n_2] = [1.27, 0.5, 1.71, 1.18, 0.96, 1.17, 0.42].

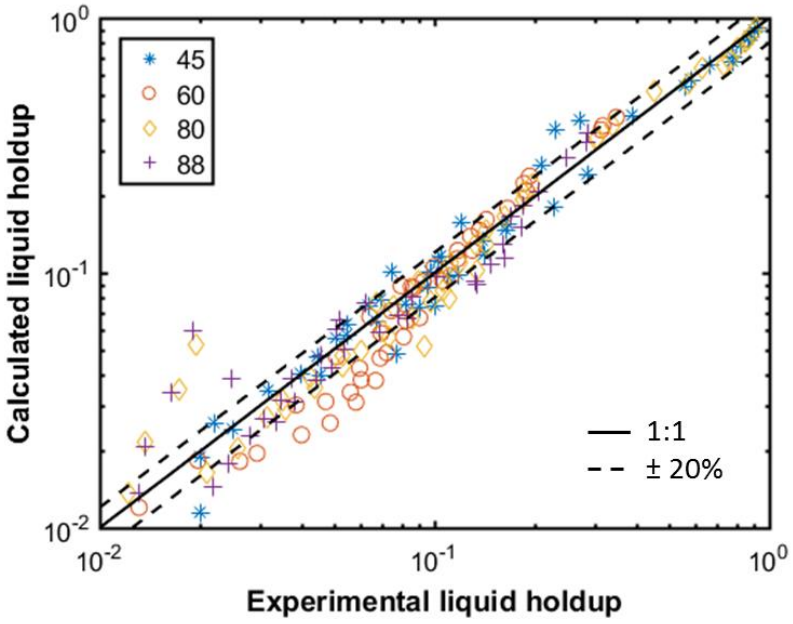

Figure 4.2–Comparison of calculated liquid holdup with experimental liquid holdup for nearly horizontal pipes (experimental data adapted after Shi et al. 2005; Alsaadi et al. 2015; Guner et al. 2015).

The flow patterns in horizontal pipes are substantially different from those observed in vertical and inclined pipes Oddie et al. (2003). In the original expression of drift velocity (Equation (4.4)), $K(\alpha_g)V_c$ acts as a transition curve between bubble rise velocity $1.53V_c$ and flooding velocity K_uV_c (Holmes, 1977) based on the gas volume

fraction ramping parameters a_1 and a_2. Both velocities were obtained from vertical flow experiments and no longer applicable to horizontal flow. A relative velocity (V_r) obtained from the original flooding curve expression described by Wallis (1969) is applied as a substitute for $K(\alpha_g)V_c$ in the modified drift velocity expression. Equations. (4.14) to (4.16) present the modified model for horizontal flow:

$$C_o = \frac{A}{1+(A-1)\alpha_g^{\,2}} \tag{4.14}$$

$$V_d = \frac{(1-\alpha_g C_o)C_o V_r m}{\alpha_g C_o\sqrt{\frac{\rho_g}{\rho_l}}+1-\alpha_g C_o} \tag{4.15}$$

$$V_r = \sqrt{\frac{gD(\rho_l-\rho_g)}{\rho_l}} \tag{4.16}$$

Brito (2015) applied a liquid wave-growth criterion proposed by Taitel and Dukler (1976) to predict the transition from stratified flow to stratified wavy with liquid film reversal flow. The criterion, which is expressed in dimensionless liquid height cannot be applied directly in the drift-flux model framework. A simplified criterion of gas void fraction is applied in the modified model, which is $A = A_1$, $m = m_1$ for $\alpha_g < a_1$, and $A = A_2$, $m=m_2$, for $\alpha_g > a_2$, and a linear interpolation between these values when $a_1<\alpha_g< a_2$. Experimental data of horizontal pipe flow (θ = 90°) reported by Fan (2005) (mainly in stratified wavy flow regime) and Brito (2012) (mainly in slug flow regime) are applied to obtain the model parameters. Figure 4.3 shows the comparison result of predicted and measured values of liquid holdup, which has a squared 2-norm difference of 0.114. The

final optimized parameters are [A_1, A_2, m_1, m_2, a_1, a_2] = [0.72, 1.86, 4.51, 0.21, 0.54, 0.89]. The relevant liquid holdup values for flow pattern transition are 0.46 (1- a_1) and 0.11 (1- a_2) based on the optimized values of a_1 and a_2. We would like to point out that the proposed horizontal model is highly empirical and data-oriented.

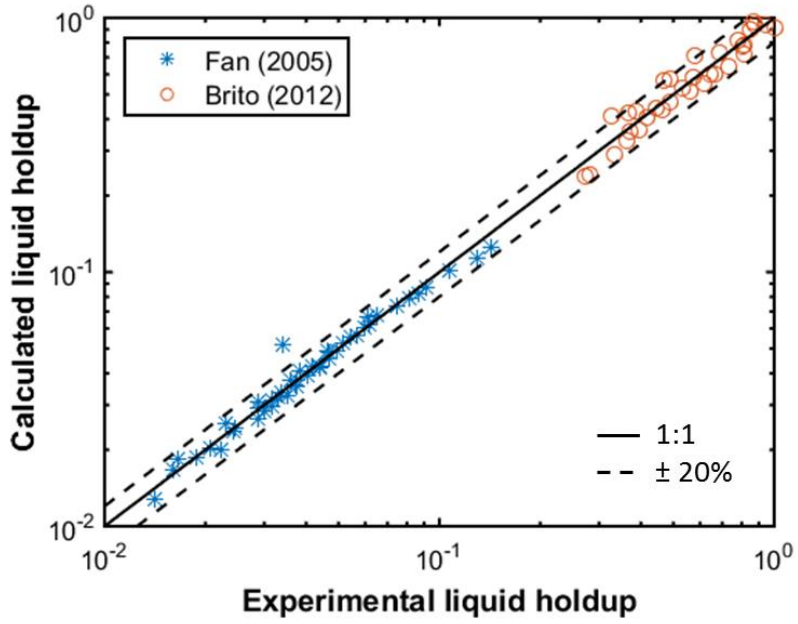

Figure 4.3–Comparison of calculated liquid holdup and experimental liquid holdup for horizontal pipes (experimental data adapted after Fan 2005; Brito 2012).

In the original Shi's model, the limit of θ in Eq. (4.10) is from 0° to 88°. When θ equals 90° (or within 2° of horizontal), $f(\theta)=0$, a zero drift velocity, $v_{dm}=0$, is applied (Schlumberger 2014). We apply the proposed horizontal model for θ between 88° and 90°. A homogeneous flow model (C_o=1, v_{dm}= 0) will also be investigated for comparison purpose.

4.3 Model Verification

A synthetic case is established for model verification. The case is set up as shown in Figure 4.4(a). A small reservoir with a dimension of 500ft × 300ft × 100ft is incorporated as the boundary condition for the wellbore model. The reservoir is located at a depth of 6050ft and is discretized into 5×3×1 grids. The reservoir is assumed to be a gas reservoir with a relative permeability performance shown in Figure 4.4(b). A horizontal well is assumed to have only one perforation inside the reservoir. The vertical and slanted part of the well is uniformly discretized into 31 segments with a length of 202.57ft. Segments 30 and 31 have an inclination angle of 30° and 60° respectively. The horizontal part of the well is uniformly discretized into 3 segments with a length of 200ft. The end segment 34 is connected with the reservoir grid. Other reservoir, wellbore and fluid properties applied in the model are presented in Table 4.1.

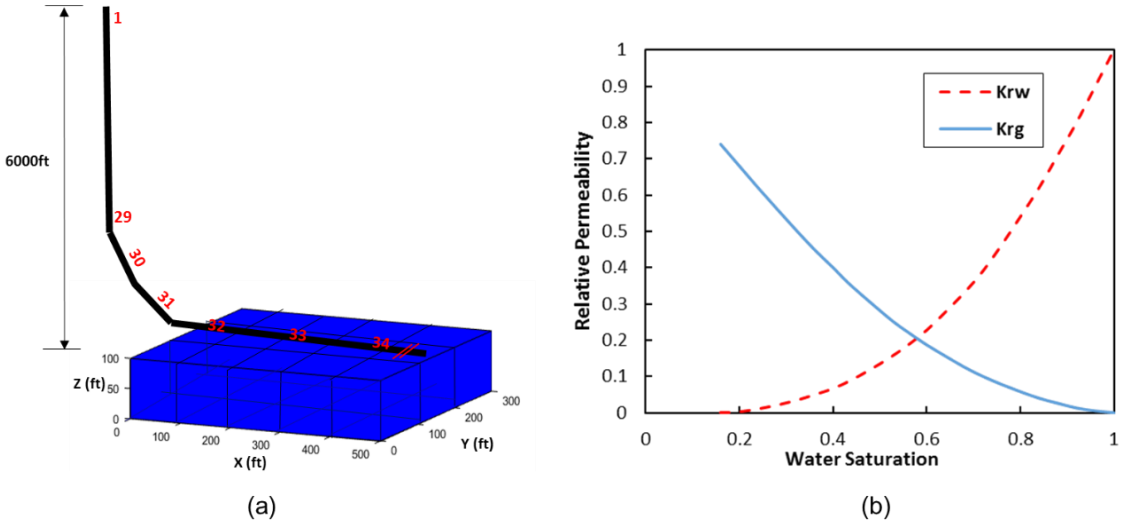

Figure 4.4–(a) Reservoir and wellbore layout of the synthetic verification case, and (b) relative permeability curves applied in the reservoir model.

Parameter	Value	Units
Reservoir properties		
Initial reservoir pressure	5600	psia
Initial water saturation	0.3	-
Reservoir temperature	200	F
Reservoir porosity	0.3	-
Reservoir permeability	10	mD
Rock compressibility	4×10^{-6}	psi^{-1}
Wellbore properties		
Wellbore diameter	0.5	ft
Wellbore relative roughness	0.0005	-
Well index (geometry)	9.1	rcf·cp/day/psi
Maximum gas produce rate	15	MMscf
Minimum tubing head pressure	100	psia
Fluid properties		
Water viscosity	0.31	cp
Water compressibility	3×10^{-6}	psi^{-1}
Gas fluid composition	10.0 CO_2 90.0 CH_4	mol%

Table 4.1–Wellbore and reservoir parameters for the verification case.

The model is compared with the Multi-segment Well model in ECLIPSE 300 (E300) for verification purposes. First, a basic multi-segment well model with a homogeneous wellbore fluid flow assumption (C_o=1, v_{dm}= 0) is applied. Figures. 4.5(a) and 4.5(b) show that the two models match well in both comparisons of gas producing rate and the pressure of perforated well segment. The simulation results represent an ideal situation that all produced water is lifted out of the wellbore, which is also the result that a common reservoir simulator will present. Figure. 4.6(a) compares the pressure along the wellbore at the 10th day of the production. Figure 4.6(b) compares the frictional pressure drop along the horizontal wellbore for the whole production period. The comparison results further validate the reliability of the wellbore model.

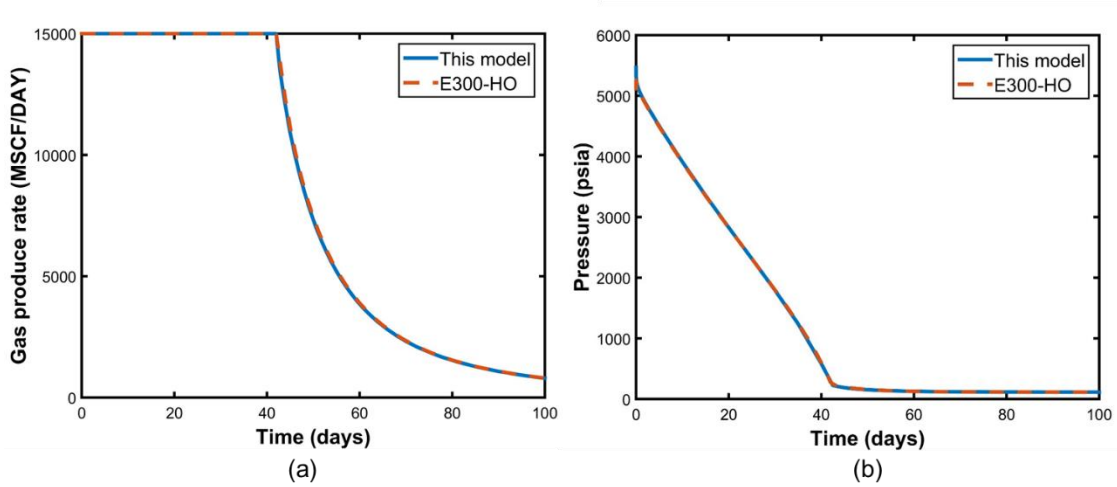

Figure 4.5–Comparisons of (a) gas producing rate and (b) the pressure of the perforated well segment between the proposed model and E300.

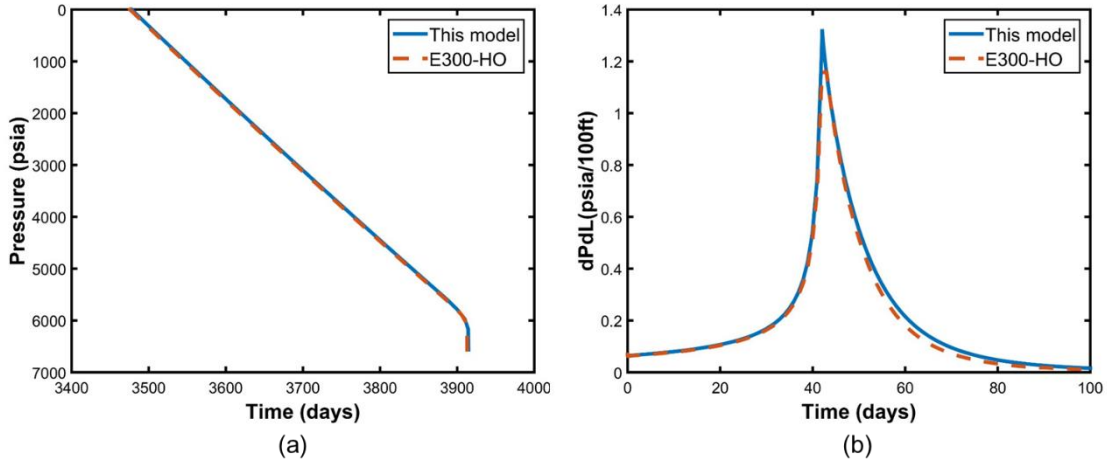

Figure 4.6–Comparisons of (a) wellbore pressure at the 10th day of production and (b) frictional pressure drop of the horizontal lateral between the proposed model and E300.

Furthermore, we apply the modified wellbore drift-flux model and compare the simulation results with E300, which implements the original drift-flux model proposed by Shi et al. (2005) for vertical and deviated pipes, and the homogeneous flow model for horizontal pipes. The relevant drift-flux parameters applied in the E300 model are [A, B, F_v, a_1, a_2] = [1.2, 0.6, 1.0, 0.05, 0.13]. The comparison results of gas producing rate and the pressure of perforated well segment are shown in Figure 4.7(a) and (b). Both results show a sharp drop on gas rate decline curve, accompanied by a sharp increase on the pressure of the perforated segment around the 60th day of production. These two observations are consistent with the liquid loading symptoms reported by Lea and Nickens (2004). The modified model predicts the onset of liquid loading about 1 day earlier than the original model. After the onset of liquid loading, the original model predicts a smoother decline of gas producing rate than the modified model.

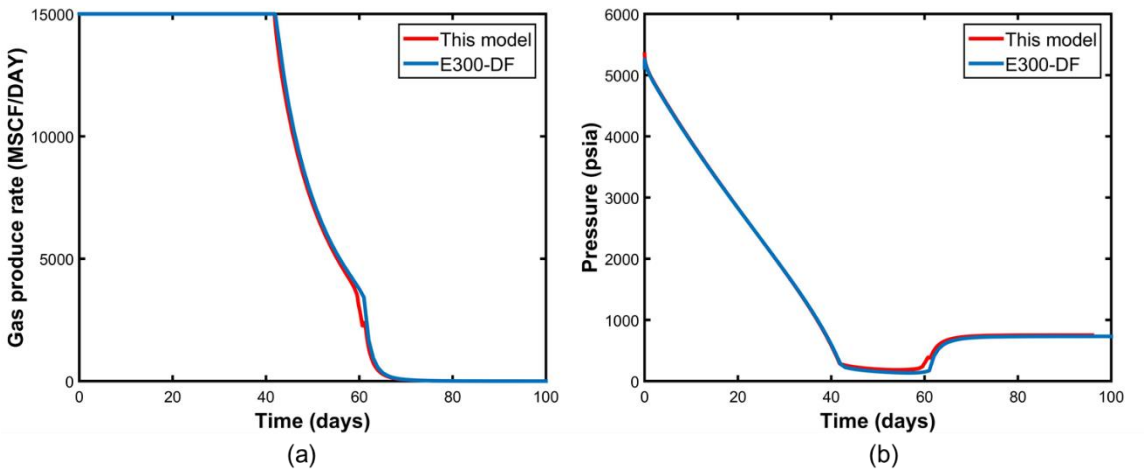

Figure 4.7–Comparisons of (a) gas producing rate and (b) the pressure of perforated well segment simulated from the modified drift-flux model and the original model of Shi et al. (2005).

4.4 Flow Regime Transition Analysis

Figure 4.8(a) shows an expanded view of gas producing rate predicted by the modified model from 59 to 62 days. Figure 4.8(b) shows the water producing rate predicted by the modified model during the same time period. We divide this production period into two: the first time period from t_1 =59.6 days to t_2 =60.6 days, the second period begins at t_2 through to t_3 = 61.3 days. The first interval, Δt_{12}, is mainly influenced by flow pattern transition in the vertical and slanted region of the wellbore. The second interval, Δt_{23}, is mainly influenced by flow pattern transition in the horizontal region of the wellbore. Two points in time are specified, namely: t_A = 60.1 days and t_B = 61.1 days, and are selected for further analysis.

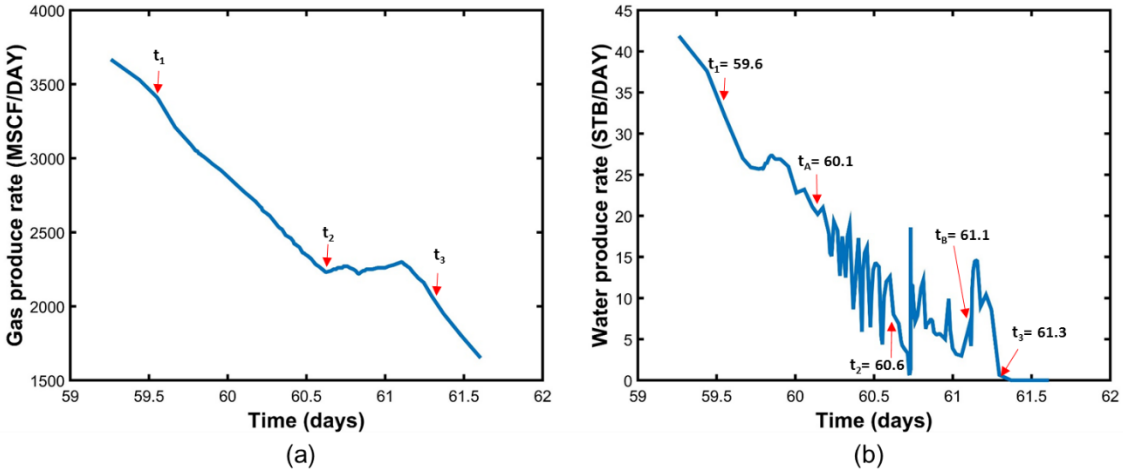

Figure 4.8–Zoom-in view of (a) gas producing rate and (b) water producing rate predicted by the modified model in the time period of 59 day to 62 day.

In the first time section (t_1 to t_2), we compare the superficial gas velocity (v_{sg}) with the critical transition velocity from annular to churn flow (v_{gc} in Equation (4.9)) for all vertical and slanted wellbore segments. The comparison results in Figure 4.9 indicates that the flow pattern transition from annular to churn flow starts at time t_1, located at the bottom of the slanted wellbore region. The time also coincides with the liquid loading onset time shown in Figure 4.7. We can observe that the gas producing rate decline profile remains stable for this flow pattern transition period. We would like to point out that shifting between flow regimes (annular and churn) occurs in the first two well segments (well head) from time t_2 to t_3. It is mainly because of the unstable velocity profile resulting from the flow regime transition in the horizontal section. If we replace the drift-flux model in the horizontal section with the homogenous flow model, the whole wellbore will finish

the flow regime transition at around time t_2 without shifting. The water production also ceases at the same time.

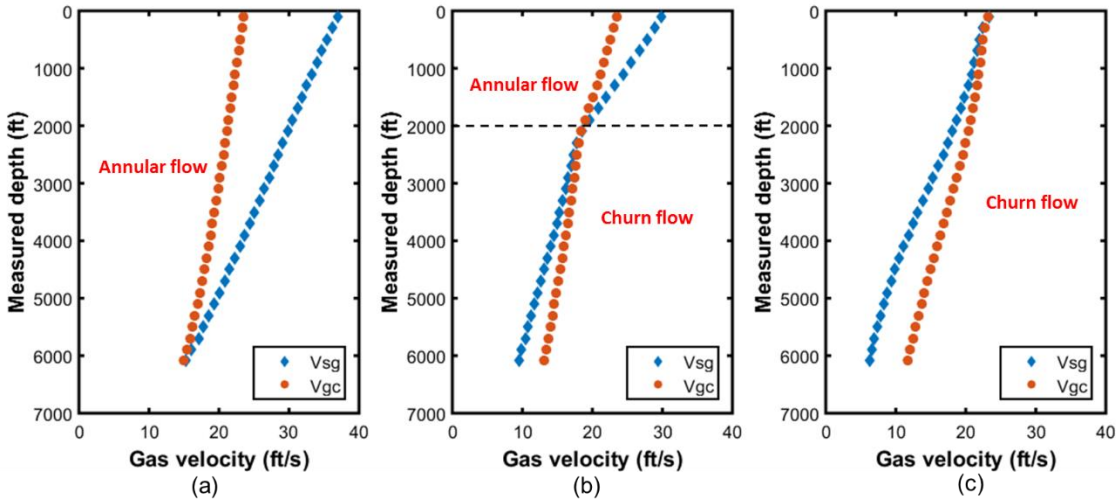

Figure 4.9–Superficial gas velocity and critical gas velocity of vertical and slanted wellbore segments (1 to 31) at different times, (a) t_1, (b) t_{12}, and (c) t_2.

Figure 4.10 presents the calculated liquid holdup for all wellbore segments from time t_1 to t_3. The flow pattern transition criteria (liquid holdups equal to 0.11 and 0.46) for horizontal flow in the modified model are plotted as the black dash lines in the figure. We can observe that the flow pattern transition in horizontal wellbore region starts at time t_2 and completes before t_{23}. However, the impact of the flow pattern transition on wellbore liquid holdup distribution lasts to time t_3, when water completely ceases producing. We define the time period from the onset of liquid loading to the cease of water production (from t_1 to t_3) as the flow regime transition time. For this base case, the total flow regime transition time is approximately 1.7 days.

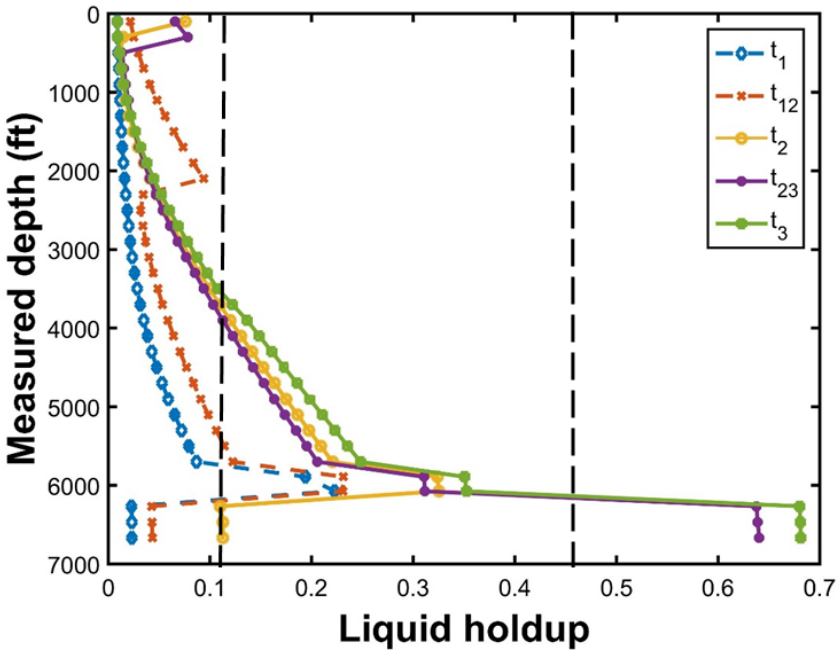

Figure 4.10–Liquid holdup profile along the wellbore at different times from t_1 to t_3.

4.5 Natural Cyclical Production

We design a 3D synthetic reservoir model with a dimension of 1150ft × 1150ft × 200ft. The layout of the reservoir and wellbore is shown in Figure 4.11. The horizontal well is designed to have a 3900ft vertical wellbore section, a 200ft slanted wellbore section and a 560ft horizontal wellbore section. The horizontal lateral of the wellbore is completed in the middle of the reservoir with an open-hole completion of 460ft, which is represented by the red dash line. The reservoir is assumed to produce gas and water simultaneously, and the relative permeability curve of the two phases are the same as that given in Figure 4.4(b). The production is under a maximum gas producing rate constraint of

10000Mscf/day and a minimum tubing head pressure of 100psia. Other reservoir, wellbore and fluid properties are presented in Table 4.2.

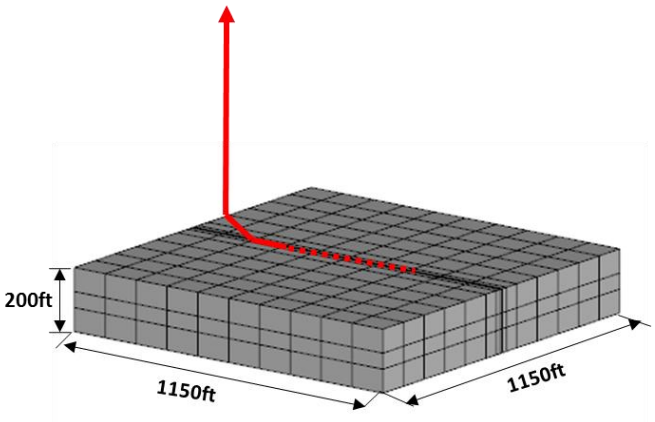

Figure 4.11–Reservoir and wellbore layout of the 3D synthetic case.

Parameter	Value	Units
Reservoir properties		
Initial reservoir pressure	2000	psi
Initial water saturation	0.25	-
Reservoir temperature	100	F
Reservoir porosity	0.1	-
Reservoir depth	4000	ft
Rock compressibility	4×10^{-6}	psi^{-1}
Wellbore properties		
Wellbore diameter	0.5	ft
Wellbore relative roughness	0.0005	-
Maximum gas producing rate	10000	Mscf/day
Minimum tubing head pressure	100	psia
Fluid properties		
Water viscosity	0.31	cp
Water compressibility	3×10^{-6}	psi^{-1}
Gas fluid composition	10.0 CO_2 90.0 CH_4	mol%

Table 4.2–Reservoir and wellbore properties of the 3D synthetic case

We assume the reservoir has homogeneous and isotropic permeability. Figure 4.12 shows the gas and water producing rates when reservoir permeability equals to 1mD. Based on the analysis of the previous section, the liquid loading occurs at time a (202 day), when the flow regime transition from annular to slug flow at the bottom of the slanted wellbore region. The flow regime transition in the whole wellbore is accompanied by the unstable water production (time period a - b). Later, the water production ceases and the gas producing rate drops sharply until reaches economic producing rate (time period b - c). We name time period a – b as gas liquid coproduction period, and time period b - c as zero liquid production period.

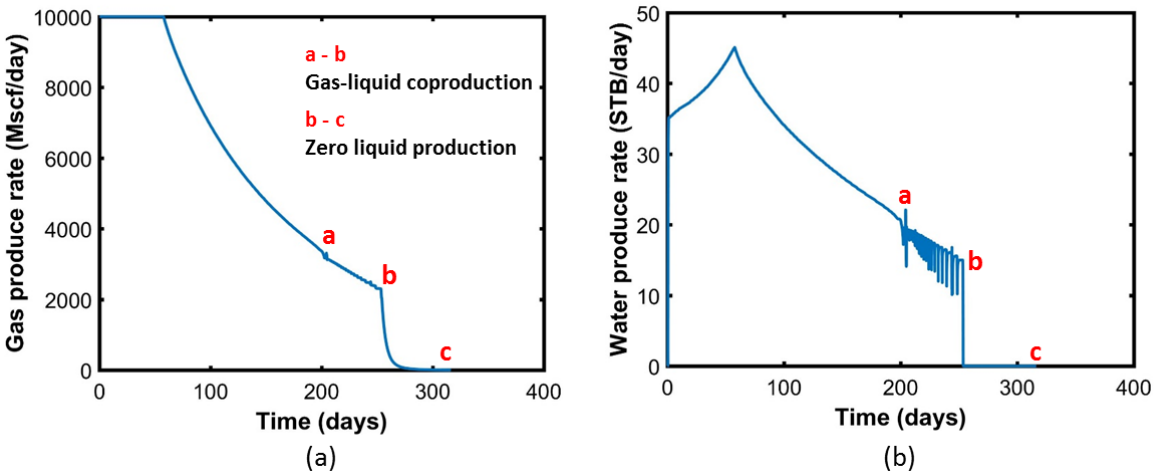

Figure 4.12–(a) Gas producing rate and (b) water producing rate for reservoir permeability equals to 1mD in the synthetic case.

Figure 4.13 shows the lengths of these two production periods under different reservoir permeabilities with 2Mscf/day as economic producing rate. As reservoir

permeability decreases from 5mD to 0.3mD, the gas-liquid coproduction period increases from 8 to 111 days, and the zero liquid production period increases from 23 to 145 days.

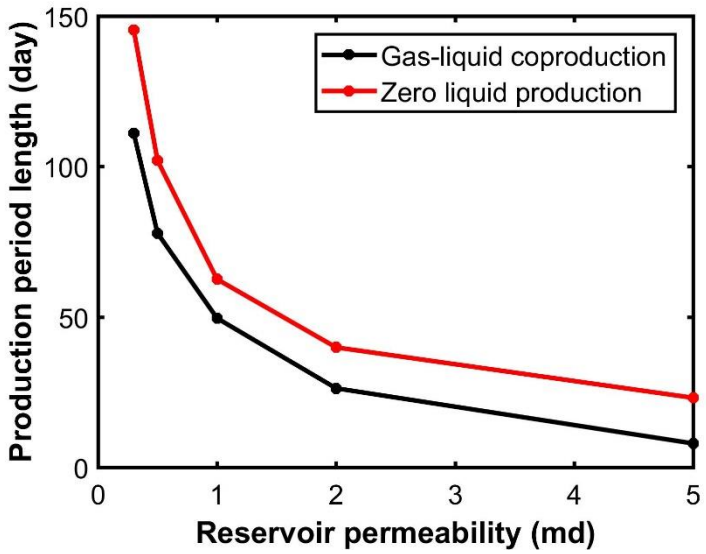

Figure 4.13–Lengths of gas liquid coproduction period and zero liquid production period under different reservoir permeability.

Figure 4.14 presents the gas and water producing rates when reservoir permeability equals to 0.1mD. After the onset of liquid loading (at about 0.7 day), the gas and water coproduce for about 230 days and enter several intermittent production cycles. The maximum water producing rates for the last four producing cycles are 494, 1075, 1648 and 2430STB/day respectively. We analyze a single production cycle from a (265.7 day) to b (302.6 day), and to c (303.1 day), as marked in Fig. 4.14(a).

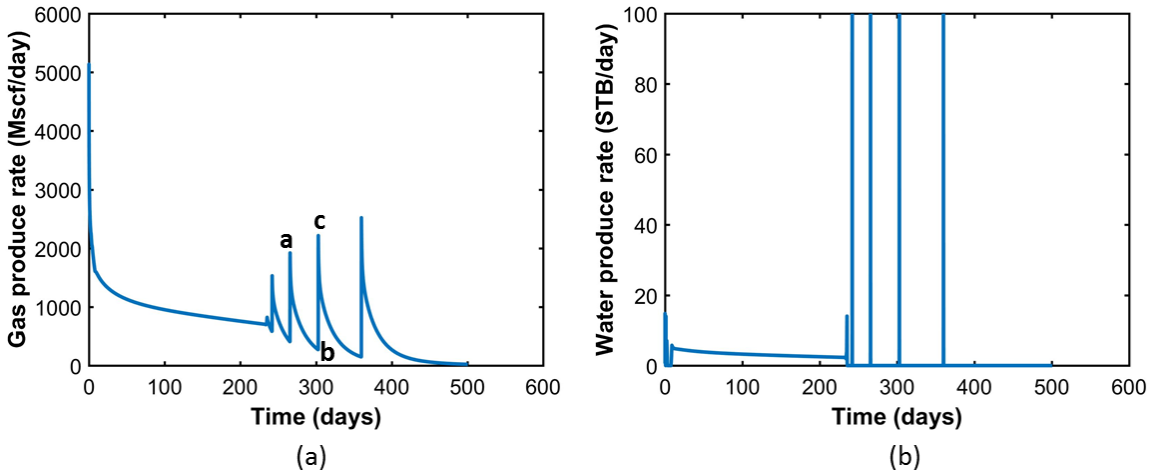

Figure 4.14–(a) Gas producing rate and (b) water producing rate for reservoir permeability equals to 0.1mD.

The dynamic wellbore pressure and reservoir pressure profiles at the last well segment (well toe) are presented in Figure 4.15. For the whole production period, the reservoir pressure remains higher than the wellbore pressure, with the difference gradually decreasing to zero. The reservoir behavior is a little slower than the wellbore behavior. For the production cycle being evaluated, the corresponding characteristic times for reservoir are a' (268 day), b' (302.8 day) and c' (305.4 day).

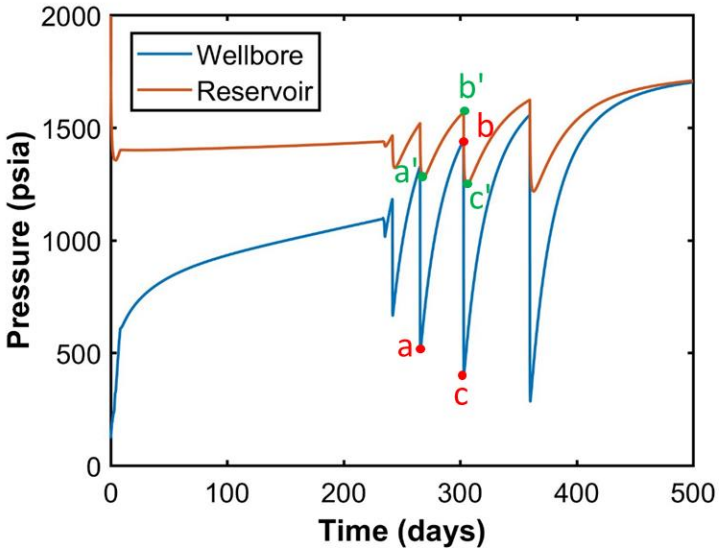

Figure 4.15–Dynamic wellbore pressure and reservoir pressure profiles at the last wellbore segment.

We analyze the static reservoir pressure along the cross section perpendicular to the horizontal wellbore as shown in Fig. 4.16. Fig. 4.16(a) shows the reservoir pressure buildup from time a' to b'. During this 35-day period, the near-wellbore pressure increases from 1274psia to 1568psia, and the far field pressure decreases from 1847psia to 1827psia. Fig. 4.16(b) shows the reservoir pressure drawdown from time b' to c'. During this 3-day period, the far field pressure remains unchanged, and the near-wellbore pressure decreases quickly from 1568psia to 1246psia. We propose the following explanation for this natural cyclical production phenomenon: the low gas producing rate after the onset of liquid loading allows the buildup of reservoir pressure in the near-wellbore region. The accumulated pressure puts the wellbore into another cycle of high gas producing rate accompanied by the removal of accumulated water through production.

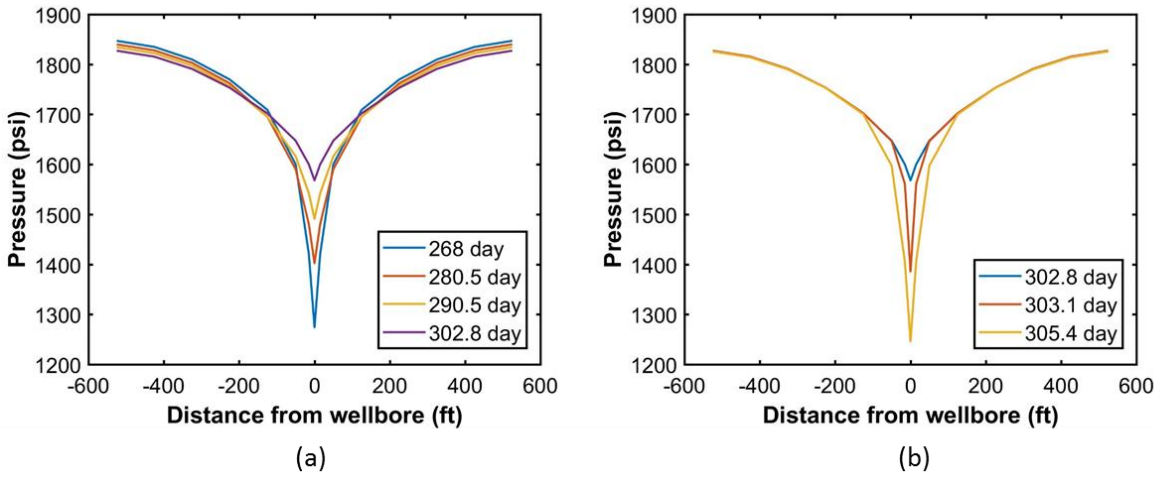

Figure 4.16–Reservoir pressure profiles (a) from time a' to b' and (b) from time b' to c'.

The natural cyclical production phenomenon coincides with several reported field observations. Wang et al. (2015) reported field data of two adjacent gas wells (a horizontal well and a vertical well) in a low-permeable sandstone gas reservoir. The production history indicated that the horizontal well went through several months of intermittent production, while the vertical well produced at a stable low gas flow rate. Marino et al. (2017) also presented field data of a "natural" intermittent production case as shown in Figure 4.17, but they did not provide detailed well information. The natural cyclical production is different from the intermittent production strategy proposed by Whitson et al. (2012). The latter is also known as cyclic shut-in control, which is commonly applied in mature gas fields (Jackson et al., 2011; Limpasurat et al., 2015). The shut-in operation after the onset of liquid loading allows the buildup of reservoir pressure in the near-wellbore region and thus achieves a higher gas flow rate when the well is re-opened.

However, in the natural cyclical production case, the gas producing rate enters the next cycle of high production without shutting in the well. The low gas flow rate after the onset of liquid loading allows the pressure to build up naturally in the near-wellbore region.

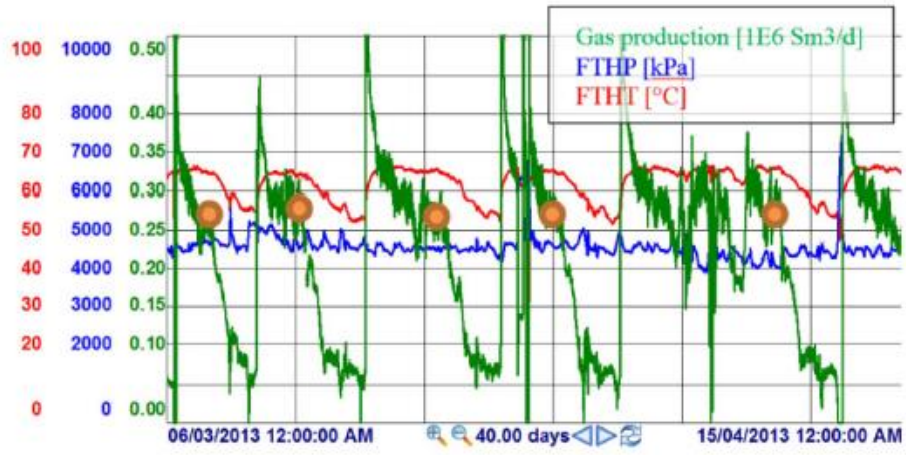

Figure 4.17–Field data of natural cyclical production (reprinted from Marino et al. 2017).

4.6 The Impact of Different Stimulation Techniques

Stimulation techniques are commonly applied to remove near wellbore damage and enhance wellbore productivity in tight gas reservoirs. In this section, we investigate two kinds of stimulation. One is the uniform stimulation in the near-wellbore region, and the other is the multi-stage hydraulic fracturing. The reservoir being investigated is the same size as in the previous case shown in Figure 4.11.

4.6.1 Uniform Near-Wellbore Stimulation

The uniform stimulation cases are simulated by increasing the reservoir permeability around the open-hole wellbore portion. All the other properties are kept the same as in Table 4.2. The stimulated area is 50 ft × 50 ft. We define the stimulation extent (SE) as the ratio of stimulated permeability to matrix permeability. Figure 4.18 shows the gas producing rate and the cumulative gas production when SE is 5 and 10 respectively. Uniform stimulation around wellbore significantly reduces the cycles of intermittent production. When the gas producing rate reaches the lowest economic rate, the cumulative gas production of the two cases are 333 MMscf and 417 MMscf respectively.

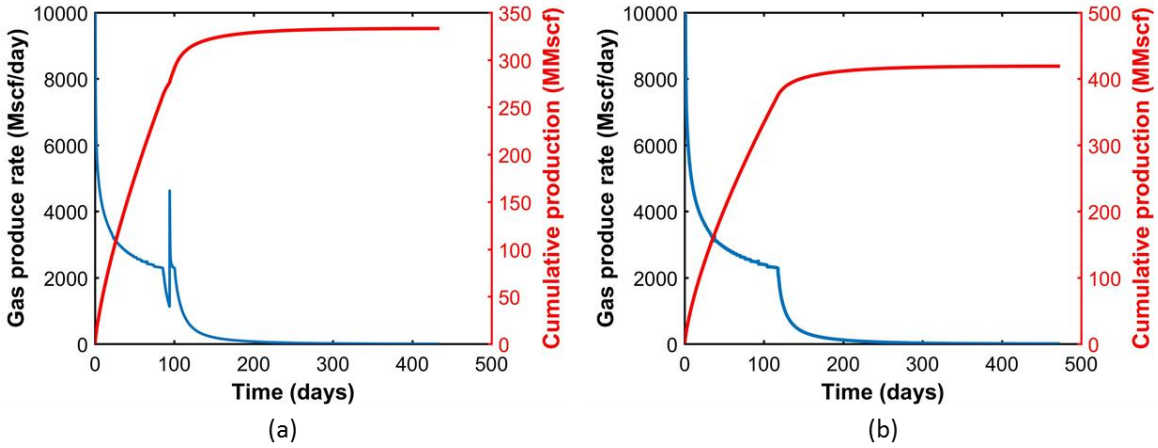

Figure 4.18–Gas producing rate and cumulative gas production for cases with (a) SE = 5 and (b) SE = 10.

Figure 4.19 presents the dynamic wellbore pressure and reservoir pressure profiles at the last well segment. In both cases, the wellbore is first under the maximum producing rate control of 10 MMscf/day and then switches to the minimum tubing head pressure

control of 100 psi. The onset of liquid loading can be recognized through wellbore pressure changes. For the cases with SE is 5 and 10, liquid loading occurs at 23.1 day and 34.9 day respectively.

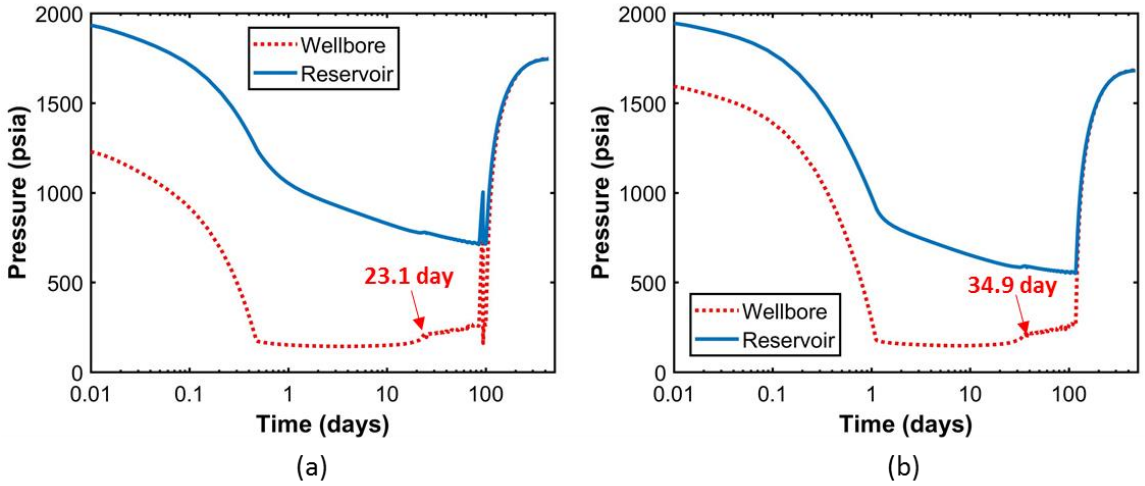

Figure 4.19–Dynamic wellbore pressure and reservoir pressure profiles at the last wellbore segment for cases with (a) SE = 5 and (b) SE = 10.

Figure 4.20 gives the water producing rate profiles of the two cases. After the onset of liquid loading, gas coproduces with water for tens of days and then water production completely ceases, which is also characterized by the sharp increase of wellbore pressure profile. By comparing wellbore pressure and reservoir pressure profiles shown in Figure 4.15 and Figure 4.20, we can find that natural cyclical production occurs when the difference between the wellbore pressure and the reservoir pressure is significant. A high extent stimulation around the wellbore decreases the initial pressure difference between the wellbore and the reservoir, and thus avoids the natural cyclical production.

We further investigate the impact of anisotropic reservoir permeability. In this case, the vertical permeability (k_z) is set to be 0.1 time of the horizontal permeability (k_{xy}) in both reservoir matrix and stimulated volume. The horizontal permeability of reservoir matrix is 0.1 mD. Figure 4.20 shows the gas producing rate and the cumulative gas production for SE equals to 5 and 10. The intermittent production cycle increases significantly. The cumulative gas production rate reaches 329 MMscf after 650 days of production for SE equals to 5. The cumulative gas production reaches 350 MMscf after 607 days of production for SE equals to 10. The same recovery is reached at day 107 for the case with isotropic reservoir permeability (no cyclical production).

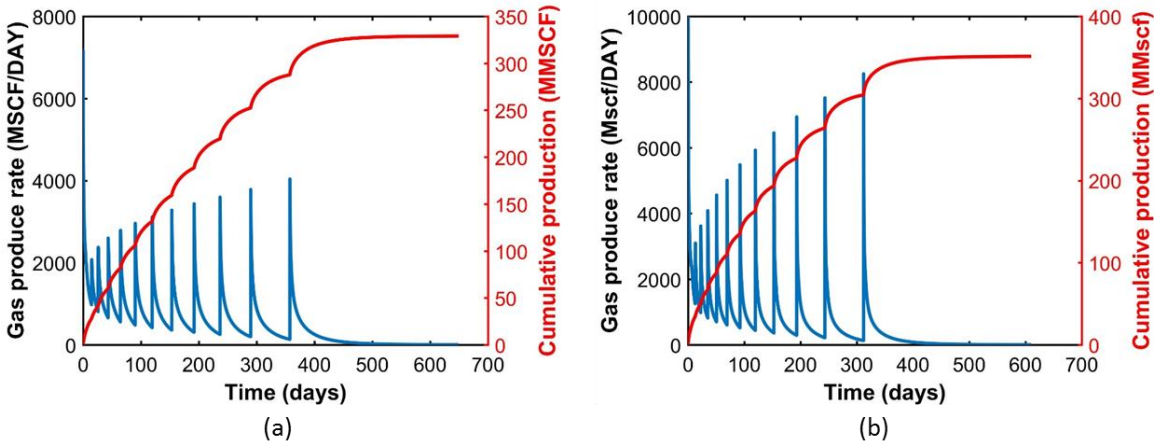

Figure 4.20–Gas production rate and cumulative gas production for anisotropic permeability case with (a) SE = 5 and (b) SE = 10.

Figure 4.21 shows the dynamic wellbore pressure and reservoir pressure profiles for the two stimulation extent. The time for onset of liquid loading is marked on the figure.

The larger initial pressure difference between wellbore and reservoir caused by the lower reservoir permeability enhances the natural cyclical production for both cases.

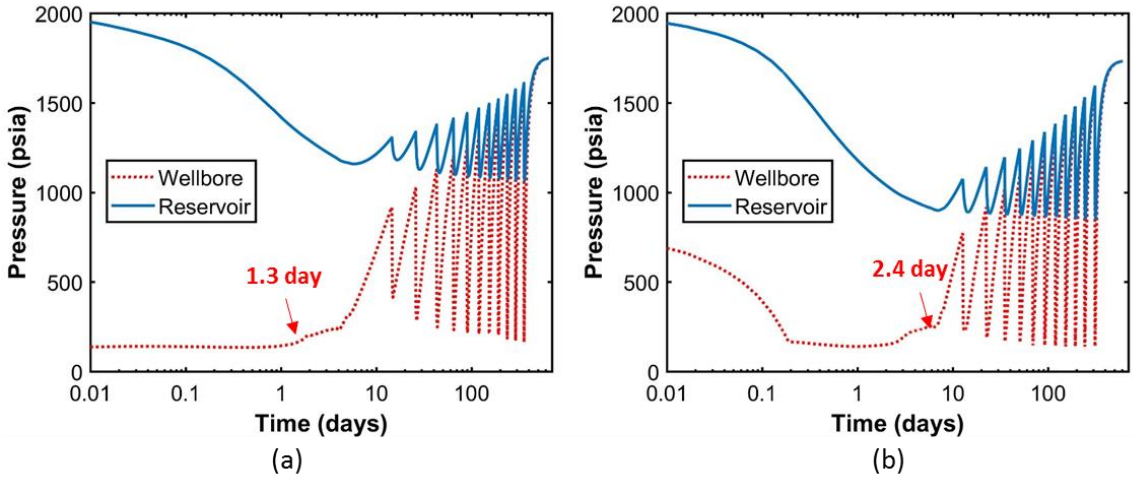

Figure 4.21–Wellbore pressure and reservoir pressure profiles for anisotropic permeability case with (a) SE = 5 and (b) SE = 10.

4.6.2 Multi-Stage Hydraulic Fracturing

To investigate the impact of multi-stage hydraulic fractures, we design a new case in Figure 4.22. The reservoir size and the length of the horizontal wellbore the same as that shown in Figure 4.11. The horizontal lateral of the wellbore has four transverse hydraulic fractures, represented by short white lines. There is local grid refinement around the transverse fractures. The fracture width and permeability are set to be 0.2 ft and 500 mD.

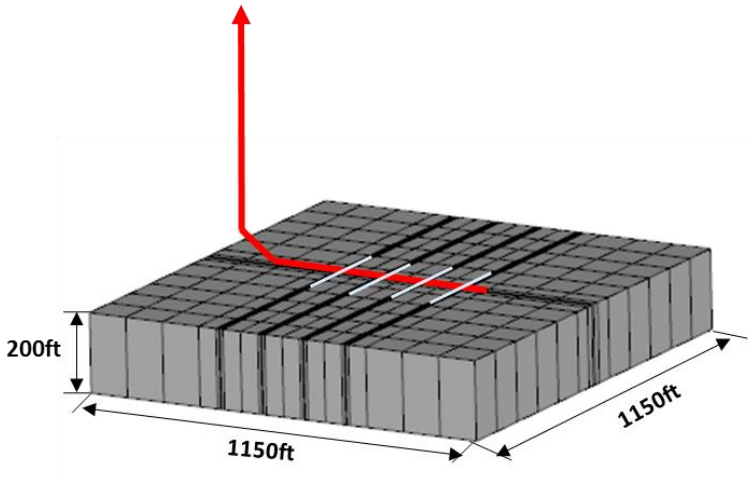

Figure 4.22–Layout of the case with hydraulic fractures

Figure 4.23 shows the gas producing rate and cumulative gas production for fracture length equals to 150 ft and 350 ft respectively. The cumulative production of the two cases are 569 MMscf and 820 MMscf, significantly higher than that of the cases with uniform stimulation. There is no natural cyclical production in either case.

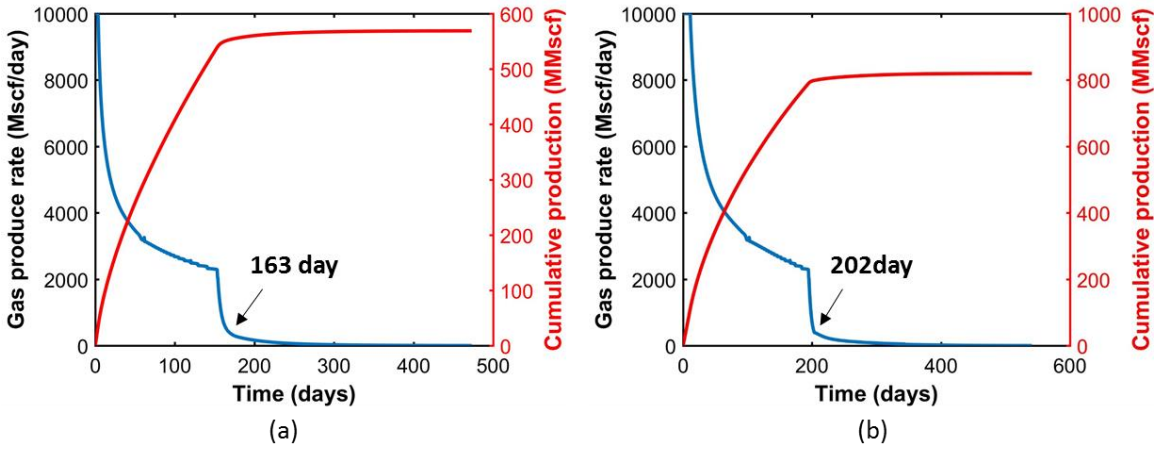

Figure 4.23–Gas production rate and cumulative gas production for cases with fracture length equals to (a) 150 ft and (b) 350 ft.

Based on the dynamic wellbore pressure and reservoir pressure profiles shown in Figure 4.24, the initial pressure differences between wellbore and reservoir of the two cases are both about 500 psi at the onset of liquid loading. For the case with 150 ft fractures, liquid loading occurs at day 57.9 and water production ceases at day 153.5. For the case with 350 ft fractures, liquid loading occurs at day 98 and water production ceases at day 194.7.

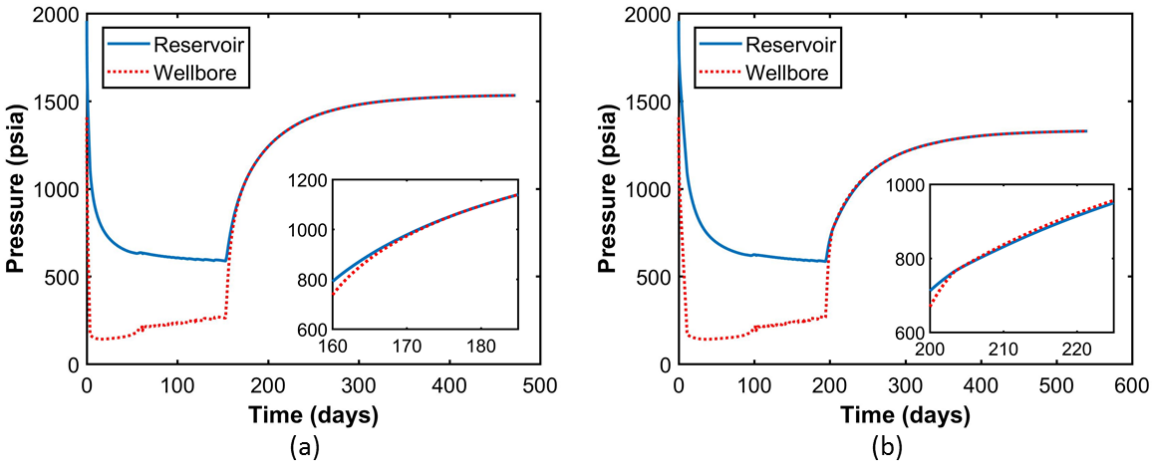

Figure 4.24–Dynamic wellbore pressure and reservoir pressure profiles at the second perforation for cases with fracture length equals to (a) 150 ft and (b) 350 ft.

After the water production ceases, the gas producing rate first drop sharply and then maintains at low producing rates for hundreds of days. Therefore, there exists a transition period associated with the rate changes. For the case with 150 ft fractures, the transition period is smooth and around day 163. For the case with 350 ft fractures, there exists a sharp transition point at day 202. This observation can be explained by the

dynamic changes of wellbore pressure and reservoir pressure shown in Figure 4.24. When all the produced water starts to accumulate in the wellbore, the wellbore pressure increases sharply and the reservoir pressure in the near-wellbore region starts to build up. For the case with 150 ft fractures, the reservoir pressure remains higher than the wellbore pressure during the transition period. However, for the case with 350 ft fractures, the wellbore pressure exceeds the reservoir pressure after 202 days, which indicates the reinjection of wellbore water into the formation.

Figure 4.25 presents the reservoir pressure along the cross section overlay the horizontal wellbore. The dash lines mark the location of hydraulic fractures. In both cases, the reservoir pressure slowly build up in the near-wellbore region after water production ceases. For the case with 150 ft fractures, almost no reinjection happens. For the case with 350 ft fractures, an obvious wellbore fluid reinjection can be recognized after 202 days. The reinjection occurs at the second and the third perforations.

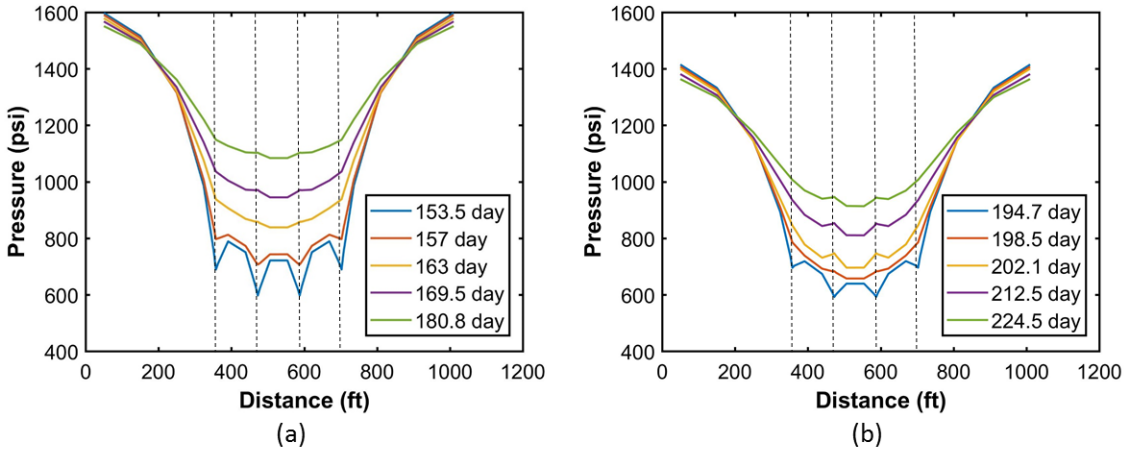

Figure 4.25–Reservoir pressure along the horizontal wellbore for cases with fracture length equals to (a) 150 ft and (b) 350 ft at different times.

Figure 4.26 and Figure 4.27 present the pressure maps of the two cases. When the water production just ceases, the reservoir pressure around the second and the third fractures is significantly smaller than that around the first and the last fractures as shown in Fig. 4.26(a) and Fig. 4.27(a). Fig. 4.26(b) and Fig. 4.26(b) show the reservoir pressure maps during the gas rate transition periods. The pressure around the fractures significantly increases because of the reservoir pressure buildup. However, the pressure around the second and the third fractures remains lower than that of the first and the last fractures, especially for the case with longer fractures. This situation leads to the reinjection from the second and the third perforations, while the first and the last perforations continue producing.

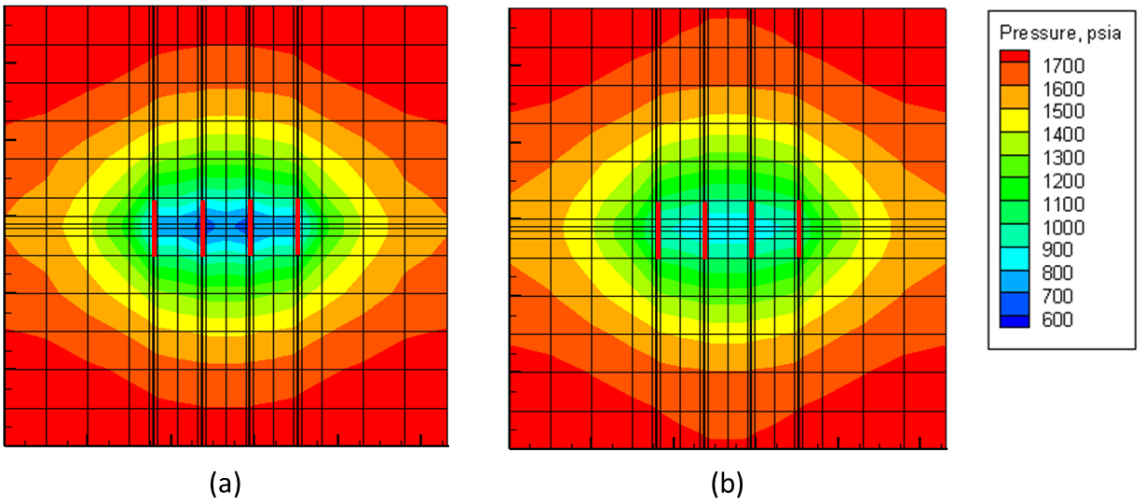

Figure 4.26–Reservoir pressure maps at (a) 153.5 day and (b) 163 day for the case with the fracture length equals to 150 ft.

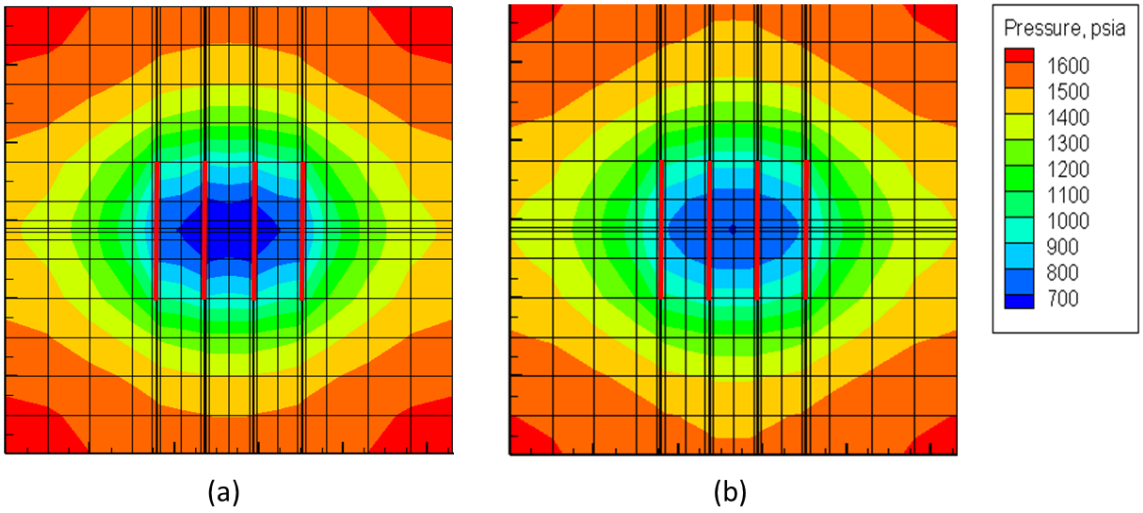

Figure 4.27–Reservoir pressure maps at (a) 194.7 day and (b) 202.1 day for the cases with the fracture length equals to 350 ft.

4.7 Conclusions

In this chapter, we for the first time applied a fully implicitly coupled wellbore-reservoir model GURU-MSW to characterize the liquid loading phenomenon. We proposed a modified drift-flux model that is able to predict the transition from annular or stratified flow regime to churn or slug flow regime for nearly vertical, nearly horizontal and horizontal pipes. The modified model was incorporated into GURU-MSW to simulate the whole producing life of a liquid-loaded horizontal gas well. We applied the model to analyze the gas and water production scenarios of an open-hole horizontal well, a horizontal well with uniform stimulation, and a horizontal well with multi-stage hydraulic fractures. The following conclusions can be obtained:

(1) There exists a gas-water coproduction period and a zero liquid production period after the onset of liquid loading for most production scenarios being investigated. The lengths of both production periods increase as reservoir permeability decreases from 5mD to 0.3mD.

(2) For reservoir permeability equals to 0.1mD, the horizontal gas well experiences natural cyclical production after the onset of liquid loading. It is because of the periodic buildup and draw down of reservoir pressure. The production phenomenon is consistent with reported field observations.

(3) Stimulation techniques such as near wellbore stimulation and hydraulic fracturing can decrease the initial pressure difference between wellbore and near-wellbore reservoir when liquid loading occurs, and thus mitigate or eliminate the natural cyclical production phenomenon.

5. A NEW UNIFIED DRIFT-FLUX MODEL FOR ALL PIPIE INCLINATIONS

Implementation of a drift-flux multiphase flow model within a fully-coupled wellbore-reservoir simulator like GURU-MSW is non-trivial and must adhere to a number of very strict requirements in order to ensure numerical robustness and convergence. The existing drift-flux model inside ECLIPSE/INTERSECT is only fully posed for upward flow from 2 degrees (from the horizontal) to vertical. In this chapter, we attempt to extend the current DF model to a unified and numerically robust model that is applicable to all well inclinations.

In order to achieve this objective, some 5805 experimental measured data from 22 sources as well as 13440 data points from the OLGA-S library were utilized to parameterize a new DF model – one that makes use of the accepted upward flow DF model and a new formulation extending this to the horizontal and downward flow. The proposed model is compared against 2 existing drift-flux models (also applicable to all inclinations) and is shown to have better, or equivalent, performance. More significantly, the model is also shown to be numerically smooth, continuous and robust for co-current flow when implemented to GURU-MSW.

5.1 Model Development

In the new model, we apply the same profile parameter proposed by Shi et al. (2005). This has been given in section 4.2. We repeat it in a combined form as shown in Eq. (5.1).

$$C_0 = \frac{A}{1+(A-1)\times min\left[\left(\frac{\max\left(\alpha_g, \frac{\alpha_g |v_m|}{V_{sgf}}\right)-B}{1-B}\right)^2, 1\right]} \tag{5.1}$$

The profile parameter changes within the range $1 \leq C_0 \leq A$. C_0 will be a constant of 1 if A equals to 1.

The drift-velocity correlation comes from the idea of Bendiksen (1984), which combines drift velocity components for both horizontal and vertical flow as follows:

$$v_d = v_d^v sin\theta + v_d^h cos\theta. \tag{5.2}$$

For the vertical drift velocity (V_d^v), we apply the existing drift-velocity expression documented by Holmes (1977) and Shi et al. (2005), namely:

$$v_d^v = \frac{\left(1-\alpha_g C_o\right) C_o K\left(\alpha_g\right) V_c}{\alpha_g C_o \sqrt{\rho_g / \rho_l} + 1 - \alpha_g C_o}. \tag{5.3}$$

For the horizontal drift velocity (V_d^h), we propose the following correlation:

$$v_d^h = \sqrt{gD}\left(N_1 - N_2\left[\frac{(N_\mu)^{N_4}}{(N_{Eö})^{N_3}}\right]\right)\left(\alpha_g\left[1-\alpha_g\right]\right). \tag{5.4}$$

In Equation (5.4), viscosity number (N_μ) is defined as:

$$N_\mu = \frac{\mu_l}{\left(\rho_l - \rho_g\right) D^{1.5} \sqrt{g}} \tag{5.5}$$

Eötvös number ($N_{Eö}$) is defined as:

$$N_{Eö} = \frac{g\left(\rho_l - \rho_g\right) D^2}{\sigma_{gl}} \tag{5.6}$$

The first and second terms in Eq. (5.4) are inspired by the work of Ben-Mansour et al. (2010), Jeyachandra et al. (2012), and Zukoski (1966). The horizontal drift velocity has been shown to be highly dependent on gas volume fraction (Isao and Mamoru, 1987). The purpose of the third term in Eq. (5.4) is to ensure that the horizontal drift velocity approaches to 0 as gas volume fraction approaches to 0 and 1.

The correlation in Eq. (5.3) was designed for upward and horizontal flow $0° \leq \theta \leq 90°$. For downward flow, Bhagwat and Ghajar (2012) observed that drift-flux models developed for upward flow can be applied to downward flow by changing the sign the of the drift velocity term from positive to negative. They further proposed a model where the "sign flipping criteria" are defined at $-50° \leq \theta < 0°$ and when $Fr_{sg} \leq 0.1$ (Bhagwat and Ghajar, 2014). Fr_{sg} is the gas Froude number defined by Eq. (A.6). However, the model is based on superficial gas velocity and is discontinuous in form, making it unsuited for implementation in coupled wellbore-reservoir simulation. This is contrary to typical steady-state pipe-flow multiphase simulators where superficial velocities are known

inputs and void fraction is an output. In coupled wellbore-reservoir simulation, this is reversed and void fraction is an input and superficial velocities are the outputs.

To fulfill our application objective, we propose the following drift velocity correlation, applicable for all pipe inclinations:

$$v_d = \left(m_1 v_d^v sin\theta + \left[1 - \frac{2}{1+exp\left(50 * sin\left(\theta + m_2 v_m\right)\right)} \right] v_d^h cos\theta \right) \left(1 + \frac{1000}{Re_L + 1000} \right)^{m_3} \tag{5.7}$$

Equation (5.7) adds two new terms to the original correlation shown in Eq. (5.2). One is a logistic function to adjust the horizontal drift velocity term. The logistic function creates a smooth transition between 1 and -1 with the transition location being determined by θ and V_m (the functionality of this term will be illustrated in the discussion Section). The second term utilizes the liquid Reynolds number defined by Eq. (5.8). The term accounts for deviations observed at low velocity (at low Reynolds number).

$$Re_L = \frac{v_m \rho_l D}{\mu_l} \tag{5.8}$$

5.2 Model Parameterization

The average in-situ gas volume fraction (α_g), across the pipe cross-section, is obtained by solving the following implicit function:

$$f\left(\alpha_g;\, X_p, \xi\right) = \frac{v_{sg}}{C_o\left(\alpha_g;\, X_p, \xi\right) v_m + v_d\left(\alpha_g;\, X_p, \xi\right)} - \alpha_g = 0 \tag{5.9}$$

X_p are tunable model parameters, and ξ are input fluid properties. The Wijngaarden-Dekker-Brent root-finding algorithm (Press et al., 1992) is applied to solve Eq. (5.9). If

multiple roots are found, the lower one is taken as the physical root (Landman, 1991). The vector X_p contains the following eleven empirical parameters from the model:

$$X_p = \left[A, B, a_1, a_2, N_1, N_2, N_3, N_4, m_1, m_2, m_3\right]$$

These parameters are obtained by minimizing the average error between the experimental and calculated gas volume fraction. The objective function is defined as:

$$F_{obj} = \frac{1}{N}\sum_{i=1}^{N}\left|\alpha_g^{exp} - \alpha_g^{cal}\right| \tag{5.10}$$

The parameters are optimized between the lower- and upper-bounds as follows:

$$\left(X_p\right)_{lower} = \left[1.0, 0.1, 0.1, 0.3, 0.1, 0.1, 0.1, 0.1, 0.5, 1.0, 0.5\right]$$

$$\left(X_p\right)_{upper} = \left[1.5, 0.9, 0.7, 0.9, 2.0, 2.0, 1.0, 1.0, 2.0, 3.0, 2.0\right]$$

We utilize two distinct datasets to determine optimal model parameters. The first dataset contains 5805 data extracted from the Tulsa University Fluid Flow Project (TUFFP) database. This contains experimental data from 22 sources, all in the public domain with a summary of sources and property ranges in Table B-1. Worthy of note is the fact that the data covers pipe inclinations in the range $-90° \leq \theta \leq 90°$ and pipe diameters from 1 to 6.73 inches. The second dataset comprises 13440 records generated from the OLGA-S library. The OLGA-S library is derived from high-quality experimental data from the SINTEF multiphase flow laboratory near Trondheim, Norway (Schlumberger, 2017b). This dataset covers pipe inclinations in the range of $80° \leq \theta \leq 90°$ and pipe diameters from 1 to 7 inches. Table 5.1 summarizes the range of key properties of these datasets, including superficial

velocities, viscosities and gas volume fraction. Both datasets cover the typical operational range of gas and oil wells.

Variables	Pipe diameter (inch)	Inclination (degree)	Gas superficial velocity (m/s)	Liquid superficial velocity (m/s)	Liquid Viscosity (cP)	Gas volume fraction
TUFFP Dataset						
Min	1.0	-90	0.023	0.0003	0.1	0.006
Max	6.7	90	82.32	5.2	74.4	0.999
OLGA-S Dataset						
Min	1.0	-80	0.0001	0.001	0.5	0.0001
Max	7.0	90	14.976	14.965	50.0	0.997

Table 5.1–Data range of the TUFFP dataset and the OLGA-S dataset for model parameterization.

Figure 5.1 plots the distributions of the two datasets over gas input fractions ($f_g=V_{sg}/V_m$), pipe inclinations and pipe diameters. We can observe that the TUFFP dataset is concentrated at the higher-end of gas input fraction range ($f_g > 0.8$). Conversely, the dataset extracted from OLGA-S library has a more uniformly distributed gas input fractions. We also note that the TUFFP dataset has 2138 data points applicable to pure horizontal flow ($\theta=0°$), and 966 data points for pure vertical flow ($\theta=90°$). Contrary to such bias, the OLGA-S dataset is more evenly distributed in near horizontal flow ($\theta = [-5°, -2°, -1°, 0°, 1°, 2°, 5°]$) and also more evenly spread over other pipe inclinations. Finally, we note that TUFFP dataset has a greater propensity of small diameter conduits while data obtained from OLGA-S is uniformly distributed over the four pipe diameters considered, $D \in$ (1, 3, 5, 7) inches. Note that while field units are stated here, all calculations except the reservoir simulation part used the SI system.

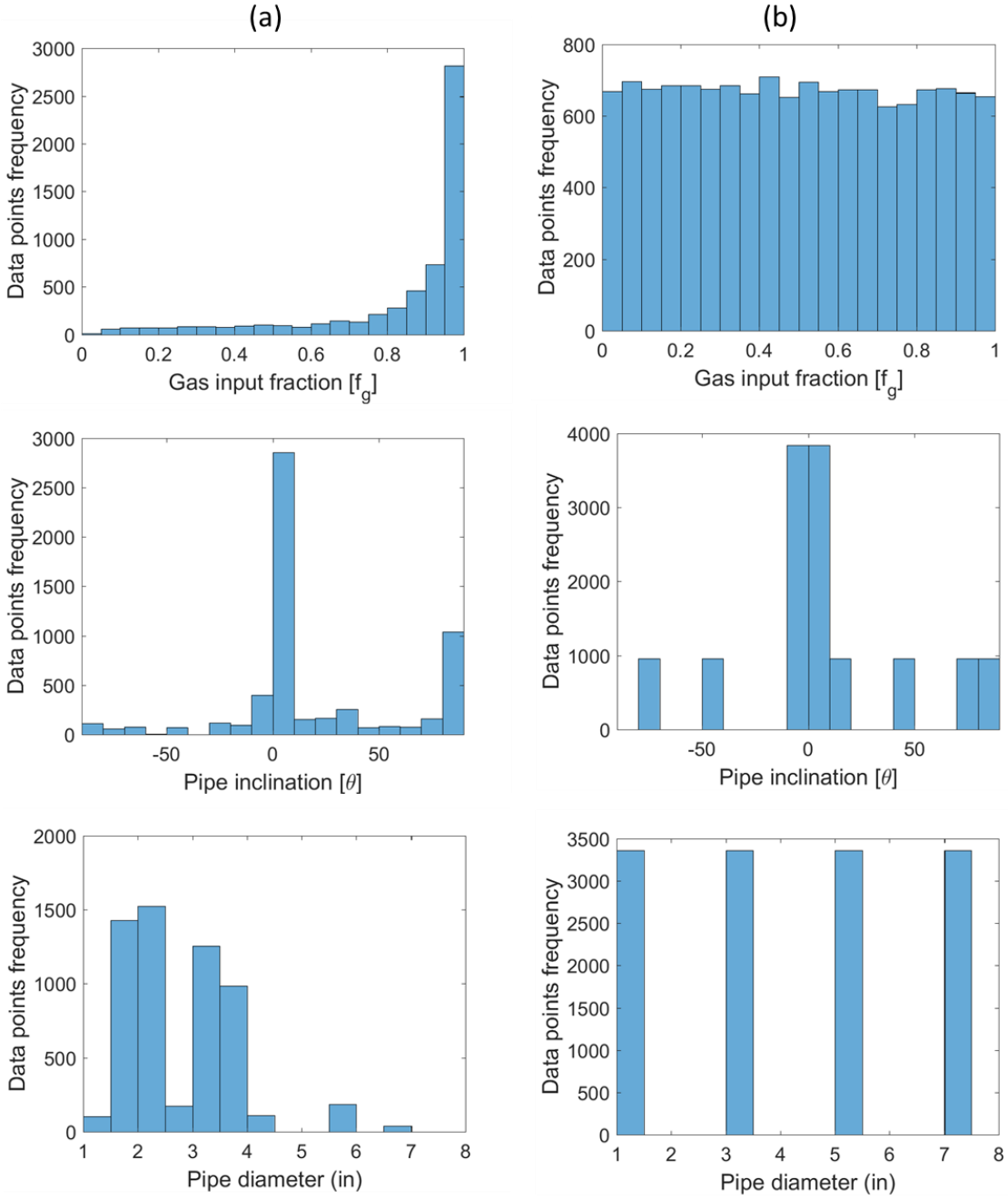

Figure 5.1–Distributions of (a) TUFFP dataset and (b) OLGA-S dataset over gas input fraction, pipe inclination and pipe diameter.

5.3 Other Models Used for Comparison

Two state-of-the-art drift-flux models from literature are used for comparative analysis. One is the model proposed by Choi et al. (2012), while the other is that of Bhagwat and Ghajar (2014). Henceforth, we shall refer to these models as Choi's model and B&G's model. The B&G's model was claimed by the authors to be the best performing model in the literature so far.

The model proposed by Choi et al. (2012) is as follows:

$$C_o = \frac{2}{1+\left(Re_{tp}/1000\right)^2} + \frac{1.2-0.2\sqrt{\frac{\rho_g}{\rho_l}}\left(1-e^{\left(-18\alpha_g\right)}\right)}{1+\left(1000/Re_{tp}\right)^2} \tag{5.11}$$

$$v_d = 0.0246cos\theta + 1.606\left(g\sigma_{gl}(\rho_l-\rho_g)/\rho_l^2\right)^{0.25} sin\theta \tag{5.12}$$

The Re_{tp} has the same definition as shown in Equation (5.8).

The model proposed by Bhagwat and Ghajar (2014) is as follows:

$$C_o = \frac{2-\left(\frac{\rho_g}{\rho_l}\right)^2}{1+\left(\frac{Re_{tp}}{1000}\right)^2} + \frac{\left[\left(\sqrt{\left(1+\left(\frac{\rho_g}{\rho_l}\right)^2 cos\theta\right)/\left(1+cos\theta\right)}\right)^{1-\alpha}\right]^{0.4} + C_{o,1}}{1+\left(\frac{1000}{Re_{tp}}\right)^2} \tag{5.13}$$

where,

$$C_{o,1} = \begin{cases} 0 & \text{for } -50° \le \theta \le 0° \text{ and } Fr_{sg} \le 0.1 \\ \left(C_1 - C_1\sqrt{\frac{\rho_g}{\rho_l}}\right)\left[\left(2.6-\beta\right)^{0.15} - \sqrt{f_{tp}}\right]\left(1-\chi\right)^{1.5} & \text{otherwise} \end{cases} \tag{5.14}$$

Coefficient C_1=0.2 for circular and annular pipe geometries, and

$$\beta = \frac{u_{sg}}{u_{sl} + u_{sg}} \tag{5.15}$$

The Froude number for superficial gas velocity is defined as:

$$Fr_{sg} = \sqrt{\frac{\rho_g}{\rho_L - \rho_g}} \frac{u_{sg}}{\sqrt{gD\cos\theta}} \tag{5.16}$$

χ is two phase flow quality defined as follows:

$$\chi = \frac{v_{sg}\rho_g}{v_{sg}\rho_g + v_{sl}\rho_l} \tag{5.17}$$

The friction factor f_{tp} is defined by Fanning function:

$$\frac{1}{f_{tp}} = -4.0\log_{10}\left(\frac{\varepsilon / D}{3.7} - \frac{1.256}{Re_{tp}\sqrt{f_{tp}}}\right) \tag{5.18}$$

The drift velocity is defined as:

$$v_d = (0.35\sin\theta + 0.45\cos\theta) \times \sqrt{\frac{gD(\rho_L - \rho_g)}{\rho_L}}\left(1-\alpha_g\right)^{0.5} C_2C_3C_4 \tag{5.19}$$

where C_2, C_3, C_4, are defined as follows:

$$C_2 = \begin{cases} \left(\dfrac{0.434}{\log\left(\mu_l / 0.001\right)}\right)^{0.15} & \left(\mu_l / 0.001\right) > 10 \\ 1 & \left(\mu_l / 0.001\right) \le 10 \end{cases} \tag{5.20}$$

$$C_3 = \begin{cases} \left(La / 0.025\right)^{0.9} & La < 0.025 \\ 1 & La \ge 0.025 \end{cases} \tag{5.21}$$

$$C_4 = \begin{cases} -1 & \text{for} -50° \le \theta \le 0° \text{ and } Fr_{sg} \le 0.1 \\ 1 & \text{others} \end{cases} \tag{5.22}$$

La is the inverse of non-dimensional hydraulic pipe parameter defined as:

$$La = \frac{\sqrt{\frac{\sigma_{g-L}}{g(\rho_L - \rho_g)}}}{D} \tag{5.23}$$

5.4 Results

Using the datasets discussed in section 5.2, optimized model parameters were computed and are summarized in Table 5.2. Note that the units of m_2 is deg•s/m, while all others are dimensionless. The best fit parameter set for the OLGA-S dataset includes *A =1*, which indicates that the profile parameter (C_o) equals to 1 for all values of input gas fraction, and effectively renders parameter *B* redundant.

X_p	X_{opt}^{TUFFP}	X_{opt}^{OLGAS}
A	1.088	1.000
B	0.833	0.773
a_1	0.577	0.591
a_2	0.769	0.786
N_1	1.981	1.968
N_2	1.759	1.759
N_3	0.574	0.574
N_4	0.477	0.477
m_1	1.017	1.000
m_2	2.303	2.300
m_3	1.000	1.000

Table 5.2–Optimized parameters for the proposed model determined based on the two datasets.

5.4.1 TUFFP Dataset: Model Comparison

Table 5.3 summarizes the comparative performance of different drift-flux models against the TUFFP dataset. Model error is the mean absolute difference between predicted values and measured values defined by Equation (5.10). The percentage of the predictions located within ±20% and ±10% error bands are also shown in the table. The proposed model with its respective optimized parameter sets has the best performance in all pipe inclination ranges. The model predicts around 90% of the data points within ±20% error bands and 70% of the data points within ±10% error bands, for all pipe inclinations. Although Choi's model also has similar performance within ±20% error bands, far fewer predictions lie within ±10% error bands. The performance of the proposed model with X_{opt}^{OLG} as model parameters is also reasonable compared with the other two drift-flux models. For all three models, the performance in the horizontal flow region are comparable to the accuracy obtained for upward flow prediction. The proposed model and Choi's model have better performance in upward and horizontal flow, while the B&G's model has better predictive performance for downward flow.

Pipe Inclination Range	**Criteria**	**This model (X_{opt}^{TUF})**	**This model (X_{opt}^{OLG})**	**Choi's model**	**B&G's model**
Upward (2730 data) $0° < \theta \leq 90°$	error	0.045	0.06	0.078	0.069
	±20%	90.4	87.9	88.9	83.3
	±10%	73.4	59	45.8	53.9
Horizontal (2138 data) $\theta = 0°$	error	0.042	0.066	0.072	0.077
	±20%	94.2	87.8	90	83.2
	±10%	77.3	62.2	52.7	48
Downward (937 data) $-90° \leq \theta < 0°$	error	0.062	0.072	0.099	0.065
	±20%	88.9	85.1	90	86.9
	±10%	69.9	62	42	67.2

Table 5.3–Statistical comparison of different drift-flux models against the TUFFP dataset.

Figure 5.2 presents cross plots of predicted gas volume fractions for different drift-flux models against measured gas volume fractions for horizontal and upward data in TUFFP dataset. The ±20% and ±10% error bands are shown as dashed lines, respectively. It is clear from the figure that the major differences among models corresponds to high gas volume fraction region ($0.75 < \alpha_g < 1$). The proposed model, using the optimized parameter set X_{opt}^{OLG} tends to overpredict gas volume fraction in this region. This is mainly due to the fact that the profile parameter always equals to 1 in this parameterization. Choi's model tends to under predict gas volume fraction when $\alpha_g > 0.8$. B&G's model tends to over predict gas volume fractions when $\alpha_g > 0.5$.

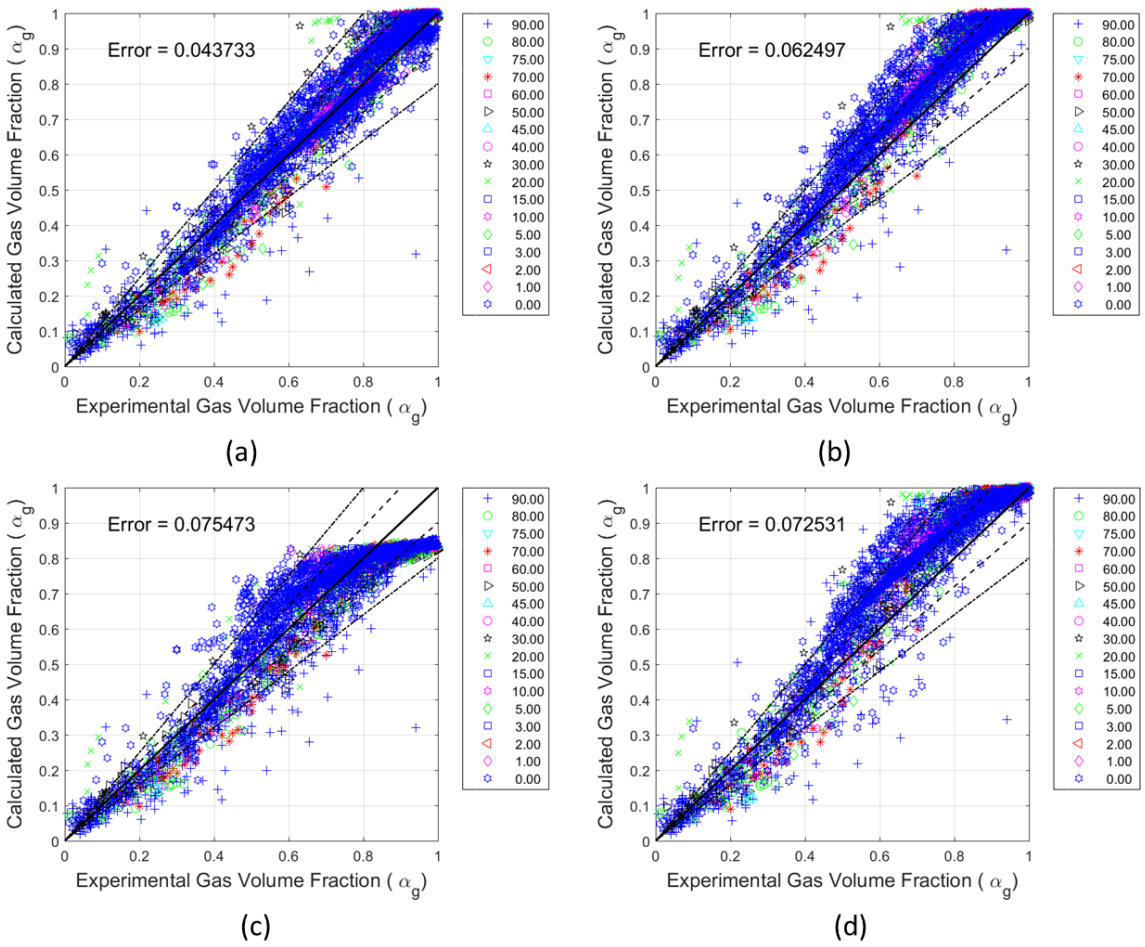

Figure 5.2–Cross-plots of model comparative performance for horizontal and upward flow: (a) the proposed model with X_{opt}^{TUF} parameter set, (b) the proposed model with X_{opt}^{OLG} parameter set, (c) the Choi's model and (d) the B&G's model against upward and horizontal pipe inclinations in the TUFFP dataset.

Figure 5.3 presents similar comparison cross plots for downward flow data in TUFFP dataset. Compared to Figure 5.2, the cross plots for downward flow are more scattered. Outliers of the proposed model are evenly distributed outside the ±20% error bands, while the outliers of Choi's and B&G's model are densely distributed below the –

20% error band. Possible reasons for these significant differences in behavior for downward flow will be discussed later in section 5.6.1.

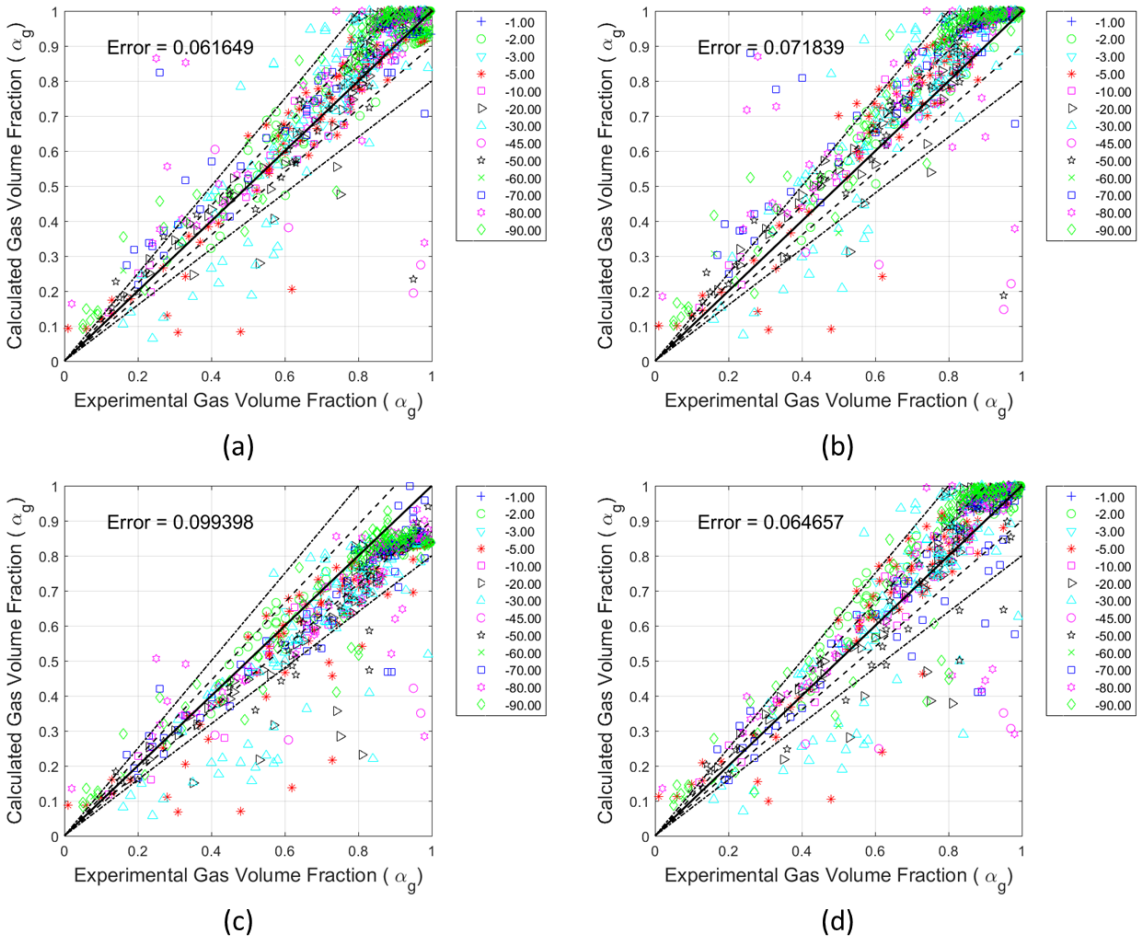

Figure 5.3–Cross-plots of model comparative performance for downward flow: (a) the proposed model with X_{opt}^{TUF} parameter set, (b) the proposed model with X_{opt}^{OLG} parameter set, (c) the Choi's model and (d) the B&G's model against downward pipe inclinations in the TUFFP dataset.

5.4.2 OLGA-S Dataset: Model Comparison

Table 5.4 summarizes the comparative performance of different drift-flux models against the OLGA-S dataset. The predictions of the correlations are all improved over those observed using the TUFFP dataset. It is probably due to data quality, namely that the OLGA-S dataset is more consistent. The performance of the proposed model, applying optimized parameter sets X_{opt}^{TUF} and X_{opt}^{OLG} are similar, with the X_{opt}^{OLG} parameter set slightly outperforming in terms of the quantity of data points falling within ±10% error bands. The proposed model and that of B&G have similar mean absolute errors for both upward and downward inclinations. The error of B&G's model for horizontal flow is slightly higher than that obtained from the proposed model. The performance of the two models are comparable in terms of the percentage of data falling within ±20% and ±10% error bands. In general, however, both models perform significantly better than Choi's model. We also observe that all three models have significantly better performance for upward and horizontal inclinations than they do for downward inclinations.

Pipe Inclination Range	**Criteria**	**This model (X_{opt}^{TUF})**	**This model (X_{opt}^{OLG})**	**Choi's model**	**B&G's model**
Upward (6720 data) $0° < \theta \leq 90°$	error	0.022	0.019	0.050	0.022
	±20%	97.9	97.8	95.4	95.4
	±10%	80.6	90.7	32.4	83.7
Horizontal (960 data) $\theta = 0°$	error	0.023	0.023	0.043	0.027
	±20%	97.3	96.7	96.0	96.3
	±10%	82.0	89.2	43.0	78.8
Downward (6720 data) $-90° \leq \theta < 0°$	error	0.030	0.030	0.055	0.033
	±20%	95.1	94.7	91.6	92.8
	±10%	81.8	84.9	45.0	80.8

Table 5.4–Statistical comparison of different drift-flux models against the OLGA-S dataset.

Figure 5.4 presents cross plots of predicted gas volume fractions for different drift-flux models against measured gas volume fractions for horizontal and upward flow in OLGA-S dataset. The performance of the proposed model, applying X_{opt}^{TUF} and X_{opt}^{OLG} are comparable. The major outliers observed for all three models approximately lie within the mid-range of gas volume fraction ($0.25 < \alpha_g \leq 0.75$), and lie above the +20% error bound. For high gas volume fraction region ($0.75 < \alpha_g < 1$), the proposed model (using both optimized parameter sets) slightly over predicts gas volume fraction. Choi's model tends to under predict the gas volume fraction when $\alpha_g > 0.8$, while B&G's model tends to over predict gas volume fraction when $\alpha_g > 0.5$.

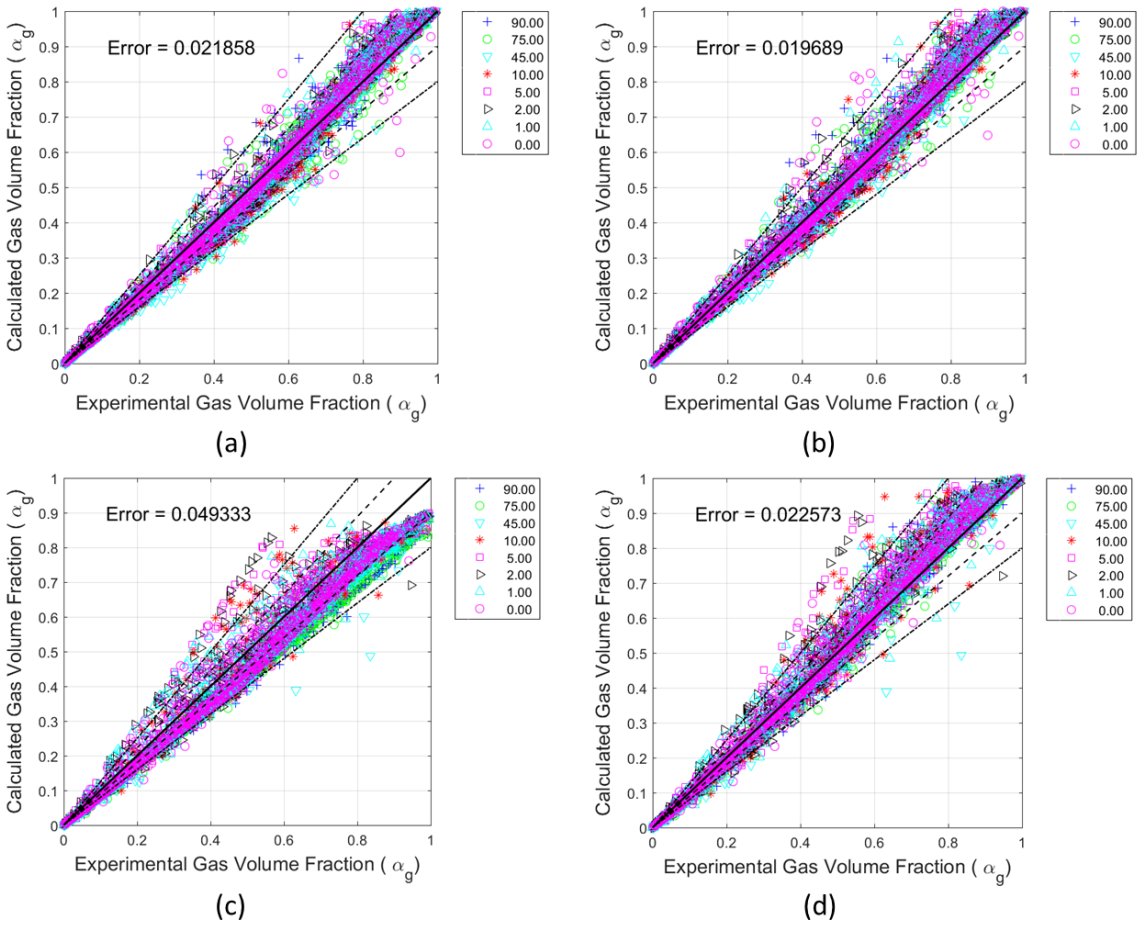

Figure 5.4–Cross-plots of model comparative performance for horizontal and upward flow: (a) the proposed model with X_{opt}^{TUF} parameter set, (b) the proposed model with X_{opt}^{OLG} parameter set, (c) the Choi's model and (d) the B&G's model against upward and horizontal pipe inclinations in the OLGAS dataset.

Figure 5.5 presents comparisons for downward pipe inclinations. We observe similar model behavior as stated previously for the TUFFP dataset. The major outliers attributed to the proposed model are slightly fewer than those attributed to the Choi's and B&G's models. Those outliers are also more evenly distributed outside both the ±20%

error bands. The outliers associated with both Choi's and B&G's models are more densely distributed below the –20% error band, indicating a consistent underestimation of gas volume fraction.

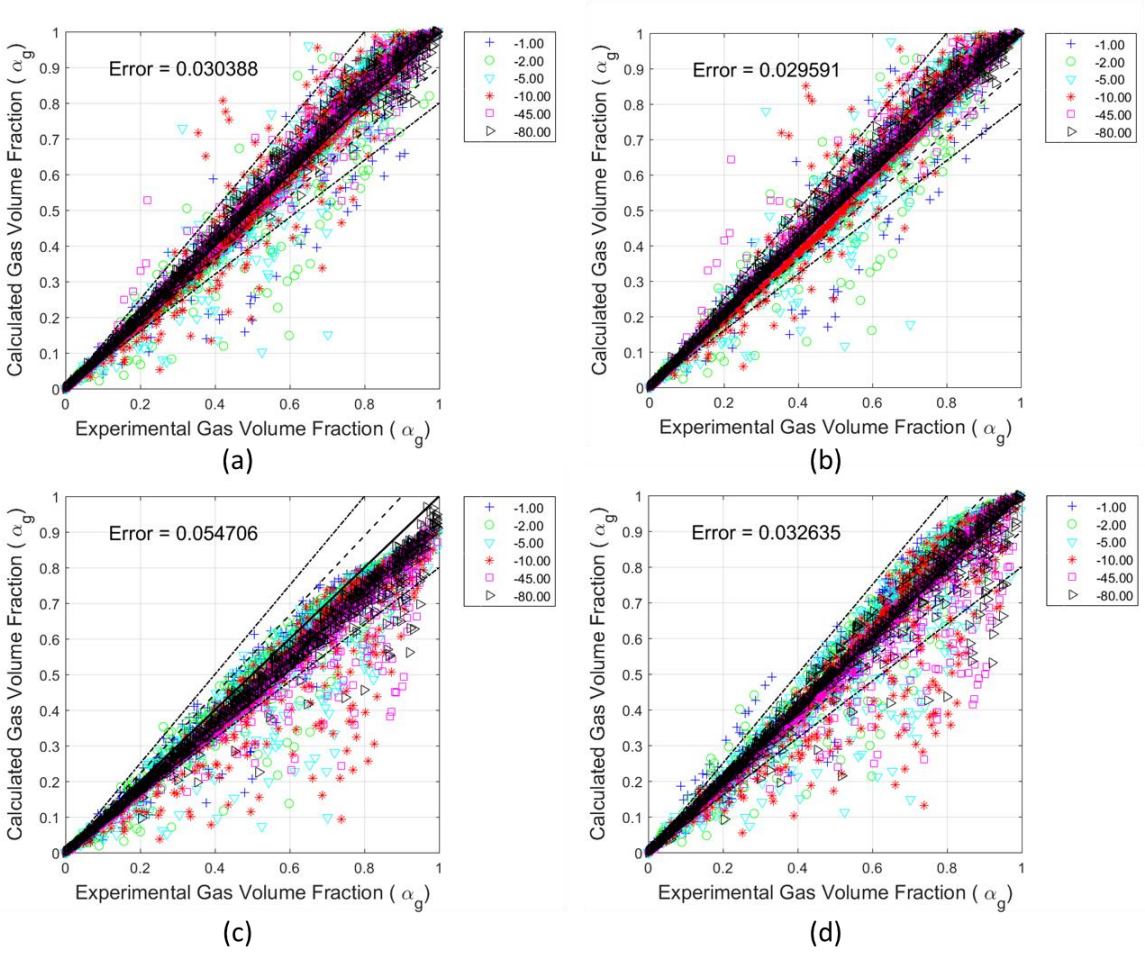

Figure 5.5–Cross-plots of model comparative performance for horizontal and upward flow: (a) the proposed model with X_{opt}^{TUF} parameter set, (b) the proposed model with X_{opt}^{OLG} parameter set, (c) the Choi's model and (d) the B&G's model against upward and horizontal pipe inclinations in the OLGAS dataset.

5.5 Application in GURU-MSW

We apply GURU-MSW to test the numerical stability of this newly developed drift-flux model. As we mentioned in section 2.3.1. The primary variables of the wellbore module in GURU-MSW are pressure, water holdup (α_w), mixture velocity, and molar density of each hydrocarbon component. Since pressure and molar density of each hydrocarbon component are implicitly correlated with density and viscosity, we take water holdup and mixture velocity as representative parameters to evaluate. We plot calculated drift velocity (v_d) over $0 \leq v_m \leq 50$ft/s and $0 \leq \alpha_w \leq 1$ for six inclinations: $\theta = 90°$, $\pm 10°$, 0°, -45° and -80° as shown in Figure 5.6 These plots illustrate the model continuity and smoothness over the entire solution space. At $\theta = -10°$, we observe a smooth transition of drift velocity from positive to negative as v_m decreases.

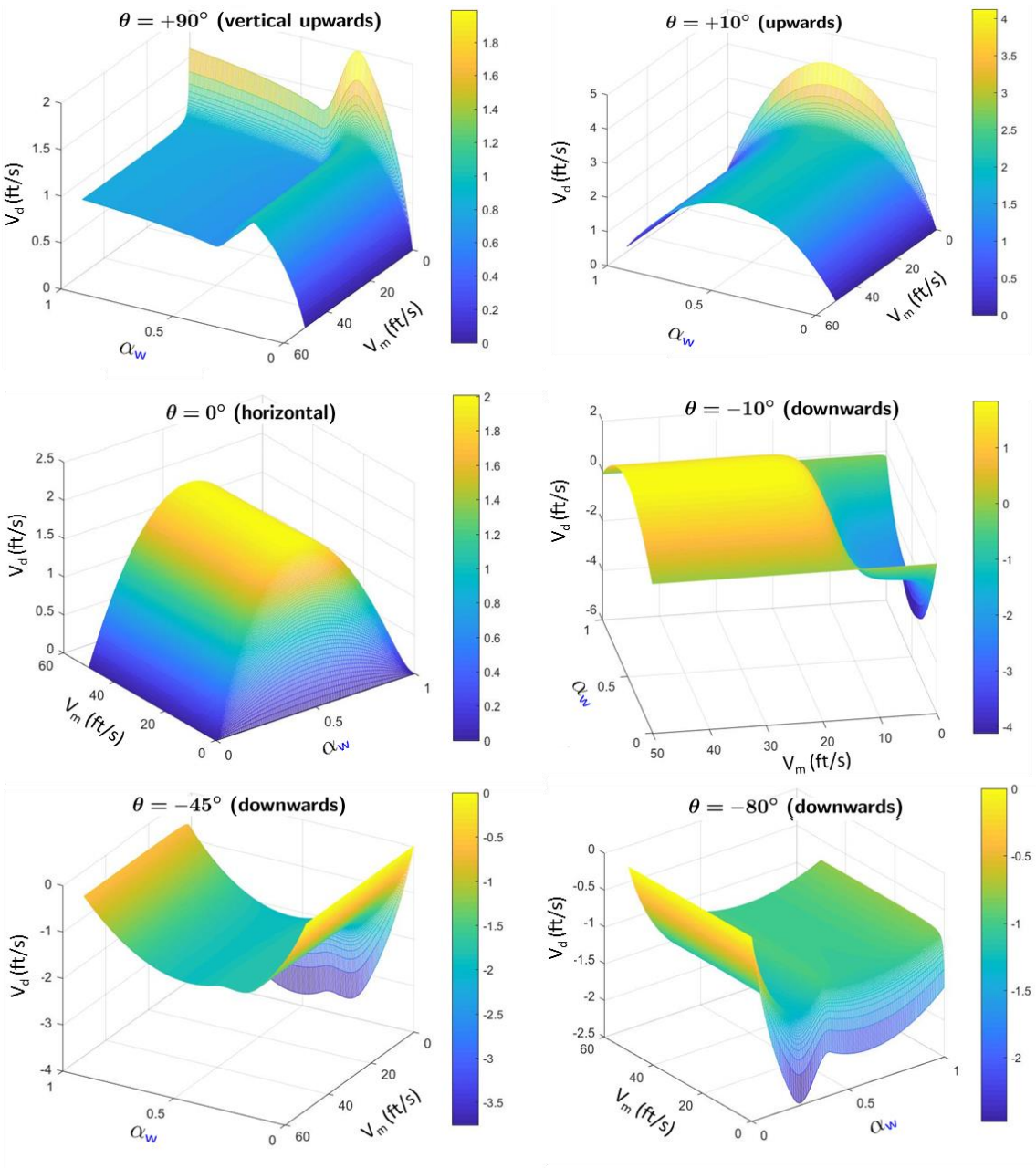

Figure 5.6–Numerical smoothness demonstration of drift velocity at six different pipe inclinations. Model test following X_{opt}^{OLG}.

To further test that the new model is compatible with mass and momentum conservations inside the coupled wellbore-reservoir simulator, we design four test cases with reservoir layout and wellbore trajectories shown in Figure 5.7. The reservoir model is shown on the top with the wellbore location shown in red. The dash line represents the flow influx region. The four wellbores specified possess inclinations of ±10°. The four well configurations are: toe-up, toe-down, undulating hump and undulating sump. The existing DF model (defined for +2 degrees to vertical) is, therefore, only applicable to the toe-down scenario.

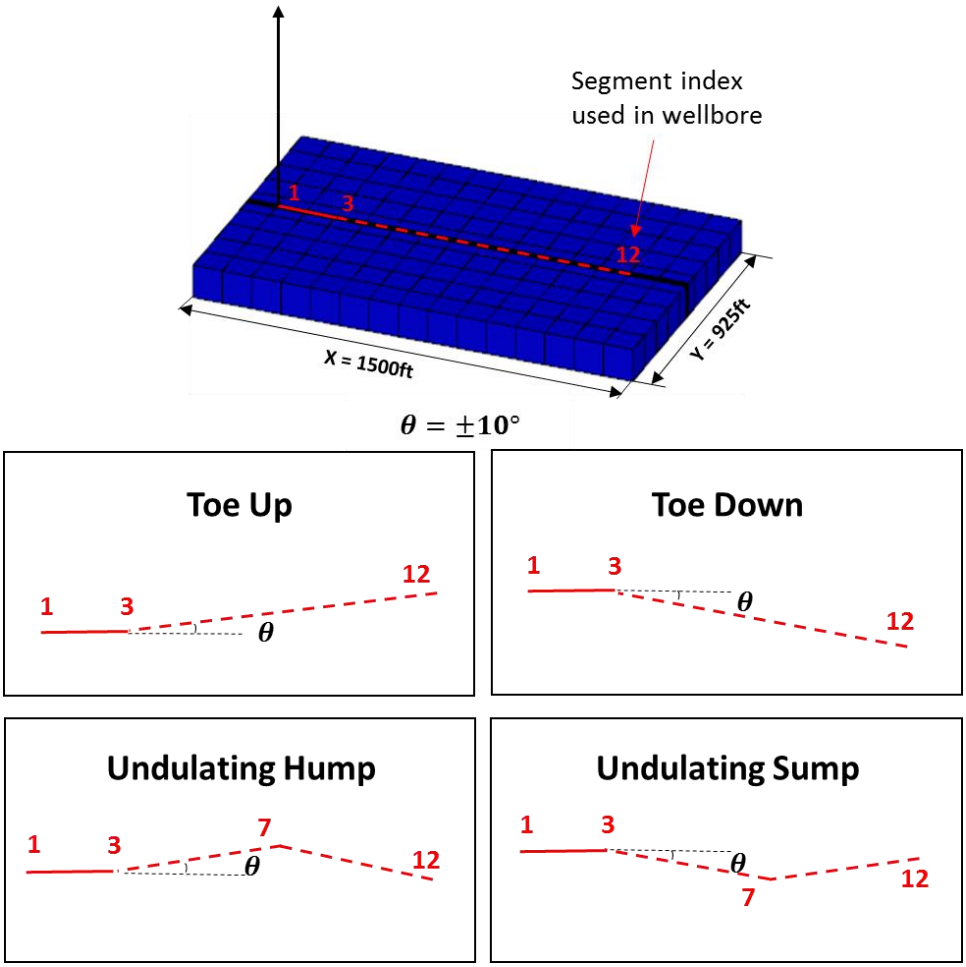

Figure 5.7–Sketch of the four well configurations assessed in the numerical testing with GURU-MSW.

Parameters of the simulation are shown in Table 5.5. There are three phases (gas, oil and water) presented in the simulation. We combine the oil and water phases into a "liquid" phase (slippage between oil and water is not considered).

Parameter	Value	Units
Reservoir properties		
Initial reservoir pressure	6000	psia
Initial water saturation	0.3	-
Reservoir temperature	200	F
Reservoir porosity	0.1	-
Reservoir permeability	1	mD
Rock compressibility	4×10^{-6}	psi^{-1}
Wellbore properties		
Wellbore diameter	0.3	ft
Wellbore relative roughness	0.0005	-
Well index (geometry)	0.7	bbl·cP/day/psi
Maximum oil produce rate	10000	STB/day
Minimum bottom hole pressure	1000	psia
Fluid properties		
Water viscosity	0.31	cP
Water compressibility	3×10^{-6}	psi^{-1}
Oil fluid composition	25.0 N2C1 35.0 C2C5 40.0 C6+	mol%

Table 5.5–Parameters applied in the testing case shown by Figure 5.7.

The predicted cumulative oil and gas production for all well configurations in a 1000-day window are shown in Figure 5.8 and Figure 5.9 respectively. The results first prove that the new drift-flux model is applicable in MSW-reservoir simulation for different well trajectories. The predicted cumulative production of all four well configurations are almost coincident, which is because of the same well index and inflow region length. If we zoom in the cumulative production for the last 100 days, we can find slight differences among different configurations. The following ranking can be obtained for both oil and gas production: toe down > undulating sump > undulating hump > toe up. This ranking mainly comes from different well inflow rates due to hydrostatic depth

corrections between completion depth and the center of grid blocks. In GURU-MSW, the correction is calculated from the saturation weighted fluid densities in the completion grid block.

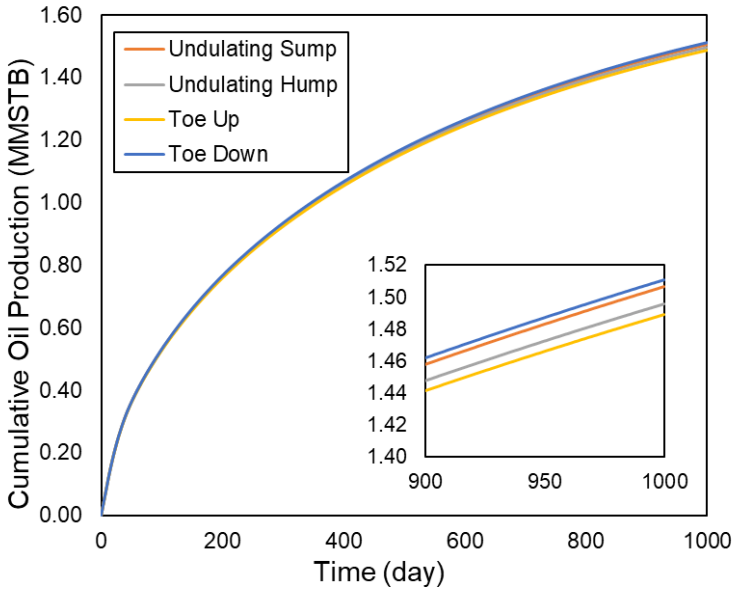

Figure 5.8–Predicted oil cumulative production for the four well configurations.

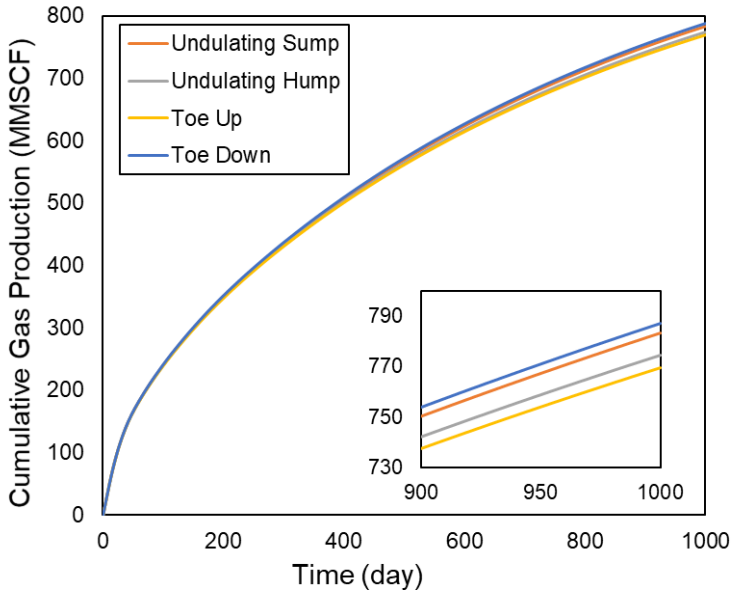

Figure 5.9–Predicted gas cumulative production for the four well configurations.

We also compare the cumulative oil and gas production of a horizontal wellbore predicted by the homogeneous model and the new drift-flux model, as shown in Figure 5.10. The reservoir setting and simulation parameters are the same as Figure 5.7 and Table 5.5. Comparing with the results predicted by the drift-flux model, the homogeneous model underpredicts the cumulative oil production for 16.2% and over predicts the cumulative gas production for 11.3%.

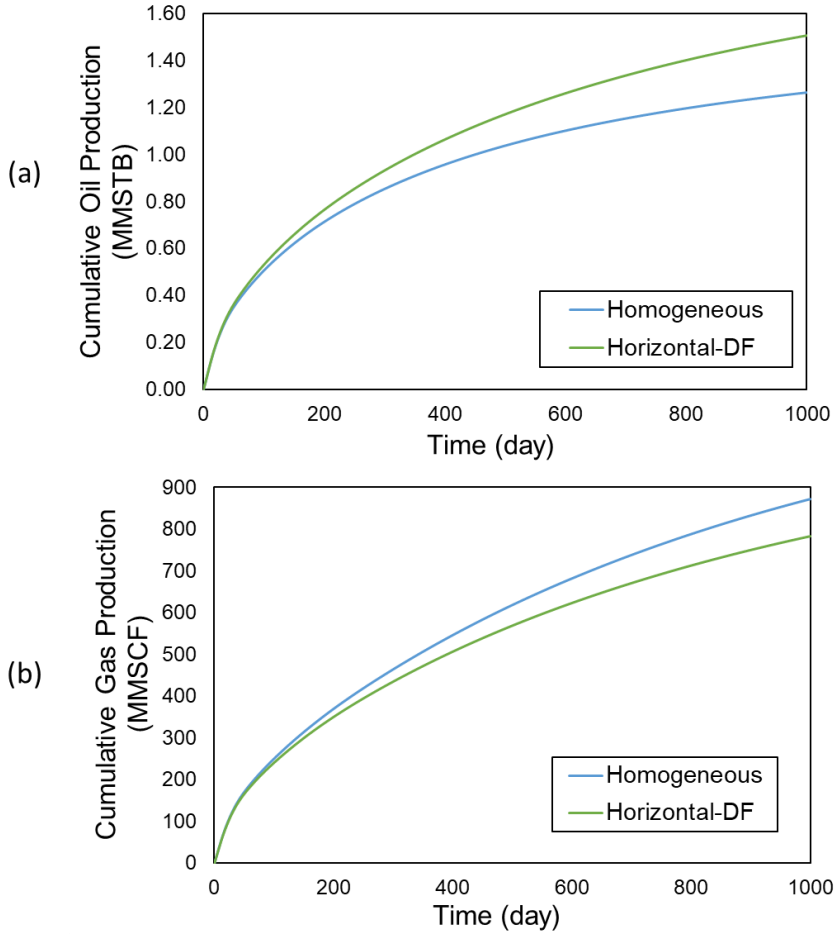

Figure 5.10–(a) Oil and (b) gas cumulative production predicted by the homogeneous model and the proposed drift-flux model for the horizontal wellbore configuration.

The differences are resulted from the different evolution of wellbore mole fractions predicted by the two models. Figure 5.11 presents the wellbore average mole fraction with time for the three pseudo-components. Figure 5.12 presents the average mole fraction of flow influx into wellbore. The results predicted by the proposed drift-flux model and the homogeneous model are compared in both figures. Although the two models predict the same flow influx mole fraction, the mole fraction inside the wellbore is much more

different because of the phase slippage consideration. During the 1000-day production window, the drift flux model predicts that the light component N_2C_1 increases from 0.25 to 0.3, the heavy component C_{6+} reduces from 0.4 to 0.3, and the mole fraction of the middle component remains almost unchanged. For the same production period, the homogeneous model predicts that the light component N_2C_1 increases from 0.25 to 0.45, the heavy component C_{6+} reduces from 0.4 to 0.2, and the mole fraction of the middle component also remains almost unchanged. Compared to the drift-flux model, the homogeneous model predicts more light components and fewer heavy components in the wellbore. This is mainly because of the no-slip assumption held by the homogeneous model, which can lead to large errors in production predictions.

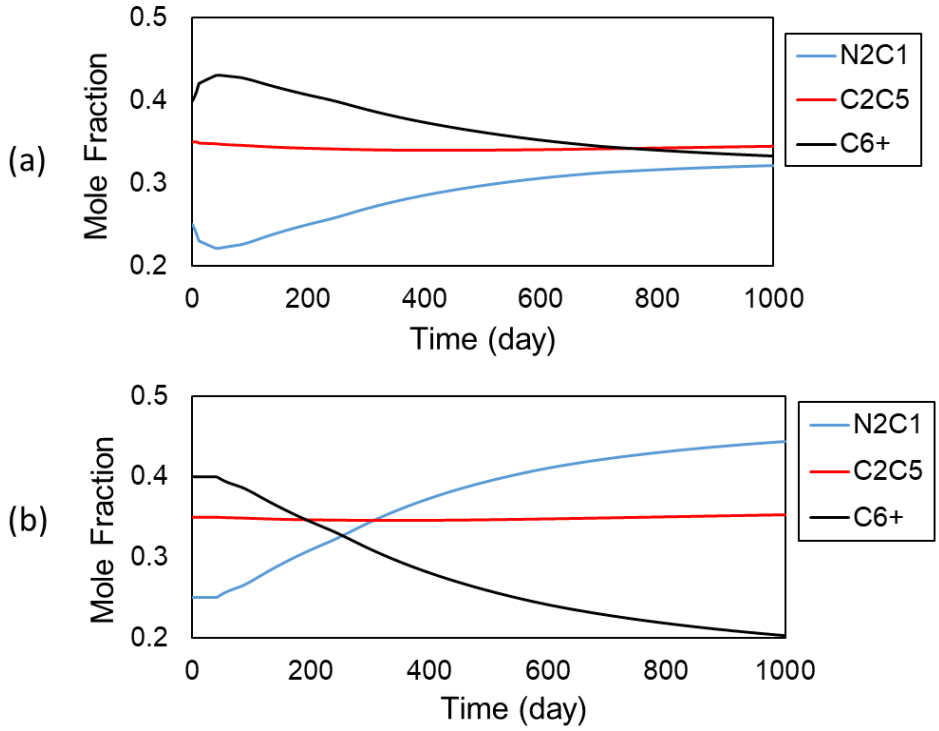

Figure 5.11–Average mole fraction in wellbore predicted by (a) the proposed drift-flux model and (b) the homogeneous model.

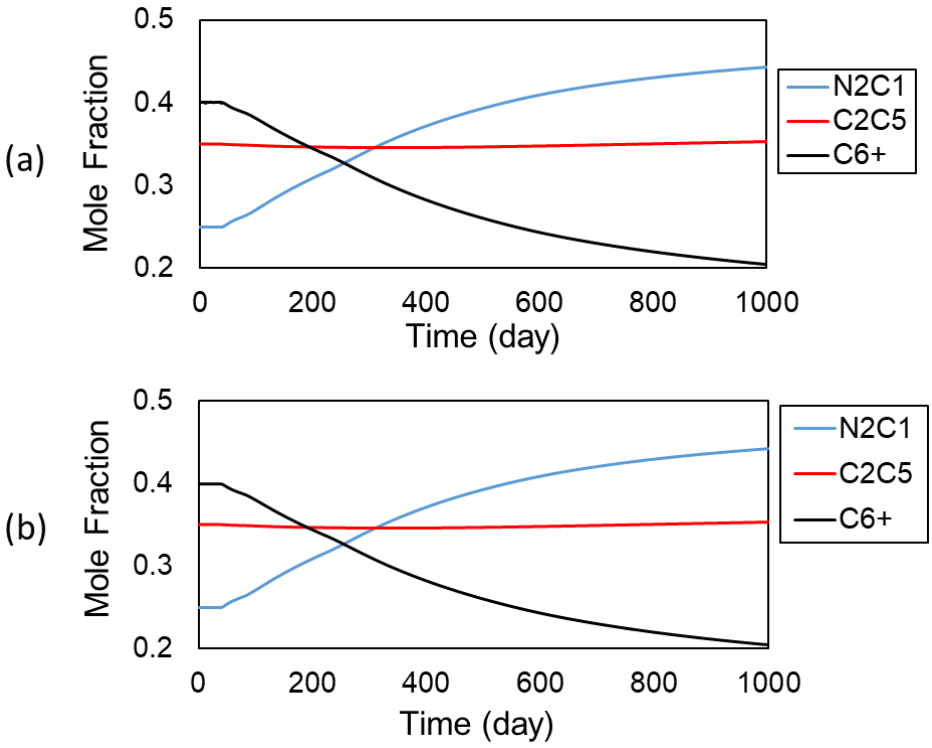

Figure 5.12–Average mole fraction of flow influx predicted by (a) the proposed drift-flux model and (b) the homogeneous model.

5.6 Discussion

5.6.1 Analysis on Upward and Downward Flow Behavior

To understand the differences associated with upward and downward pipe inclinations, we analyze the trend of OLGA-S data by plotting pipe inclinations with gas volume fraction for different gas input fractions (f_g). Figure 5.13 presents these plots at different mixture velocities. The pipe inclination range is $-80° \leq \theta \leq 90°$, and the gas input fraction range is $0.01 \leq f_g \leq 0.99$. Different marker color on the plot represents different flow regimes. It may be observed that pipe inclinations have significant effects on gas

volume fraction at low mixture velocity with low gas fractions. For $V_m = 1m/s$ and f_g = 0.99, the gas volume fraction of $\theta = -2°$ is 38% higher than that of $\theta = 0°$, and the gas volume fraction of $\theta = 2°$ is 26% lower than that of $\theta = 0°$. At this same mixture velocity ($V_m = 1m/s$), the value of gas volume fraction at $\theta = 0°$ is much closer to that observed at $\theta = 2°$ than to that at $\theta = -2°$ in the range of $0.3 \leq f_g \leq 0.9$. For example, the gas volume fraction of $f_g = 0.7$ at of $\theta = 2°, 0°, -2°$ are 0.363, 0.365 and 0.759 respectively. The gas volume fraction difference of upward and downward flow becomes much smaller as f_g becomes smaller and V_m becomes larger.

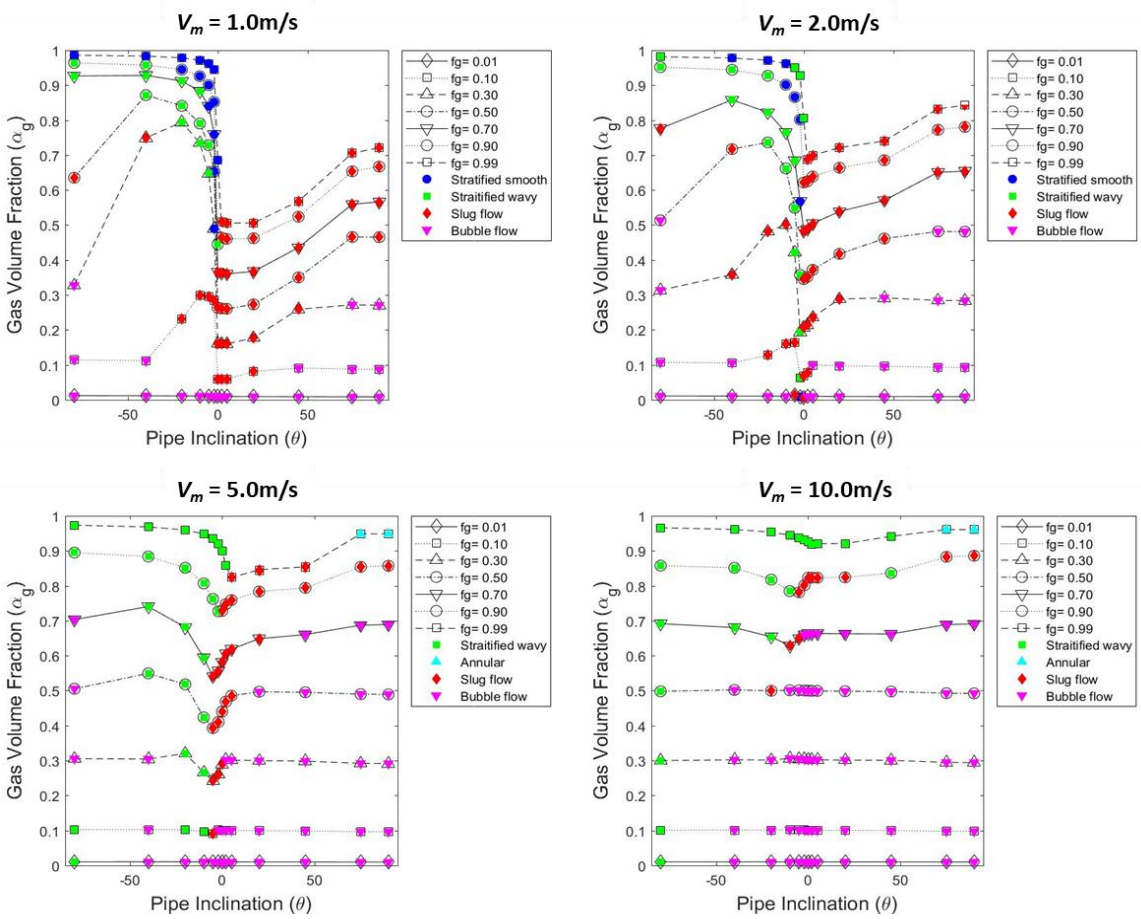

Figure 5.13–Plots of gas volume fraction (α_g) against inclination for various gas input fractions. Each plot exhibits OLGA-S data sampled based on the mixture velocity shown. Different color represents different flow regimes given by the OLGA-S library.

Ghajar and Bhagwat (2014) reported similar qualitative results to those observed in Figure 5.13 by analyzing experimental data over the range $-20° \leq \theta \leq 20°$ and $0.01 \leq f_g \leq 0.92$. They observed a significant decrease in gas volume fraction when inclination changed from –20° to +20° at low liquid and gas flow rates. They suggested that the reason for high gas volume fraction values was due to long "residence" time of the gas phase (in the test section) caused by the flow stratification at downward inclinations. The OLGA-S

library predicts stratified flow patterns for downward flow and slug flow for upward flow at these low flow rates – which is in keeping with these observations.

Figure 5.14 presents the gas volume fraction predictions for the proposed model, Choi's model and B&G's model. The figure compares model responses for two values of mixture velocity, namely: v_m = 1m/s and 5m/s. For v_m = 1m/s, the proposed model characterizes gas volume fraction at the horizontal transition reasonably well (*i.e.*, the regions between upward and downward flow). Choi's model (middle) is unable to capture this trend, while B&G's model is only partially successful (not predict well when $f_g \geq 0.9$). On the other hand, the proposed model does appear to resemble OLGA-S data trend over the whole range of input gas fractions.

For v_m = 5m/s, we observe that gas volume fraction behave almost linearly with respect to f_g. The effect of pipe inclination on gas volume fraction also appears less significant. Only the proposed model captures the modest impact of inclination on gas volume fraction. Conversely, predictions from Choi and B&G appear to be almost independent of inclinations. In the region of high gas fractions, *i.e.*, $f_g \geq 0.7$, the proposed model and also B&G's model tend to over predict gas volume fraction, while Choi's model tends to under predict this quantity. This is consistent with the observations shown earlier (Figure 5.4).

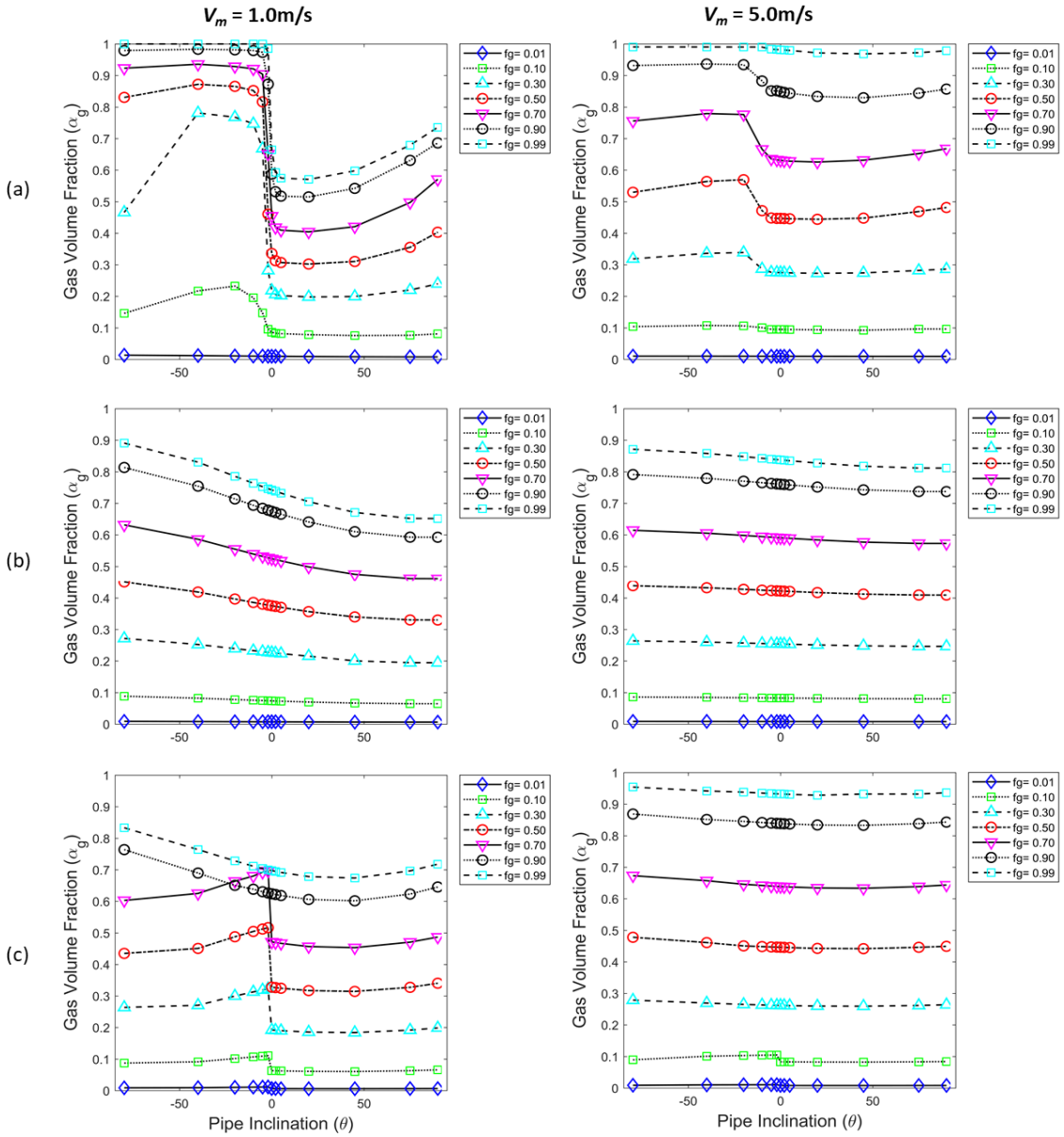

Figure 5.14–Predictions of gas volume fraction of (a) the proposed model, (b) the Choi's model, and (c) the B&G's model for V_m equals to 1 and 5m/s.

The utility of having a parameter set tuned to OLGA-S data allows engineers to construct a fully unified flow model from sandface-to-facilities. This means a completely

unified flow model throughout which has benefits for inversion and consistency as there is now a single harmonious model describing the multiphase flow in all conduits. In addition, applying a profile parameter equals to one can guarantee hyperbolicity of the transient drift flux modeling in a standalone wellbore or pipeline simulator (Eghorieta et al., 2018). This has implications in gas kick modeling and detection for drilling operations (Tang et al., 2019; Xu et al., 2018).

5.6.2 Model Limitations

Although the proposed model successfully resembles the gas volume fraction trends exhibited by OLGA-S, it still suffers from some inaccuracy predictions for $v_m \lesssim 2$m/s. This is particularly visible over the mid-range of gas input fractions, namely: $0.3 \leq f_g \leq 0.7$. In general, the stratified flow behavior observed at low mixture velocity and slightly-downward flow cause difficulties to all drift-flux models. It is non-trivial to derive a simple correlation to predict these dramatic changes in gas volume fraction at the transition.

Subsequent to reported observations by Ghajar and Bhagwat (2014), a revised correlation to better model behavior at the transition between stratified and non-stratified flow in downward flow was proposed by Bhagwat and Ghajar (2015). This correlation is more complex than their previous model where the transition criterion involved a superficial gas velocity Froude number such that $Fr_{sg} \leq 0.1$.

Several researchers have suggested a larger profile parameter ($C_o \simeq 2$) for gas-liquid flow with high liquid viscosity (Choi et al., 2012; Ghajar and Bhagwat, 2014;

Gokcal, 2008). To avoid potential numerical difficulties in coupled wellbore-reservoir simulation, the proposed model only allows the profile parameter change in the range $1 \leq C_0 \leq 1.2$. The optimized parameter set based on the TUFFP dataset has a profile parameter range of $1 \leq C_0 \leq 1.088$. The optimized parameter set based on the OLGA-S dataset has a constant profile parameter of 1. Therefore, we only suggest the application of the proposed model in low and medium liquid viscosity range ($\mu_l \lesssim 70$cP).

5.7 Conclusions

In this chapter, we proposed a new unified gas-liquid drift-flux model suitable for all pipe inclinations. The model has parameters optimized through data from the TUFFP and the OLGA-S library. The model was compared against two state-of-the-art drift-flux models and proved to have comparable, or better, performance. The primary conclusions from the study are as follows:

(1) Gas-liquid two phase flow becomes stratified at low mixture velocities ($\lesssim$2m/s) for slightly downward pipe inclinations, which is difficult for any drift-flux model to represent. The proposed model furnishes acceptable results for this flow regime.

(2) Gas volume fraction increases sharply at the transition of horizontal-upward to horizontal-downward at low mixture velocities. The proposed model can represent this trend reasonably well.

(3) The model is proved to be numerically stable in GURU-MSW over four testing well configurations.

(4) In a compositional test case, the homogeneous model predicted 16.2% less oil production and 11.3% more gas production than the proposed drift-flux model.

6. CONCLUSIONS AND FUTURE WORK

6.1 Conclusions

In this work, we develop a general simulation framework for coupled wellbore reservoir simulation (GURU-MSW) based on a general-purpose compositional reservoir simulator (GURU). In GURU-MSW, the wellbore module and the reservoir module are at the same level and fully implicitly coupled. Although taking the most developing effort, the fully implicit mechanism is unconditionally stable and faster than those iteratively or loosely coupling mechanisms. With a flexible segment connection list embedded, GURU-MSW can handle complex wellbore structures and well group modeling.

GURU-MSW is applied in the analysis of two production scenarios: one is well interference in shale reservoir development, and the other is gas well liquid loading phenomenon. Both applications start with verification of GURU-MSW against relevant cases in ECLIPSE 300. Those verification and application cases help with debugging GURU-MSW comprehensively. For example, the well interference application tests GURU-MSW in wellbore cross flow modeling, and it also demonstrates GURU-MSW's capability in handling multiple wells under group control strategy.

On the other hand, we make valuable efforts in extending the application range of coupled wellbore-reservoir simulation. Applying an MSW-reservoir simulator for well interference and liquid loading modeling are both first attempts in the literature. The liquid loading application is a big improvement based on the current literature. The dynamic nature of liquid loading phenomenon cannot be comprehensively modeled through either

a single reservoir simulator or a single wellbore simulator. The analysis with GURU-MSW allows us to observe some interesting phenomena that have never been studied. The natural cyclical production observation can serve as the best illustration.

We also make significant contributions in gas-liquid drift-flux modeling within coupled wellbore-reservoir simulation. Two novel drift-flux models are proposed in this work. One drift-flux model is specially designed for application in liquid loading analysis. The model considers the transition criteria from annular to churn/slug flow, which governs the onset of liquid loading. Applicable to pipe inclinations from 0° (horizontal) to 90° (vertical upward), the model is incorporated into GURU-MSW for liquid loading analysis in horizontal wellbore.

The other is a unified drift-flux model applicable to whole pipe inclination range from -90° to 90°. Some previously reported drift-flux models have the same application range, however none of them are applicable to a coupled wellbore-reservoir simulator. Being tested in GURU-MSW, the new model demonstrates its potential in filling in the gap left by the existing drift flux model in MSW modeling (horizontal and downward flow).

6.2 Future Work

We would like to give the following recommendations for future work associated with GURU-MSW:

(1) Incorporate the models of inflow control device (ICD) and inflow control valves (ICV) to extend the capability of GURU-MSW in smart well modeling.

(2) Extend the capability of GURU-MSW in multi-level well group modeling. This should start with developing an advanced algorithm for active well constraint determination (Watts et al. 2012).

(3) Improve the computation efficiency of GURU-MSW by designing more advanced data structure and novel preconditioners for linear solver.

(4) Incorporate the phase behavior of asphaltene and wax to extend the application of GURU-MSW in flow assurance analysis.

(5) Develop new oil-water drift-flux models (applicable to whole pipe inclinations) for application in coupled wellbore-reservoir simulation.

REFERENCES

Aarsnes, U.J.F., 2016. Modeling of two-phase flow for estimation and control of drilling operations. Ph.D. dissertation, Norwegian University of Science and Technology

Aarsnes, U.J.F., Ambrus, A., Di Meglio, F., Vajargah, A.K., Aamo, O.M., van Oort, E., 2016. A simplified two-phase flow model using a quasi-equilibrium momentum balance. Int. J. Multiph. Flow 83, 77–85.

Abdul-Majeed, G.H., 2000. Liquid slug holdup in horizontal and slightly inclined two-phase slug flow. J. Pet. Sci. Eng. 27, 27–32.

Afsharpoor, A., Javadpour, F., 2016. Liquid slip flow in a network of shale noncircular nanopores. Fuel 180, 580–590.

Ajani, A.A., Kelkar, M.G., 2012. Interference study in shale plays, in: SPE Hydraulic Fracturing Technology Conference.

Akpan, I.B., 1980. Two-phase metering. Master's thesis, The University of Tulsa.

Alamu, M.B., 2012. Gas-well liquid loading probed with advanced instrumentation. SPE J. 17, 251–270.

Alsaadi, Y., 2013. Liquid Loading in Highly Deviated Gas Wells. Ph.D. dissertation, The University of Tulsa.

Alsaadi, Y., Pereyra, E., Torres, C., Sarica, C., 2015. Liquid loading of highly deviated gas wells from 60 to 88, in: SPE Annual Technical Conference and Exhibition.

Ansari, A., Fathi, E., Belyadi, F., Takbiri-Borujeni, A., Belyadi, H., 2018. Data-Based Smart Model for Real Time Liquid Loading Diagnostics in Marcellus Shale via Machine Learning, in: SPE Canada Unconventional Resources Conference.

Awada, A., Santo, M., Lougheed, D., Xu, D., Virues, C., 2016. Is That Interference? A Work Flow for Identifying and Analyzing Communication Through Hydraulic Fractures in a Multiwell Pad. SPE J. 21, 1–554.

Bahonar, M., Azaiez, J., Chen, Z.J., 2011. Transient nonisothermal fully coupled wellbore/reservoir model for gas-well testing, part 1: Modelling. J. Can. Pet. Technol. 50, 37–50.

Beggs, D.H., Brill, J.P., 1973. A study of two-phase flow in inclined pipes. J. Pet. Technol. 25, 607–617.

Beggs, H.D., 1973. An experimental study of two-phase flow in inclined pipes. Ph.D. dissertation, The University of Tulsa.

Belfroid, S., Schiferli, W., Alberts, G., Veeken, C.A.M., Biezen, E., 2008. Predicting onset and dynamic behaviour of liquid loading gas wells, in: SPE Annual Technical Conference and Exhibition.

Ben-Mansour, R., Al-sarkhi, A., Sharma, A.K., Jeyachandra, B.C., Sarica, C., Gokcal, B., 2010. Effect of pipe diameter and high oil viscosity on drift velocity for horizontal pipes, in: 7th North American Conference on Multiphase Technology.

Bendiksen, K.H., 1984. An experimental investigation of the motion of long bubbles in inclined tubes. Int. J. Multiph. Fow 10, 467–483.

Bendiksen, K.H., Maines, D., Moe, R., Nuland, S., 1991. The dynamic two-fluid model OLGA: Theory and application. SPE Prod. Eng. 6, 171–180.

Bhagwat, S.M., Ghajar, A.J., 2015. An Empirical Model to Predict the Transition Between Stratified and Nonstratified Gas--Liquid Two-Phase Flow in Horizontal

and Downward Inclined Pipes. Heat Transf. Eng. 36, 1485–1494.

Bhagwat, S.M., Ghajar, A.J., 2014. A flow pattern independent drift flux model based void fraction correlation for a wide range of gas--liquid two phase flow. Int. J. Multiph. Flow 59, 186–205.

Bhagwat, S.M., Ghajar, A.J., 2012. Similarities and differences in the flow patterns and void fraction in vertical upward and downward two phase flow. Exp. Therm. Fluid Sci. 39, 213–227.

Brill, J.P., Chen, X.T., Flores, J.G., Marcano, R., 1996. Transportation of Liquids in Multiphase Pipelines Under Low Liquid Loading Conditions. TUFFP report, The University of Tulsa.

Brito, R., 2012. Effect of Medium Oil Viscosity on Two-Phase Oil-Gas Flow Behavior in Horizontal Pipes. M.S. Thesis, The University of Tulsa.

Brito, R.M., 2015. Effect of horizontal well trajectory on two-phase gas-liquid flow behavior. The University of Tulsa.

Caetano, E.F., 1986. Upward vertical two-phase flow through an annulus. Ph.D. dissertation, The University of Tulsa.

Cao, H., 2002. Development of techniques for general purpose simulators. Stanford University.

Cao, H., Samier, P., Kalunga, H.M., Detige, E., Obi, E., 2015. A Fully Coupled Network Model, Practical Issues and Comprehensive Comparison with Other Integrated Models on Field Cases, in: SPE Reservoir Simulation Symposium. https://doi.org/10.2118/173251-MS

Chai, Z., Yan, B., Killough, J.E., Wang, Y., 2018. An efficient method for fractured shale reservoir history matching: The embedded discrete fracture multi-continuum approach. J. Pet. Sci. Eng. 160, 170–181. https://doi.org/10.1016/j.petrol.2017.10.055

Cheremisinoff, N.P., 1977. Experimental and theoretical investigation of horizontal stratified and annular two phase flow with heat transfer. Clarkson Coll. of Tech., Potsdam, NY.

Choi, J., Pereyra, E., Sarica, C., Lee, H., Jang, I.S., Kang, J., 2013. Development of a fast transient simulator for gas--liquid two-phase flow in pipes. J. Pet. Sci. Eng. 102, 27–35.

Choi, J., Pereyra, E., Sarica, C., Park, C., Kang, J.M., 2012. An efficient drift-flux closure relationship to estimate liquid holdups of gas-liquid two-phase flow in pipes. Energies 5, 5294–5306.

Coats, B.K., Fleming, G.C., Watts, J.W., Rame, M., Shiralkar, G.S., others, 2004. A generalized wellbore and surface facility model, fully coupled to a reservoir simulator. SPE Reserv. Eval. Eng. 7, 132–142.

da Silva, D.V.A., Jansen, J.D., 2015. A Review of Coupled Dynamic Well-Reservoir Simulation∗. IFAC-PapersOnLine 48, 236–241.

Dousi, N., Veeken, C.A.M., Currie, P.K., 2006. Numerical and Analytical Modelling of the Gas Well Liquid Loading Process. SPE Prod. Oper. 21, 475–482.

Eaton, B., 1965. The Prediction of Flow Patterns, Liquid Holdup and Pressure Losses Occurring During Continuous Two-Phase Flow in Horizontal Pipes. Ph.D.

dissertation, University of Tulsa.

Economides, M.J., Hill, A.D., Ehlig-Economides, C., 2012. Petroleum production systems. Pearson Education.

Eghorieta, R.A., Afolabi, T.A., Panacharoensawad, E., 2018. Drift flux modeling of transient high-viscosity-liquid and gas two-phase flow in horizontal pipes. J. Pet. Sci. Eng. 171, 605–617.

El Fadili, Y., Shah, S., 2017. A new model for predicting critical gas rate in horizontal and deviated wells. J. Pet. Sci. Eng. 150, 154–161.

Energy Information Agency, 2010. Eagle Ford Shale Play, Western Gulf Basin, South Texas [WWW Document]. URL http://www.eia.gov/oil_gas/rpd/shaleusa9.pdf. (accessed 9.21.17).

Faille, I., Heintzé, E., 1999. A rough finite volume scheme for modeling two-phase flow in a pipeline. Comput. Fluids 28, 213–241.

Fan, Y., 2005. An Investigation of Low Liquid Loading Gas- Liquid Stratified Flow in Near-Horizontal Pipes. Ph.D. dissertation, The University of Tulsa.

Felizola, H., 1992. Slug flow in extended reach directional wells. Master's thesis, The University of Tulsa.

Fjar, E., Holt, R.M., Raaen, A.M., Risnes, R., Horsrud, P., 2008. Petroleum related rock mechanics. Elsevier.

Ghajar, A.J., Bhagwat, S.M., 2014. Gas-liquid two phase flow phenomenon in near horizontal upward and downward inclined pipe orientations. Int. J. Mech. Aerospace, Ind. Mechatronics Eng. 8, 1039–1053.

Gokcal, B., 2008. An experimental and theoretical investigation of slug flow for high oil viscosity in horizontal pipes. Ph.D Disseration, The University of Tulsa.

Guner, M., 2012. Liquid Loading of Gas Wells with Deviations from 0 to 45. Ph.D. Dissertation, The University of Tulsa.

Guner, M., Pereyra, E., Sarica, C., Torres, C., others, 2015. An Experimental Study of Low Liquid Loading in Inclined Pipes from 90 to 45, in: SPE Production and Operations Symposium.

Guyaguler, B., Zapata, V.J., Cao, H., Stamati, H.F., Holmes, J.A., 2011. Near-well-subdomain simulations for accurate inflow-performance-relationship calculation to improve stability of reservoir/network coupling. SPE Reserv. Eval. Eng. 14, 634–643.

Hasan, A.R., Kabir, C.S., Sayarpour, M., 2010. Simplified two-phase flow modeling in wellbores. J. Pet. Sci. Eng. 72, 42–49.

Hentz, T.F., Ruppel, S.C., 2010. Regional lithostratigraphy of the Eagle Ford Shale: Maverick Basin to East Texas Basin. Gulf Coast Assoc. Geol. Soc. Trans. 60, 325–337.

Holmes, J.A., 1983. Enhancements to the strongly coupled, fully implicit well model: wellbore crossflow modeling and collective well control, in: SPE Reservoir Simulation Symposium.

Holmes, J.A., 1977. Description of the drift flux model in the LOCA codes RELAPUK, in: Heat and Fluid Flow in Water Reactor Safety. Conference Sponsored by the Thermodynamics and Fluid Mechanics Group of the Institution of Mechanical

Engineers, Manchester, 13-15 September 1977.

Hovorka, S.D., 1998. Facies and diagenesis of the Austin Chalk and controls on fracture intensity — a case study from North Central Texas. Univ. Texas Austin, Bur. Econ. Geol. Geol. Circ. 98, 47.

Isao, K., Mamoru, I., 1987. Drift flux model for large diameter pipe and new correlation for pool void fraction. Int. J. Heat Mass Transf. 30, 1927–1939.

Jackson, D.F.B., Virues, C.J.J., Sask, D., 2011. Investigation of Liquid Loading in Tight Gas Horizontal Wells With a Transient Multiphase Flow Simulator, in: Canadian Unconventional Resources Conference.

Jeyachandra, B.C., Gokcal, B., Al-Sarkhi, A., Sarica, C., Sharma, A., 2012. Drift-velocity closure relationships for slug two-phase high-viscosity oil flow in pipes. SPE J. 17, 593–601. https://doi.org/SPE-151616-PA.

Jiang, J., Younis, R.M., 2017. An improved projection-based embedded discrete fracture model (pEDFM) for multiphase flow in fractured reservoirs. Adv. Water Resour. 109, 267–289. https://doi.org/10.1016/j.advwatres.2017.09.017

Jiang, Y., 2008. Techniques for modeling complex reservoirs and advanced wells. Ph.D. dissertation, Stanford University.

Johnson, G.W., 2005. A Study of Gas-Liquid Pipe Flow. Ph.D. dissertation, University of Oslo.

Kou, R., Alafnan, S.F.K., Akkutlu, I.Y., 2017. Multi-scale analysis of gas transport mechanisms in kerogen. Transp. Porous Media 116, 493–519.

Kouba, G., 1986. Horizontal Slug Flow Modeling and Metering. Ph.D. dissertation, The

University of Tulsa.

Kurtoglu, B., Salman, A., 2015. How to Utilize Hydraulic Fracture Interference to Improve Unconventional Development, in: Abu Dhabi International Petroleum Exhibition and Conference.

Landman, M.J., 1991. Non-unique holdup and pressure drop in two-phase stratified inclined pipe flow. Int. J. Multiph. flow 17, 377–394.

Lea, J.F., Nickens, H. V, 2004. Solving gas-well liquid-loading problems. J. Pet. Technol. 56, 30–36.

Limpasurat, A., Valko, P.P., Falcone, G., 2015. A New Concept of Wellbore-Boundary Condition for Modeling Liquid Loading in Gas Wells. SPE J. 20, 550–564.

Livescu, S., Durlofsky, L.J., Aziz, K., Ginestra, J.C., 2010. A fully-coupled thermal multiphase wellbore flow model for use in reservoir simulation. J. Pet. Sci. Eng. 71, 138–146.

Magrini, K.L., 2009. Liquid Entrainment in Annular Gas-Liquid Flow in Inclined Pipes. Master's thesis, The University of Tulsa.

Magrini, K.L., Sarica, C., Al-Sarkhi, A., Zhang, H.-Q., 2012. Liquid entrainment in annular gas/liquid flow in inclined pipes. SPE J. 17, 617–630.

Marino, M., Schiferli, W., Veeken, C.A.M., Smith, J., 2017. Shifting Turner's Paradigm: Gas Wells Can Produce in Slug Flow, in: SPE Annual Technical Conference and Exhibition.

Marongiu-Porcu, M., Lee, D., Shan, D., Morales, A., 2016. Advanced Modeling of Interwell-Fracturing Interference: An Eagle Ford Shale-Oil Study. SPE J. 21, 1567–

1582.

Martin, R., Baihly, J.D., Malpani, R., Lindsay, G.J., Atwood, W.K., 2011. Understanding Production from Eagle Ford-Austin Chalk System, in: SPE Annual Technical Conference and Exhibition. Society of Petroleum Engineers.

Masella, J.M., Tran, Q.H., Ferre, D., Pauchon, C., 1998. Transient simulation of two-phase flows in pipes. Int. J. Multiph. Flow 24, 739–755.

Meng, W., 1999. Low liquid loading gas-liquid two-phase flow in near-horizontal pipes. Ph.D. dissertation, The University of Tulsa.

Minami, K., 1983. Liquid Holdup in Wet-Gas Pipelines. Master's thesis, The University of Tulsa.

Moinfar, A., 2013. Development of an efficient embedded discrete fracture model for 3Dcompositional reservoir simulation in fractured reservoirs. Ph.D. dissertation, The University of Texas at Austin.

Mukherjee, H., 1980. An Experimental Study of Inclined Two-Phase Flow. Ph.D. dissertation, The University of Tulsa.

Nemoto, R.H., Baliño, J.L., Burr, K.P., 2009. Characteristic values and compatibility conditions for the no-pressure-wave model applied to petroleum systems, in: Proceeding of the 20th International Congress of Mechanical Engineering, Gramado, RS, Brazil.

Nennie, E.D., Alberts, G.J.N., Belfroid, S.P.C., Peters, E., Joosten, G.J.P., 2007. An investigation into the need of a dynamic coupled well-reservoir simulator, in: SPE Annual Technical Conference and Exhibition.

Nojabaei, B., Johns, R.T., Chu, L., 2013. Effect of capillary pressure on phase behavior in tight rocks and shales. SPE Reserv. Eval. Eng. 16, 281–289.

Oddie, G., Shi, H., Durlofsky, L.J., Aziz, K., Pfeffer, B., Holmes, J.A., 2003. Experimental study of two and three phase flows in large diameter inclined pipes. Int. J. Multiph. Flow 29, 527–558.

Okeahialam, I., Yang, M., Shinde, D.B., Sahai, V., Araque-Martinez, A., Rai, R., 2017. Completion Optimization Under Constraints: An Eagle Ford Shale Case Study. SPE Prod. Oper. 32, 128–136.

Pan, L., 2011. T2Well/ECO2N version 1.0: multiphase and non-isothermal model for coupled wellbore-reservoir flow of carbon dioxide and variable salinity water.

Pan, L., Oldenburg, C.M., 2014. T2Well—an integrated wellbore--reservoir simulator. Comput. Geosci. 65, 46–55.

Pan, L., Webb, S.W., Oldenburg, C.M., 2011. Analytical solution for two-phase flow in a wellbore using the drift-flux model. Adv. Water Resour. 34, 1656–1665.

Pauchon, C., Dhulesia, H., Lopez, D., Fabre, J., 1993. TACITE: a comprehensive mechanistic model for two-phase flow, in: BHRG Conference on Multiphase Production.

Pauchon, C.L., Dhulesia, H., 1994. TACITE: A transient tool for multiphase pipeline and well simulation, in: SPE Annual Technical Conference and Exhibition.

Peaceman, D.W., 1978. Interpretation of well-block pressures in numerical reservoir simulation. SPE J. 18, 183–194.

Pearson, K., 2010. Geologic Controls on Austin Chalk Oil and Gas Production:

Understanding a Dual Conventional-Continuous Accumulation. Gulf Coast Assoc. Geol. Soc. Trans. 60, 557–570.

Peng, D.-Y., Robinson, D.B., 1976. A new two-constant equation of state. Ind. Eng. Chem. Fundam. 15, 59–64.

Press, W.H., Flannery, B.P., Teukolsky, S.A., Vetterling, W.T., 1992. Numerical recipes in C: The Art of Scientific Computing, vol. 1.

Prosperetti, A., Tryggvason, G., 2009. Computational methods for multiphase flow. Cambridge University Press.

Rachford Jr, H.H., Rice, J.D., 1952. Procedure for use of electronic digital computers in calculating flash vaporization hydrocarbon equilibrium. J. Pet. Technol. 4, 13–19.

Redick, B.S., 2017. PID Controlled Adaptive Time-Stepping in Coupled Surface-Subsurface Simulation: A Tool for Reducing Non-Physical Oscillation. Ph.D. dissertation, Texas A&M University.

Richter, H.J., 1981. Flooding in tubes and annuli. Int. J. Multiph. Flow 7, 647–658.

Rothe, P.H., Crowley, C.J., Sam, R.G., 1986. Investigation of two-phase flow in horizontal pipes at large pipe size and high gas density. AGA Pipe Research Committee Project.

Roumazeilles, P., 1994. An Experimental Study of Downward Slug Flow in Inclined Pipes. Master's thesis, The University of Tulsa.

Santim, C.G. da S., Rosa, E.S., 2016. Roe-type Riemann solver for gas--liquid flows using drift-flux model with an approximate form of the Jacobian matrix. Int. J. Numer. Methods Fluids 80, 536–568.

Santim, C.G.S., Gaspari, E.F., Paternost, G.M., 2017. A transient analysis of gas-liquid slug flow inside a horizontal pipe using different models. J. Pet. Sci. Eng. 151, 62–76.

Schlumberger, 2017a. Eclipse Technical Description and Reference Manual.

Schlumberger, 2017b. PIPESIM Production System Analysis Software User Manual.

Schmidt, Ž., 1976. Experimental study of gas-liquid flow in a pipeline-riser pipe system. Master's thesis, The University of Tulsa.

Shi, H., Holmes, J.A., Durlofsky, L.J., Aziz, K., Diaz, L., Alkaya, B., Oddie, G., others, 2005. Drift-flux modeling of two-phase flow in wellbores. SPE J. 10, 24–33.

Shi, J., Sun, Z., Li, X., 2016. Analytical Models for Liquid Loading in Multifractured Horizontal Gas Wells. SPE J. 21, 471–487.

Shirdel, M., 2013. Development of a coupled wellbore-reservoir compositional simulator for damage prediction and remediation. Ph.D. dissertation, The University of Texas at Austin.

Siripatrachai, N., Ertekin, T., Johns, R.T., 2017. Compositional Simulation of Hydraulically Fractured Tight Formation Considering the Effect of Capillary Pressure on Phase Behavior. SPE J. 22, 1-046.

Stone, H.L., 1973. Estimation of three-phase relative permeability and residual oil data. J. Can. Pet. Technol. 12:4. https://doi.org/10.2118/73-04-06

Stone, T.W., Edmunds, N.R., Kristoff, B.J., others, 1989. A comprehensive wellbore/reservoir simulator, in: SPE Symposium on Reservoir Simulation.

Taitel, Y., Bornea, D., Dukler, A.E., 1980. Modelling flow pattern transitions for steady

upward gas-liquid flow in vertical tubes. AIChE J. 26, 345–354.

Taitel, Y., Dukler, A.E., 1976. A model for predicting flow regime transitions in horizontal and near horizontal gas-liquid flow. AIChE J. 22, 47–55.

Tan, X.-H., Huang, Y.-Z., Liu, J.-Y., You, X.-T., Wang, D.-J., Sun, Z.-Y., Yu, J., Tang, C., 2017. A New Design Method of Coiled Tubing for Deliquification in Shale Gas Field, in: SPE/ICoTA Coiled Tubing and Well Intervention Conference and Exhibition.

Tang, H., Chai, Z., Yan, B., Killough, J., 2017. Application of Multi-segment Well Modeling to Simulate Well Interference, in: Unconventional Resources Technology Conference (URTEC).

Tang, H., Hasan, A.R., Killough, J., 2018. Development and Application of a Fully Implicitly Coupled Wellbore/Reservoir Simulator To Characterize the Transient Liquid Loading in Horizontal Gas Wells. SPE J. https://doi.org/SPE-187354-PA.

Tang, H., Hasan, A.R., Killough, J., 2017. A Fully-Coupled Wellbore-Reservoir Model for Transient Liquid Loading in Horizontal Gas Wells, in: SPE Annual Technical Conference and Exhibition. https://doi.org/SPE-187354-MS.

Tang, H., Zhang, S., Zhang, F., Venugopal, S., 2019. Time series data analysis for automatic flow influx detection during drilling. J. Pet. Sci. Eng. 172, 1103–1111. https://doi.org/10.1016/j.petrol.2018.09.018

Tunstall, T., 2015. Iterative Bass Model forecasts for unconventional oil production in the Eagle Ford Shale. Energy 93, 580–588.

Valbuena Olivares, E., 2015. Production Performance Modeling Through Integration of

Reservoir and Production Network with Asphaltene Deposition. Ph.D. dissertation, Texas A&M University.

Vongvuthipornchai, S., 1982. Experimental study of pressure wave propagation in two-phase mixtures. Ph.D. dissertation, University of Tulsa.

Wallis, G.B., 1969. One-dimensional two-phase flow. New York, McGraw-Hill.

Walls, J.D., Sinclair, S.W., 2011. Eagle Ford shale reservoir properties from digital rock physics. First Break 29, 97–101.

Wang, Z., Fu, X., Guo, P., Tu, H., Wang, H., Zhong, S., 2015. Gas--liquid flowing process in a horizontal well with premature liquid loading. J. Nat. Gas Sci. Eng. 25, 207–214.

Wang, Z., Guo, L., Zhu, S., Nydal, O.J., 2018. Prediction of the Critical Gas Velocity of Liquid Unloading in a Horizontal Gas Well. SPE J. 23, 328–245. https://doi.org/10.2118/189439-PA

Watts, J.W., Fleming, G.C., Lu, Q., 2012. Determination of Active Constraints in a Network. SPE J. 17, 441–454.

Whitson, C.H., Rahmawati, S.D., Juell, A., 2012. Cyclic shut-in eliminates liquid-loading in gas wells, in: SPE/EAGE European Unconventional Resources Conference & Exhibition-From Potential to Production.

Wilson, G.M., 1969. A modified Redlich-Kwong equation of state, application to general physical data calculations, in: 65th National AIChE Meeting, Cleveland, OH. p. 15.

Woldesemayat, M.A., Ghajar, A.J., 2007. Comparison of void fraction correlations for

different flow patterns in horizontal and upward inclined pipes. Int. J. Multiph. Flow 33, 347–370.

Xu, Y., Cavalcante Filho, J.S.A., Yu, W., Sepehrnoori, K., 2017. Discrete-Fracture Modeling of Complex Hydraulic-Fracture Geometries in Reservoir Simulators. SPE Reserv. Eval. Eng. 20, 403–422.

Xu, Z., Song, X., Li, G., Wu, K., Pang, Z., Zhu, Z., 2018. Development of a transient non-isothermal two-phase flow model for gas kick simulation in HTHP deep well drilling. Appl. Therm. Eng. 141, 1055-1069.

Xue, X., Yang, C., Sharma, V.K., Datta-Gupta, A., King, M.J., 2016. Reservoir and Fracture Flow Characterization Using a Novel W (τ) Formulation, in: Unconventional Resources Technology Conference, San Antonio, Texas, 1-3 August 2016. pp. 831–852.

Yan, B., 2017. Development of general unstructured reservoir utility and fracture reservoir modeling. Ph.D. Disseration, Texas A&M University.

Yan, B., Mi, L., Chai, Z., Wang, Y., Killough, J.E., 2018. An Enhanced Discrete Fracture Network model for multiphase flow in fractured reservoirs. J. Pet. Sci. Eng. 161, 667–682. https://doi.org/10.1016/j.petrol.2017.12.016

Yan, B., Wang, Y., Nasrabadi, H., Killough, J.E., Wu, K., 2017. Accelerating Flash Calculation using Compositional Space for Compositional Simulation. J. Pet. Sci. Eng. 159, 1000–1008. https://doi.org/10.1016/j.petrol.2017.03.045

Yoshida, N., 2016. Modeling and Interpretation of Downhole Temperature in a Horizontal Well with Multiple Fractures. Texas A&M University.

Yu, W., Xu, Y., Weijermars, R., Wu, K., Sepehrnoori, K., 2017. Impact of Well Interference on Shale Oil Production Performance: A Numerical Model for Analyzing Pressure Response of Fracture Hits with Complex Geometries, in: SPE Hydraulic Fracturing Technology Conference. Society of Petroleum Engineers. https://doi.org/10.2118/184825-MS

Yuan, G., 2011. Liquid loading of gas wells. Master's thesis, University of Tulsa.

Zhang, F., Adel, I.A., Park, K.H., Saputra, I.W.R. and Schechter, D.S., 2018a. Enhanced Oil Recovery in Unconventional Liquid Reservoir Using a Combination of CO2 Huff-n-Puff and Surfactant-Assisted Spontaneous Imbibition, in: SPE Annual Technical Conference and Exhibition.

Zhang, S., Zhu, D., 2017. Inversion of Downhole Temperature Measurements in Multistage Fracture Stimulation in Horizontal Wells, in: SPE Annual Technical Conference and Exhibition.

Zhang, F., Saputra, I.W.R., Niu, G., Adel, I.A., Xu, L. and Schechter, D.S., 2018b. Upscaling Laboratory Result of Surfactant-Assisted Spontaneous Imbibition to the Field Scale through Scaling Group Analysis, Numerical Simulation, and Discrete Fracture Network Model, in: SPE Improved Oil Recovery Conference.

Zhang, Y., Seth, G., Chen, J., 2017. A Novel IPR Calculation Technique to Reduce Oscillations in Time-Lagged Network-Reservoir Coupled Modeling Using Analytical Scaling and Fast Marching Method, in: SPE Reservoir Simulation Conference.

Zhang, Y., Yu, W., Sepehrnoori, K., Di, Y., 2017. A Comprehensive Numerical Model

for Simulating Fluid Transport in Nanopores. Sci. Rep. 7.

Zuber, N., Findlay, Ja., 1965. Average volumetric concentration in two-phase flow systems. J. Heat Transfer 87, 453–468.

Zukoski, E.E., 1966. Influence of viscosity, surface tension, and inclination angle on motion of long bubbles in closed tubes. J. Fluid Mech. 25, 821–837.

APPENDIX A

This appendix lists the definitions of parameters in Eq. (2.8) of Section 2.1.2. The compressibility factor Z is solved by finding the cubic root of Peng-Robinson equation of state (Peng and Robinson, 1976).

$$Z_\alpha^{\,3} - (1 - B_\alpha) Z_\alpha^{\,2} + (A_\alpha - 3B_\alpha^{\,2} - 2B_\alpha) Z_\alpha - (A_\alpha B_\alpha - B_\alpha^{\,2} - B_\alpha^{\,3}) = 0, \quad \text{(A.1)}$$

where

$$A_\alpha = \frac{P_\alpha a}{(RT)^2}, \quad \text{(A.2)}$$

$$B_\alpha = \frac{P_\alpha b}{RT}, \quad \text{(A.3)}$$

$$a = \sum_{c=1}^{n_c} \sum_{j=1}^{n_c} x_c x_j (1 - \kappa_{cj}) \sqrt{a_c a_j}, \quad \text{(A.4)}$$

$$b = \sum_{j=1}^{n_c} x_j b_j, \quad \text{(A.5)}$$

$$a_j = 0.4572 \frac{(RT_{cj})^2}{P_{cj}} \left[1 + m_j (1 - \sqrt{T / T_{cj}}) \right]^2, \quad \text{(A.6)}$$

$$b_j = 0.0778 \frac{RT_{cj}}{P_{cj}}, \quad \text{(A.7)}$$

$$\begin{aligned} m_j &= 0.3746 + 1.5423 w_j - 0.2699 w_j^2 \quad (w_j < 0.49), \\ m_j &= 0.3796 + 1.4850 w_j - 0.1644 w_j^2 + 0.0167 w_j^3 \quad (w_j \geq 0.49). \end{aligned} \quad \text{(A.8)}$$

κ_{cj} is the binary interaction coefficient between component c and j. w_j is the acentric factor of component j. T_{cj} and P_{cj} are critical temperature and critical pressure of component j.

APPENDIX B

The sources and property ranges of the TUFFP dataset mentioned in Section 5.2 are summarized as follows:

Investigator (s)	**Inclination range θ (degree)**	**Pipe Diameter D (cm)**	**Gas superficial velocity V_g (m/s)**	**Liquid superficial velocity V_l (m/s)**	**Liquid viscosity μ_l (cP)**
Abdul-Majeed (2000)	0	5.08	[0.196 : 48.908]	[0.002 : 1.825]	[1.3 : 1.9]
Akpan (1980)	0	7.62	[0.199 : 5.458]	[0.137 : 1.701]	[0.1 : 0.14]
Alsaadi (2013)	[2 : 30]	7.62	[1.829 : 39.992]	[0.010 : 0.101]	[0.9 : 1.3]
Beggs (1973)	[-10 : 10]	2.54	[0.299 : 25.323]	[0.023 : 5.203]	[0.7 : 1.6]
Brill et al. (1996)	0	7.79	[3.629 : 12.656]	[0.004 : 0.046]	[1.6 : 1.8]
Caetano (1986)	90	6.34	[0.023 : 22.859]	[0.002 : 3.579]	[0.5 : 2.7]
Cheremisinoff (1977)	0	6.35	[2.582 : 25.241]	[0.017 : 0.070]	[0.9 : 1.2]
Eaton (1965)	0	10.20	[0.112 : 21.901]	[0.011 : 2.108]	[0.7 : 1.3]
Fan (2005)	[-2 : 2]	5.08	[4.93 : 25.70]	[0.0003 : 0.052]	1.0
Felizola (1992)	[0 : 90]	5.10	[0.39 : 3.36]	[0.050 : 1.490]	[1.3 : 4.7]
Guner (2012)	[0 : 45]	7.62	[1.485 : 39.388]	[0.010 : 0.100]	1.0
Johnson (2005)	[0 : 5]	10.00	[0.711 : 4.523]	[0.019 : 0.605]	1.0
Kouba (1986)	0	7.62	[0.302 : 7.361]	[0.152 : 2.137]	[1.2 : 1.8]
Magrini (2009)	[0 : 90]	7.62	[36.63 : 82.32]	[0.003 : 0.040]	1.0
Meng (1999)	[-2 : 2]	5.08	[4.6 : 26.6]	[0.001 : 0.054]	[4.7 : 6.3]
Minami (1983)	0	7.79	[0.475 : 16.590]	[0.005 : 0.951]	[0.6 : 2]
Mukherjee (1980)	[-90 : 90]	3.81	[0.037 : 41.310]	[0.015 : 4.362]	[0.6 : 74.4]
Rothe et al. (1986)	[-2,0]	17.10	[0.610 : 4.633]	[0.061 : 1.830]	0.88
Roumazeilles (1994)	[-30 : 0]	5.10	[0.914 : 9.357]	[0.884 : 2.438]	[1.4 : 2.2]
Schmidt (1976)	90	5.08	[0.042 : 13.146]	[0.012 : 3.480]	[1 : 2.4]
Vongvuthipornchai (1982)	0	7.62	[0.061 : 2.938]	[0.070 : 2.146]	[1.1 : 1.5]
Yuan (2011)	[30 : 90]	7.62	[9.90 : 36.00]	[0.005 : 0.100]	1.0